2-2014

Biophysical Studies of Axonal Transport

Leslie Cyle Conway
University of Massachusetts - Amherst, leslie.cyle@gmail.com

Recommended Citation

Conway, Leslie Cyle, "Biophysical Studies of Axonal Transport" (2014). *Doctoral Dissertations 2014-current.* Paper 35.

Biophysical Studies of Axonal Transport

A Dissertation Presented

by

LESLIE C. CONWAY

Submitted to the Graduate School of the
University of Massachusetts Amherst in partial fulfillment
of the requirements for the degree of

DOCTOR OF PHILOSOPHY

FEBRUARY 2014

Molecular and Cellular Biology

Biophysical Studies of Axonal Transport

A Dissertation Presented

by

LESLIE C. CONWAY

Approved as to style and content by:

Jennifer L. Ross, Chair

Maria Kilfoil, Member

Wei-Lih Lee, Member

Thomas Maresca, Member

Barbara A. Osborne, Director
Molecular and Cellular Biology Program

DEDICATION

To my family.

ACKNOWLEDGMENTS

I would like to thank Professor Jennifer Ross for her guidance and mentorship throughout my graduate career. Her enthusiasm for research and teaching has been an inspiration throughout my time here. I am extremely lucky to have had the opportunity to carry out my dissertation research in her lab.

I would like to thank my family for all of their support and interest in my research throughout the progression of my PhD.

I would like to thank Fabian Romano for all of the support, encouragement, and advice he has given me during my time here.

I would like to thank Professor Maria Kilfoil for providing the particle tracking software which was used for the high resolution tracking of the self-assembled quantum dot cargos. I would like to thank Derek Wood, as he created modifications to this code that allowed me to use this software to analyze my data. In addition, he created a GUI that allowed me to easily run the software. I would also like to thank Erkan Tüzel for the many conversations he had with us regarding motor transport on crowded microtubules. Throughout the course of these experiments, he and his lab members were working on simulations to model my experimental system. This collaboration resulted in many conversations that provided new insights into the results obtained from my experiments.

I would like to thank Joshua Pringle and Amanda Tan for the purification of MAP65, which was used in the studies of kinesin motility on microtubule bundles.

I would like to thank Professor Patricia Wadsworth and Sai Balchand for helping me get started with the CAD cell culture, and for use of their lab tissue culture facilities.

Finally, I would like to thank my committee members: Professors Maria Kilfoil, Wei-Lih Lee, and Thomas Maresca for their input and advice throughout the progression of my research.

ABSTRACT

BIOPHYSICAL STUDIES OF AXONAL TRANSPORT

FEBRUARY 2014

LESLIE C. CONWAY

B.S., UNIVERSITY OF MASSACHUSETTS LOWELL

Ph.D., UNIVERSITY OF MASSACHUSETTS AMHERST

Directed by: Professor Jennifer L. Ross

Intracellular transport provides a mechanism by which cellular material, such as organelles, vesicles, and protein, can be actively transported throughout the cell. This process relies on the activity of the cytoskeletal filament, microtubules, and their associated motor proteins. These motors are able to walk along microtubule tracks while carrying cellular cargos to enable the fast, regulated transport of these cargos. In cells, these microtubule filaments act as a binding platform for numerous different motor species as well as microtubule-associated proteins (MAPs). In addition, these filaments often form higher order structures, such as microtubule bundles. How motors navigate such complex, crowded tracks to ensure the efficient transport of cargos is unclear. While motor transport can be studied in vivo, such studies are complicated to interpret as there are many unknowns, such as which motor species are driving transport, which MAPs are bound to specific regions of microtubule tracks, and what types of microtubule architectures are present.

In the studies presented here, motor transport was reconstituted in vitro, allowing for the precise control over motor types, motor densities, the relative number of motors per cargo, and the types of microtubule tracks present. To this simplified system, specific complexities were added to microtubule tracks to systematically study the effect of certain track complexities on motor transport. Specifically, the effect of motor traffic and different microtubule bundle architectures on the transport properties of kinesin-1 motors was studied. In addition, the effect of motor domain mutations on the transport properties of kinesin-1 motors was also probed. These studies provide new insights into how motor transport is altered on microtubule tracks reminiscent of those present in the cell, as well as mechanisms utilized by kinesin motors to efficiently navigate these complex tracks.

TABLE OF CONTENTS

Page

ACKNOWLEDGMENTS v
ABSTRACT vi
LIST OF FIGURES xi

CHAPTER

1. INTRODUCTION 1

    1.1 Biophysics 1
    1.2 Microtubules 2
    1.3 Microtubule Motor Proteins 7
    1.4 Intracellular Transport 16
    1.5 Neurodegenerative Disease 25
    1.6 Motivation 26

2. MOTOR TRANSPORT OF SELF-ASSEMBLED CARGOS IN CROWDED ENVIRONMENTS 28

    2.1 Introduction 28
    2.2 Results 29

        2.2.1 Experimental Set-Up 29
        2.2.2 Non-Biotinylated Motors Transiently Interact with Qdot Cargos 35
        2.2.3 Motor Density on Crowded Microtubules 43
        2.2.4 Motility of Single Motors versus Cargos on Crowded Microtubules 48
        2.2.5 Qdot Cargos Exhibit Pausing on Crowded Microtubules 53
        2.2.6 Qdot Cargos Reverse on Crowded Microtubules 59

    2.3 Discussion 61
    2.4 Methods 70

        2.4.1 Protein Purification 70
        2.4.2 Qdot-motor attachment. 70
        2.4.3 Microtubule Preparation. 71
        2.4.4 In Vitro Assays. 71
        2.4.5 Two-Color Assays. 72
        2.4.6 Imaging. 73
        2.4.7 Data Analysis. 73
        2.4.8 Estimate of the Kinesin binding constant from images. 74
        2.4.9 Estimate of the Qdot binding constant to kinesin using bulk assay. 75
        2.4.10 Estimate of the Qdot binding constant to kinesin using visual assay. 76

3. KINESIN MOTILITY ON MICROTUBULE BUNDLES 78

- 3.1 Introduction 78
- 3.2 Results 81
  - 3.2.1 Kinesin Motility on Single Microtubules in the Presence of PEG 81
  - 3.2.2 Kinesin Motility on PEG Bundles 87
  - 3.2.3 Kinesin Motility on Single Microtubules in the Presence of MAP65 92
  - 3.2.4 Kinesin Motility on MAP65 Bundles 96
  - 3.2.5 Kinesin Motility on Cellular Bundles 101
- 3.3 Discussion 106
- 3.4 Methods 117
  - 3.4.1 Protein Purification. 117
  - 3.4.2 Microtubule Polymerization. 118
  - 3.4.3 Motility on Single Microtubules. 118
  - 3.4.4 Motility on PEG Microtubule Bundles. 119
  - 3.4.5 Motility on MAP65 Microtubule Bundles. 119
  - 3.4.6 CAD Cell Culture. 120
  - 3.4.7 Motility on CAD Cell Microtubule Bundles. 120
  - 3.4.8 Imaging. 120
  - 3.4.9 Data Analysis. 121

4. STUDY OF KINESIN MOTOR DOMAIN MUTANTS 122

- 4.1 Introduction 122
- 4.2. Results 126
  - 4.2.1 Single Molecule Studies of Kinesin E157 Mutants 126
  - 4.2.2 Multiple-Motor Studies of Kinesin E157 Mutants 130
- 4.3 Discussion 132
- 4.4 Methods 136
  - 4.4.1 Constructs. 136
  - 4.4.2 Protein Purification. 136
  - 4.4.3 Microtubule Preparation. 136
  - 4.4.4 Single Molecule Assays. 137
  - 4.4.5 Gliding Assays. 137
  - 4.4.6 Imaging. 137
  - 4.4.7 Data Analysis. 138

5. CONCLUSIONS AND FUTURE DIRECTIONS 139

5.1 Summary 139

5.1.1 Transport of Self-Assembled Qdot Cargos 139
5.1.2 Motor Transport on Bundled Microtubules 141
5.1.3 Kinesin Motor Domain Mutants 142

5.2 Future Directions 144

APPENDICES

A. DISTRIBUTIONS OF SINGLE MOLECULE DATA 148
B. PROTOCOLS 160

BIBLIOGRAPHY 177

LIST OF FIGURES

Figure Page

1.1. Microtubule Structure. 3

1.2. Kinesin-1 Structure and Microtubule Binding. 11

1.3. Kinesin-1 ATPase Cycle. 14

1.4. Cargo Binding Mechanism of Kinesin-1. 20

2.1. Run Length Comparison to Distinguish Single Motor versus Multi-Motor Qdot Cargos 32

2.2 Qdots are Transported by Non-Biotinylated Kinesin Motors 34

2.3 Two-Color Single Molecule Assays Show Association and Dissociation of Kinesin Motors to Qdot Cargos 36

2.4 Binding Constant Estimate for Qdots Binding to Non-Biotinylated Kinesin 38

2.5 Number of Kinesin Motors Bound to Qdot Cargos 41

2.6 Motor Density on Crowded Microtubules 44

2.7 Binding Constant Estimate for Kinesin Binding to Microtubules 46

2.8 Representative Kymographs Showing Motility of Cargos versus Single Motors on Microtubules with Different Levels of Crowding 49

2.9 Motility Properties of Single Motors and Cargos on Crowded Microtubules 52

2.10 Pausing of Cargos on Crowded Microtubules 54

2.11 Cumulative Probability Distributions for Qdot Cargo Pause Durations 58

2.12 Cargo Reversals on Crowded Microtubules 60

2.13 Non-Specific Interactions of Kinesin Motors with Quantum Dots 62

3.1 Microtubule Bundle Types 80

3.2 Effect of PEG on Kinesin Binding to Microtubules 83

3.3 Kinesin Motility on Single Microtubules in the Presence of PEG 85

3.4 Kinesin Motility on PEG Bundles 89

3.5 Kinesin Motility on Single Microtubules in the Presence of MAP65 94

3.6 Kinesin Motility on MAP65 Bundles 98

3.7 CAD Cells as a Model to Study Parallel Microtubule Bundles.......................... 102

3.8 Kinesin Motility on Cellular Bundles 104

3.9 Kinesin Motility on PEG versus MAP65 Microtubule Bundles.......................... 111

4.1 Kinesin E157 Residue is Located on the Motor Domain 125

4.2 Single Molecule Studies of Mutant Kinesin Motors 128

4.3 Multiple-Motor Gliding Assays with Wildtype and Mutant Kinesin Motors 131

A.1 Kinesin Motility on Single Microtubules in the Presence of PEG: Histograms 148

A.2 Kinesin Motility on Single Microtubules in the Presence of PEG: Cumulative Probability Distributions 149

A.3 Kinesin Motility on PEG Bundles: Histograms 150

A.4 Kinesin Motility on PEG Bundles: Cumulative Probability Distributions........ 151

A.5 Kinesin Motility on Single Microtubules in the Presence of MAP65: Histograms 152

A.6 Kinesin Motility on Single Microtubules in the Presence of MAP65: Cumulative Probability Distributions 153

A.7 Kinesin Motility on MAP65 Bundles: Histograms... 154

A.8 Kinesin Motility on MAP65 Bundles: Cumulative Probability Distributions 155

A.9 Kinesin Motility on Cellular Bundles: Histograms 156

A.10 Kinesin Motility on Cellular Bundles: Cumulative Probability Distributions 157

A.11 Single Molecule Studies of Mutant Kinesin Motors: Histograms 158

A.12 Single Molecule Studies of Mutant Kinesin Motors: Cumulative Probability Distributions... 159

CHAPTER 1

INTRODUCTION

1.1 Biophysics

Biophysics is an interdisciplinary field that involves the application of physics to the study of biological questions. The field of biophysics entails a quantitative approach to provide new insights into the forces and energy-driven processes behind biological processes. Popular areas of biophysics research include protein folding, membrane biology, and motor proteins, to name a few. Motor proteins within the cell use energy derived from ATP hydrolysis to perform work. Current research interests are focused on how these motors function to transport cellular cargos and generate forces to rearrange and depolymerize cytoskeletal filaments.

In this dissertation, I aim to study the mechanisms by which microtubule motor proteins function to transport cargos throughout the cell. These motors walk along microtubule filaments to distribute organelles, proteins, mRNA, and other cellular cargos. In the cell, these microtubule tracks are extremely complex, as they can form higher order architectures and can be crowded with microtubule-associated proteins (MAPs) and motor proteins. I aim to understand how motor proteins navigate complex microtubule tracks reminiscent of what would be encountered in the cell. This question will be addressed using purified components to reconstitute motor transport in vitro. With this system, I will systematically build up the complexity of microtubule tracks by adding purified MAPs or motor traffic, or by introducing complex microtubule architectures, such as microtubule bundles. From these studies, I hope to develop a better understanding of the mechanisms used by microtubule motor proteins to efficiently navigate the complex tracks present in the cell.

1.2 Microtubules

Microtubules are cytoskeletal filaments that spread throughout cells to provide structure to the cell, generate and maintain cell morphology, aid in the separation of genetic material during cell division, and function as tracks for microtubule motor proteins transporting cellular cargos. Microtubules are hollow tubes that are 25 nm in diameter and can grow up to lengths of many microns. These filaments are comprised of αβ-tubulin heterodimers that polymerize to form microtubules in the presence of guanosine triphosphate (GTP) (Arai and Kaziro, 1977). During polymerization, an α-subunit of a tubulin dimer will only bind to a β-subunit of a dimer already in the microtubule, or vise versa. This creates a polarized structure where α-tubulin is exposed on one end of the filament, while β-tubulin is exposed on the opposite end (Figure 1.1A). These are referred to as the microtubule minus and plus ends, respectively (Fan et al., 1996; Hirose et al., 1995).

There are two types of interactions between αβ-tubulin heterodimers within a microtubule structure: longitudinal and lateral interactions. Longitudinal interactions describe the head-to-tail interactions of αβ-tubulin heterodimers which result in the formation of protofilaments (Figure 1.1A). These interactions are largely dominated by hydrophobic and polar interactions (Nogales et al., 1999).

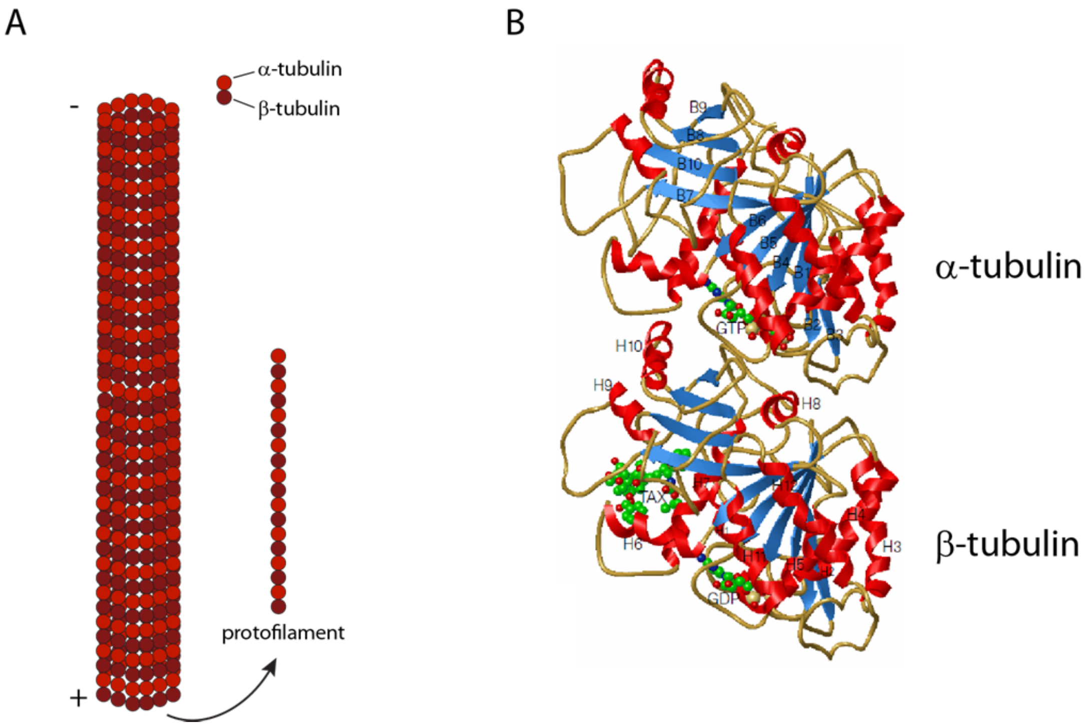

Figure 1.1. Microtubule Structure.

A. Polymerized microtubule structure comprised of αβ-tubulin heterodimers. Minus and plus signs denote the polarity of the filament. A single protofilament is shown to the right of the microtubule structure. **B.** Structure of the tubulin heterodimer with helices (H) and β-sheets (B) labeled for reference. GTP is bound to the N-site of α-tubulin and GDP is bound to the E-site of β-tubulin. Taxol (TAX) is shown bound to the β-tubulin subunit. Tubulin heterodimer structure was adapted from Nogales et al, 1998. Reproduced with permission from Nature Publishing Group, Copyright (1998).

Lateral interactions occur between adjacent protofilaments at an angle, giving the microtubule the curvature required to form a hollow tube (Nogales et al., 1999). These interactions are largely maintained through electrostatic interactions (Nogales et al., 1999). Lateral interactions are typically homologous, in that they involve interactions between two adjacent α-tubulin monomers or two adjacent β-tubulin monomers (referred to as a B lattice) (Song and Mandelkow, 1993). In some cases, an A lattice exists, where an α-tubulin monomer interacts with a β-tubulin monomer. This typically occurs at the seam of a microtubule (Song and Mandelkow, 1993). The seam results from the culmination of slight shifts in the lateral contacts between each protofilament. While B-lattice interactions still occur between each neighboring protofilament, there is one point in the microtubule where the lattices no longer match up, which is referred to as the seam. Here, an α-tubulin monomer contacts a β-tubulin monomer, forming an A-lattice.

Polymerization of microtubules is stimulated by the presence of GTP. Both α-and β-tubulin have a GTP binding site on the N-terminal region of the protein (Figure 1.1B) (Nogales et al., 1998). Because the GTP-binding site of α-tubulin is located at the dimer interface, the GTP is buried and cannot be hydrolyzed (Nogales et al., 1998). Thus, this site is referred to as the non-exchangeable, or N site. The GTP-binding site of β-tubulin is accessible until a new dimer binds. Upon binding of a new dimer, loop T7 and helix H8 of the new α-subunit interacts with the exchangeable site (E site) GTP of the incorporated tubulin dimer (Nogales et al., 1998). This E site GTP is then hydrolyzed to GDP.

Overall, α- and β-tubulin monomers are very similar in structure (Figure 1.1B). Both are compact structures formed by a core of two β-sheets surrounded by twelve α-helices (Nogales et al., 1998). Each monomer is 4 nm in height, and therefore each αβ-tubulin heterodimer is 8 nm in height (Nogales et al., 1998). On the outside surface of the microtubule, helices H11 and H12 of both α- and β-subunits are exposed (Nogales et al., 1998). These two helices are important for mediating specific interactions with microtubule associated proteins (MAPs) as well as microtubule motor proteins (Nogales et al., 1998). In addition, both α- and β-subunits have a disordered C-terminal tail (Nogales et al., 1998). This tail is 10 or 18 amino acids in length for an α- or β-subunit, respectively (Nogales et al., 1998). These tails are highly acidic (negatively charged at neutral pH) and promote the association of MAPs and motors through electrostatic interactions (Nogales et al., 1998; Sackett, 1995).

While microtubules are comprised entirely of αβ-tubulin dimers, these filaments can be modified post translationally to create distinct populations of microtubules throughout the cell. These post-translational modifications are reversible modifications that include acetylation, detyrosination, polyglutamylation, and polyglycylation of tubulin subunits that are incorporated into microtubule polymers (Janke and Bulinski, 2011). These modifications typically signify stable populations of microtubules and allow the cell to specifically regulate motor activity, MAP binding, and depolymerase or severing activity on specific subsets of microtubules within the cell (Janke and Bulinski, 2011). This allows for the fine tuning of microtubule dynamics and transport in specific regions of the cell.

Acetylation involves the addition of an acetyl group to the α-subunit of tubulin (L'Hernault and Rosenbaum, 1985). This modification occurs on Lys40, a residue that is located inside the microtubule lumen (L'Hernault and Rosenbaum, 1985). Acetylation is commonly associated with stable microtubules, as these microtubules have been shown to be more resistant to drug-induced microtubule depolymerization (Matsuyama et al., 2002).

Like acetylation, detyrosination occurs specifically on α-tubulin (Arce et al., 1975). Detyrosination results in the removal of the last residue of the C-terminal tail of α-tubulin, which is a tyrosine residue (Hallak et al., 1977). This modification has been shown to increase the binding affinity of kinesin-1 to microtubules 2.8-fold (Dunn et al., 2008; Konishi and Setou, 2009; Liao and Gundersen, 1998), while decreasing the binding of CAP-Gly proteins, proteins that bind to growing microtubule plus ends (Bieling et al., 2008; Peris et al., 2006; Weisbrich et al., 2007). In addition, detyrosinated microtubules have been shown to exhibit increased stability in the presence of kinesin-13 depolymerizing kinesins (Peris et al., 2009).

Polyglutamylation and polyglycylation result in the addition of chains of glutamic acid or glycine to C-terminal tails of either α- or β-tubulin (Alexander et al., 1991; Edde et al., 1990; Redeker et al., 1994; Rudiger et al., 1992). These chains branch off of a glutamic acid residue within the C-terminal tail and can vary in length (Alexander et al., 1991; Edde et al., 1990; Redeker et al., 1994; Rudiger et al., 1992). In cells, long chains of glutamic acid have been shown to increase the susceptibility of microtubules to microtubule severing proteins such as katanin and spastin, while short chains of glutamic acid have no effect (Sharma et al., 2007). Additionally, it has been observed that a decrease in polyglutamylation results in the disruption of binding of both kinesin-3 (KIF1A) in neurons (Ikegami et al., 2007), as well as dynein (Kubo et al., 2010; Suryavanshi et al., 2010).

In addition to diverse microtubule populations generated through post translational modifications of tubulin, microtubule architecture can take on distinct forms in different regions of the cell or different phases of the cell cycle. In interphase, microtubules radiate outwards from the microtubule organizing center, with all microtubule plus ends pointing to the cell periphery. In cells undergoing mitosis, microtubules are bundled in an antiparallel array at the spindle midzone (Loiodice et al., 2005). This antiparallel array enables the generation of forces by motors at the spindle midzone to ensure the proper segregation of genetic material during mitosis. Astral microtubules emanate from each centrosome during mitosis, pointing away from the spindle midzone, towards the cell cortex. Astral microtubules are oriented such that their plus ends point towards the cortex. This population of microtubules is important for the generation of forces which function to position the mitotic spindle (Palmer et al., 1992). In neurons, microtubule architecture varies depending on the region of the cell. In the cell body, microtubules form an array similar to that found in interphase cells. In the axons, microtubules are bundled by MAPs, forming parallel arrays of microtubules that are uniformly polarized with all microtubule plus ends pointing away from the cell body (Heidemann et al., 1981). In dendrites, microtubules are also bundled by MAPs, but the microtubules within these bundles are randomly oriented, with about 50% of microtubule plus ends pointing toward the cell body, and 50% of microtubule plus ends pointing away from the cell body (Baas et al., 1988). These specific arrangements of microtubules enable the polarized transport of cellular cargos by microtubule motor proteins.

While the basic structure of all microtubules is the same, these filaments can be tuned by specific post translational modifications and by the architecture that they assemble. This enables microtubules to specifically direct the traffic of molecular cargos throughout the cell, as well as the generation of forces within the cell.

1.3 Microtubule Motor Proteins

An important function of microtubules is to provide tracks for motor proteins. Motor proteins walk along these tracks while carrying cellular cargos, enabling the distribution of cargos throughout the cell. These cargos can include mRNA, proteins, vesicles, or organelles. While small molecules are able to diffuse throughout the cell rather efficiently, large cargos rely on the active transport of motor proteins for movement throughout the cell at a rate faster than diffusion. In addition, motor transport can specifically direct the spatial distribution of cargos due to signals created by microtubule tracks, such as post translational modifications and microtubule architecture. This process of motor-driven transport of cargos throughout the cell is referred to as intracellular transport, or is also referred to as cargo transport. Two microtubule motor proteins important for intracellular transport include kinesin-1 and cytoplasmic dynein.

Cytoplasmic dynein is a member of the AAA+ (ATPase associated with various cellular activities) family of proteins (Neuwald et al., 1999). It is comprised of two dimerized heavy chains and several associated light chains (Vale, 2003). Each heavy chain has six concatenated AAA domains that form a ring. While the first four of these AAA domains have ATP binding and hydrolysis sites, only the first domain has been found to be essential for dynein motility (Reck-Peterson and Vale, 2004). A 15 nm coiled-coil stalk stretches from the hexamer of AAA domains to a microtubule binding domain (Asai and Koonce, 2001). Using energy derived from ATP hydrolysis, dynein is able to take processive steps along the microtubule. The steps of this motor are rather unrestricted and variable. The step size of dynein ranges from 4 to 32 nm (Reck-Peterson et al., 2006). In addition, dynein stepping is not restricted to a single protofilament or direction. This motor has been shown to be able to side-step onto adjacent protofilaments (Reck-Peterson et al., 2006). In addition, while dynein is predominantly a minus-end directed motor, it has been shown to reverse direction during a processive run (Ross et al., 2006).

Dynactin associates with dynein and has been shown to be essential for dynein function. This protein is also involved in the attachment of cargos to the motor (Holleran et al., 2001). In addition, dynactin has a microtubule binding domain which is thought to enhance dynein processivity by acting as a microtubule tether (King and Schroer, 2000).

Kinesin-1 is another important motor involved in intracellular transport, and will be the focus of this dissertation. This motor was first identified in 1985 during a purification process aimed to isolate the ATPase responsible for promoting the translocation of organelles along microtubules in giant squid axons (Vale et al., 1985a). A non-hydrolyzable version of ATP, AMP-PNP, had previously been shown to inhibit motility of cargos in giant squid axons, locking cargos onto microtubule filaments (Lasek, 1984). This observation was used to help isolate kinesin motors. AMP-PNP was added to squid axoplasm supernatant in the presence of microtubules with the idea that kinesin motors would lock onto microtubules. Centrifugation was used to pellet the microtubules and separate any proteins that were not bound to microtubules. ATP and salt were added to promote the release of kinesin motors from microtubules. A second centrifugation resulted in the separation of released motors from microtubules and any remaining microtubule-bound proteins. The released motor was approximately 110 kDa in size, and was shown to promote the motility of microtubules in a microtubule gliding assay. This isolated motor was named ‘kinesin’, derived from the Greek word kinesis, which refers to movement (Vale et al., 1985a).

Kinesin-1 exists as a heterotetramer, consisting of two heavy chains and two associated light chains (Figure 1.2A). The two heavy chains dimerize through a coiled-coil stalk, and the light chains associate with the C-terminal region of this stalk. The kinesin heavy chains are essential for microtubule binding and movement, while the kinesin light chains mediate interactions with cellular cargos.

Each heavy chain consists of 960 amino acids that code for a globular N-terminal motor domain, a neck linker, an extended coiled-coil stalk, and a globular C-terminal tail domain (Yang et al., 1989). The motor domain consists of a microtubule binding domain as well as a nucleotide binding site, where ATP binds (Yang et al., 1989). The kinesin motor domain interacts with both tubulin subunits, however the majority of the interactions are mediated through the β-subunit of tubulin (Gigant et al., 2013; Song and Mandelkow, 1993). A recent structure of the kinesin-1 motor head bound to a tubulin dimer shows that helix H12 and the H8-S7 loop of β-tubulin are important for interactions with loops L8 and L12, and the β-strand before loop L8 in the kinesin motor head (Figure 1.2B) (Gigant et al., 2013). In addition, parts of helices H3, H11, and H12 and the H11-H12 loop of α-tubulin were shown to be important to mediate interactions with loop L11 and helices H4 and H6 of the kinesin motor head (Gigant et al., 2013). Interactions between kinesin and tubulin have been shown to be largely electrostatic and hydrophobic in nature (Woehlke et al., 1997).

The motor domain is followed by a 14 amino acid flexible neck linker that joins the motor head to the coiled-coil stalk. The coiled-coil stalk is made up of α-helices and facilitates the dimerization of two kinesin heavy chains (Yang et al., 1989). This dimerization is essential for kinesin processivity (Hancock and Howard, 1998). In addition, a hinge region within the coiled-coil stalk allows the C-terminal tail of kinesin to fold over and interact with the motor domain. This conformation is stabilized by the presence of kinesin light chains and results in the autoinhibition of kinesin motors, as motors in this folded state are unable to release ADP from their nucleotide pocket and are unable to bind microtubules (Dietrich et al., 2008; Hackney and Stock, 2008; Verhey et al., 1998).

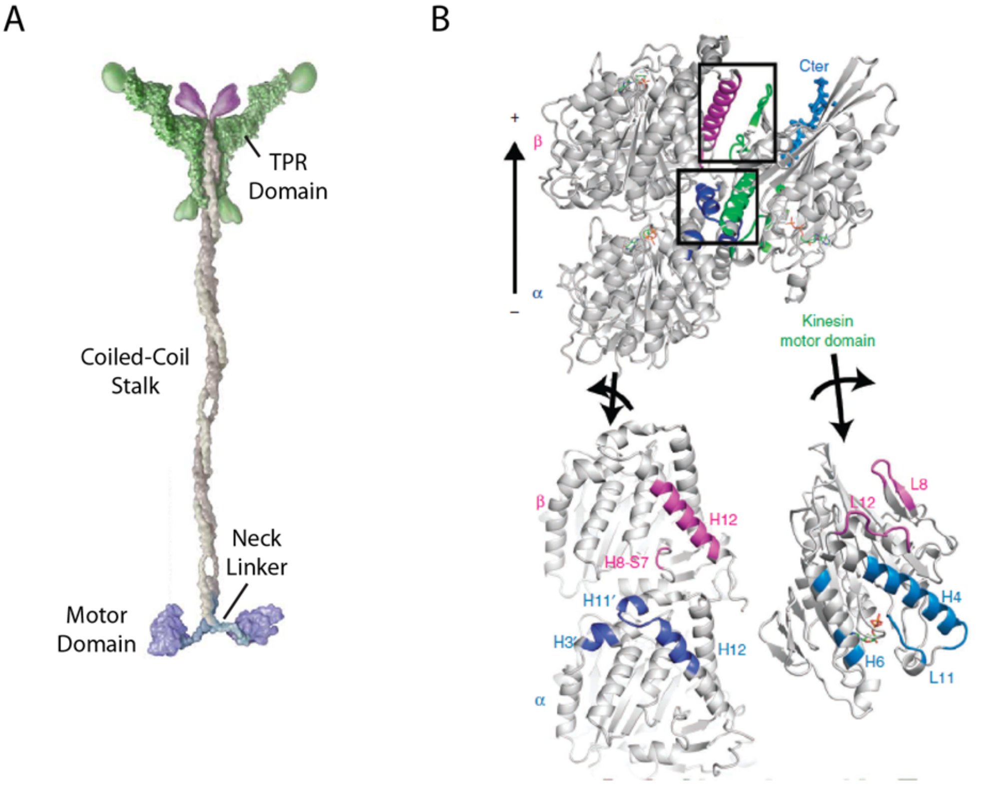

Figure 1.2. Kinesin-1 Structure and Microtubule Binding.

A. Kinesin-1 shown as a compilation of known structures. Unknown parts of the structure are depicted as smooth domains. Figure adapted from Vale, 2003. Reproduced with permission from Elsevier. **B.** Structure of kinesin-1 bound to an αβ-tubulin heterodimer. Regions involved in the kinesin-microtubule binding interaction are highlighted and further depicted in rotated model below. Figure adapted from Gigant et al., 2013. Reprinted with permission from Macmillan Publishers Ltd: Nature Structural & Molecular Biology (Gigant et al., 2013), 2013.

This autoinhibition mechanism is thought to be relieved upon binding to cargos (Coy et al., 1999). For the study of kinesin motors, truncated kinesin constructs are often used that prevent motor autoinhibition. These constructs have enough of the coiled-coil domain to facilitate dimerization, but lack the hinge region and tail region responsible for autoinhibition. In the studies presented in this dissertation, I use a truncated human kinesin construct, K560, which possesses only the first 560 amino acids of the human kinesin heavy chain (Woehlke et al., 1997). This construct allows for the study of constitutively active kinesin motors.

When dimerized, kinesin walks processively towards the plus ends of microtubule filaments (Vale et al., 1985b). This motor steps along microtubules in a hand-over-hand manner (Yildiz et al., 2004), with one head bound to the microtubule at all times to prevent dissociation. The ATPase cycle of kinesin is tightly regulated to ensure that one motor head is bound to the microtubule at all times, allowing for processive motility (Figure 1.3) (Gilbert et al., 1998). Free in solution, kinesin motor heads are bound to ADP. Upon binding to the microtubule, head 1 releases its ADP and binds the microtubule tightly in an apo state. When ATP binds to head 1, conformational changes in the kinesin motor domain cause docking of the neck linker onto the motor domain (Rice et al., 1999). The neck linker interacts with the motor domain in such a way that it points towards the plus end of the microtubule. This neck linker docking biases the positioning of head 2 ahead of head 1, towards the microtubule plus end (Rice et al., 1999). When head 2 reaches its forward binding site, in front of head 1, it binds weakly to the microtubule. Following ATP hydrolysis on head 1, head 2 releases its ADP and binds tightly to the microtubule. Head 2 is now tightly bound to the microtubule in an apo state. After release of inorganic phosphate from the hydrolyzed ATP on head 1, this head is bound to ADP and unbinds from the microtubule. At this point, the cycle begins again, with head 1 binding in front of head 2, resulting in the processive plus-end directed, hand-over-hand motility of kinesin. Kinesin-1 is able to take 100-200 consecutive steps, moving approximately 1-2 μm, before dissociating from the microtubule.

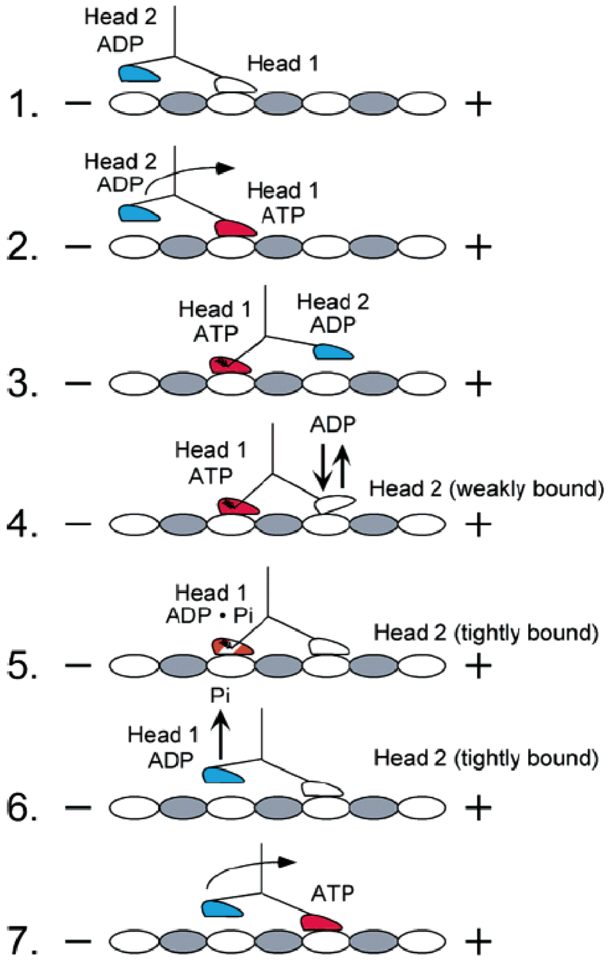

Figure 1.3. Kinesin-1 ATPase Cycle.

Schematic depicting the ATPase cycle of kinesin-1 dimeric motors. Motor heads are bound to the microtubule when in the apo state (white) or when bound to ATP (red). In the ADP-bound state (blue), motor heads are unbound from the microtubule. This figure was reprinted from Klumpp et al, 2003. Copyright (2003) American Chemical Society.

Kinesin-1 has been shown to take steps that are 8 nm in size (Svoboda et al., 1993), while following a single protofilament along a microtubule (Ray et al., 1993). This strict motility pattern is due to the short neck linker length and the specific binding region of kinesin on the microtubule. Each neck linker can stretch up to only 4 nm in length (Hariharan and Hancock, 2009). Thus, a walking motor can stretch its next head up to 8 nm forward, due to the contributions of both neck linkers. This 8 nm distance is the same size as a tubulin dimer (Nogales et al., 1998). Therefore, with each step, a kinesin motor head can reach forward to its next binding site on the next adjacent tubulin dimer, with the center of mass of the motor moving 8 nm with each step. The size of the kinesin neck linker has been shown to be extremely important for the processive motility of these motors. Studies where the kinesin neck linker length has been made either longer or shorter have shown that even minor changes in neck linker length disrupt kinesin processivity (Shastry and Hancock, 2010). When the neck linker was shortened by just one amino acid, motors lost all processivity. This suggests that the wildtype neck linker is just long enough for kinesin to reach its next binding site. By removing one amino acid, this mutant could no longer reach its next binding site, thereby making it non-processive. When the neck linker was extended by 1-3 amino acids, kinesin processivity was reduced proportionally. These results suggest that the short neck linker length is important for the generation of strain between the two motor heads, which thereby enables the tight coupling of the two motor heads (Shastry and Hancock, 2010).

In addition to kinesin-1 and cytoplasmic dynein, there are a number of other motor proteins that exist in the cell. All of these motors possess different motility properties, cargo binding preferences, and distributions throughout the cell. This diversity allows for the transport of cargos to be finely tuned in a cell where there are many different cargos that need to be transported to specific regions.

1.4 Intracellular Transport

Microtubule motors bind and transport a variety of cargos in the cell. These cargos include proteins that are just nanometers in size, vesicles that can be 50 nm – 1 μm in size, and organelles such as mitochondria, which can be as large as 10 μm in diameter. The transport of these cargos within a cell is imperative for the survival of all cell types. Newly synthesized proteins must be distributed from their site of synthesis to where they are needed for their specific cellular function. For instance, newly synthesized proteins that must be secreted from the cell are packaged in secretory vesicles that must be transported to the cell periphery (Marks et al., 1994). Alternatively, extracellular material that needs to be degraded is endocytosed and must be transported from the cell membrane to lysosomal compartments within the cell (Settembre et al., 2013). All of these diverse forms of traffic are mediated by motor proteins.

While intracellular transport is imperative for the survival of all cell types, it is especially important in neurons. Neurons are the basis of an organism's signaling machinery. These cells transmit and receive signals that allow the brain to stimulate the movement of muscles within the body. These cells have numerous processes that emerge from their cell body. The majority of these are branched processes that function to receive signals from neighboring neurons, termed dendrites. Each neuron has a single long extension, referred to as the axon, which is responsible for sending signals to neighboring neurons or directly signaling to muscles. Axonal processes are extremely long relative to the size of the cell, extending up to 1 meter in length in some cases. These processes must be maintained in order to preserve their function, which requires the synthesis of new cellular materials and the capability of ridding these processes of material marked for degradation (Holzbaur, 2004). Because the majority of the machinery required for protein synthesis and degradation is located in the cell body, neurons rely heavily on intracellular transport for delivery of new cellular material to these processes, and the removal of cellular material marked for degradation (Holzbaur, 2004). This specific type of transport is referred to as axonal transport.

Axonal transport occurs on parallel arrays of bundled microtubules within the axon. These microtubules are all oriented such that the plus ends are pointed towards the axon terminal, while the minus ends are oriented close to the cell body (Baas et al., 1988). This enables the organized traffic of newly synthesized material into the cell body primarily by plus end directed kinesin motors and removal of cellular material from the axon by minus end directed dynein motors.

Two distinct processes by which cargos are transported within the axon have been identified. These two transport processes are distinguished by their differing overall rates of transport, and are therefore referred to as fast and slow axonal transport. Cargos transported by both of these processes are actively transported at similar rates, however in slow axonal transport, movement is interrupted by long pauses, slowing their overall transport rates compared to cargos transported by fast axonal transport (Brown, 2003). Fast and slow axonal transport are believed to be carried out by two different transport mechanisms. Fast axonal transport involves the movement of membrane bound organelles by a fixed team of motors. The mechanism which underlies slow axonal transport is less clear, but is thought to be due to the transient self-assembly of proteinaceous cargos with motors along the microtubule (Scott et al., 2011).

In order for cargos to be transported, motors must associate with them in some manner. Motors mediate a variety of attachment mechanisms with cellular cargos, which in part dictates cargo specificity. For kinesin motors, these attachments typically occur via the kinesin light chains (Vale and Fletterick, 1997).

The kinesin light chain is comprised of an N-terminal coiled-coil domain followed by six tetratricopeptide repeat (TPR) motifs (Vale and Fletterick, 1997). The N-terminal coiled-coil domain mediates interactions with the kinesin heavy chain while the TPR domain is responsible for interacting with various cargos (Vale and Fletterick, 1997). There are four different isoforms of the kinesin light chain in humans, KLC1-4. These light chain isoforms have different expression patterns as well as slight structural differences that allow them to have different specificities for cargos (Zhu et al., 2012).

Kinesin motors are thought to bind cargos through an adaptor protein, rather than directly linking to membranous cargos (Figure 1.4). One well-studied example of this is the c-jun N-terminal kinase (JNK)-interacting proteins (JIPs): JIP-1, JIP-2, and JIP-3 (Verhey et al., 2001). These proteins have been shown to be direct cargos of kinesin, as they interact directly with the kinesin light chain TPR domain, an interaction that is required for their distribution within cells (Verhey et al., 2001). JIP proteins are scaffolding proteins for the JNK family of MAP kinases. Thus, by binding to kinesin light chains, these proteins act as a scaffold, bringing together a complex of signaling proteins that can be specifically distributed throughout the cell by kinesin motor activity. In addition, these JIPs were shown to assemble transmembrane proteins that serve as a scaffold for kinesin binding to vesicles and organelles. JNK has been of recent interest in regard to treatments for Parkinson’s Disease, a neurodegenerative disease associated with the death of dopaminergic neurons. Neuronal death is mediated by apoptosis, and recent studies have begun to reveal the role of JNK signaling in the initiation of the apoptotic pathway (Dauer and Przedborski, 2003). Much interest lies in the development of therapies aimed to prevent JNK signaling in patients with Parkinson’s Disease (Dauer and Przedborski, 2003).

Another, more direct interaction between kinesin light chains and cargos that has been observed is through the amyloid precursor protein (APP). APP is a transmembrane protein that has been shown to directly bind to the TPR domain of KLCs (Kamal et al., 2000). This allows for kinesin motors to interact with membranous cargos via APP, and is another mechanism by which kinesin motors can bind and transport vesicular cargos. APP has been strongly associated with the onset and progression of Alzheimer’s Disease, as APP aggregates, or plaques, are often found in the brains of affected patients. These plaque formations are believed to be caused by mutations within the APP gene that promote APP aggregation, an increase in the production of proteolytic fragments of APP that are prone to aggregation, or defects in the transport of APP by molecular motors (Goldstein, 2001).

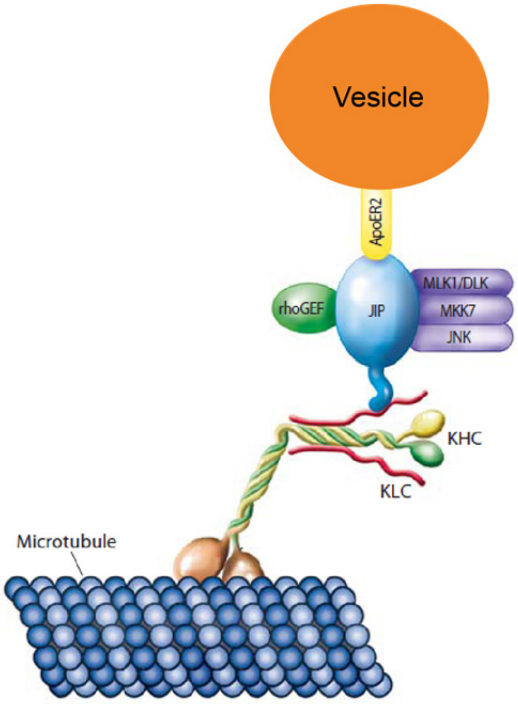

Figure 1.4. Cargo Binding Mechanism of Kinesin-1.

This figure depicts the mechanism by which kinesin-1 binds membranous cargos through the JIP scaffolding protein. JIP acts as a scaffold to bring together signaling molecules and a transmembrane protein (ApoER2, in the case here) that functions to mediate attachments between kinesin motors and membranous cargos. Figure was adapted from (Rutter and Hill, 2006).

While individual motors can travel up to 1 or 2 μm before dissociating from the microtubule, these length scales are small compared to the distances cargos must be transported to reach the ends of axonal processes. To increase the processivity of molecular cargos, multiple motors are often complexed to the same cargo (Gross et al., 2007). These motors can be of the same species, but often include a mix of different motor species. Many studies have been done to understand the impact of multiple motors on the transport of a cargo. To start, these studies were simplified by studying multiple motors of a single motor species attached to a cargo.

Both theoretical and experimental studies have been carried out to probe the effect of multiple kinesin motors on cargo transport. Both theory and experiments showed that by increasing the number of motors bound to a cargo, processivity of these cargos was enhanced (Beeg et al., 2008; Derr et al., 2012; Klumpp and Lipowsky, 2005). This enhancement can be explained by the fact that additional motors bound to a cargo act as a tether when one motor dissociates. For single motors, a dissociation event would mean the end of a processive run. For cargos with multiple motors, when one motor dissociates, the cargo is still bound to the microtubule by other motors, which continue the cargo's processive run. In addition, the dissociated motor is still attached to the cargo, and is therefore held in close proximity to the microtubule, allowing it to easily rebind after its dissociation. This enables cargos to be transported over lengths that are much longer than the run length of a typical single motor.

One discrepancy between theoretical and experimental studies is the degree to which the processivity of these cargos is enhanced. Theoretical work consistently shows greater increases in processivity compared to what is observed in experimental studies (Derr et al., 2012; Klumpp and Lipowsky, 2005; Korn et al., 2009). This suggests that there is some type of negative interference between multiple motors that are bound to a single cargo, which results in shorter run lengths than would be anticipated otherwise. One explanation for this discrepancy is that in multiple motor complexes, the detachment rate of kinesin motors is increased, a property that is not taken into account in theoretical models (Rogers et al., 2009). It is known that kinesin motors bound to the same cargo do not step in synchrony (Leduc et al., 2007). This asynchronous stepping would likely lead to a generation of forces within the motor-cargo complex (Rogers et al., 2009). A cargo transported by just two motors can be used as an example here. If the leading motor is stepping faster than the trailing motor, strain will be generated, stretching both motors. This generation of strain within the complex is thought to increase the unbinding rate of motors (Rogers et al., 2009). Thus, cargos transported by N motors often have less than N motors engaged with the microtubule, as many would often be in the unbound state. This would explain why experimental studies show shorter than expected run lengths compared to results generated by simplified theoretical studies.

In addition, it has been shown that the velocity of cargos is independent of motor number. Cargos with variable numbers of motors have been shown to be transported at velocities identical to those of single motors (Beeg et al., 2008; Derr et al., 2012; Herold et al., 2012; Rogers et al., 2009). This suggests that the presence of multiple motors on a cargo does not interfere with the stepping rate of kinesin motors.

One hallmark of axonal transport is the bidirectional transport of cargos (Schnapp et al., 1985). These cargos exhibit frequent reversals in direction during their transport. These reversals are attributed to the presence of two oppositely directed motors bound to one cargo. For example, kinesin and dynein are often bound to the same cargo (Welte, 2004).

How oppositely directed motors cooperate to transport a cargo has been the focus of many recent studies. Two main hypotheses in the field are that bidirectional transport is regulated by 1) a tug-of-war mechanism or 2) a mechanism where motor activity is regulated such that only a single motor species is engaged at one time (Gross, 2004).

In the tug-of-war model, oppositely directed motors bound to a cargo each walk in their own direction, creating a tug-of-war between the two motor species. Assuming the two sides are not perfectly balanced in the amount of force they are capable of generating, one side (one motor species) will win, determining the direction in which the cargo is transported. The amount of force generated by each side can be finely tuned by the number of motors and the amount of force each motor type is capable of producing. For instance, because the stall force of kinesin-1 is on the order of 5-6 pN (Svoboda et al., 1993), whereas the stall force of dynein is only approximately 1.1 pN (Mallik et al., 2004), the number of dynein motors on a cargo would have to exceed that of kinesin by about 6- or 7-fold in order to win a tug of war (Hendricks et al., 2010). Changes in the number of motors bound during transport could result in directional reverses mid-transport, as are observed in the bidirectional transport of cargos.

The second model used to describe bidirectional motility of cargos is that motors are regulated by an external factor. In this model, one motor species would be inactivated, allowing the other motor species to dominate motility. Factors that have been suggested to regulate motor activity include proteins or molecules that alter the recruitment of motors to a cargo, or scaffolding molecules that specifically tune the activity of motors (Hendricks et al., 2010). In the case of kinesin motors, it has been proposed that motor activity could be regulated by factors that promote or relieve the autoinhibition state of motors bound to cargo (Hendricks et al., 2010).

The tug-of-war model is supported by a number of studies which aim to identify and quantify motor species bound to endogenous cargos. These studies have shown that there is an approximate 6:1 ratio of dynein:kinesin motors bound to membranous cargos in cells (Hendricks et al., 2010; Soppina et al., 2009). Given the forces that dynein and kinesin motors are able to produce, this ratio makes it conceivable that a cargo could be transported in the direction of either kinesin or dynein motors, as is expected by the ability of these cargos to spontaneously switch directions. One study compared the bidirectional motility of purified neuronal transport vesicles in vitro to their motility in cells (Hendricks et al., 2010). These studies showed that there were no significant differences in motility in vitro versus in vivo. Thus, this suggests that the bidirectional motion observed was due to a tug-of-war mechanism, and not due to the presence of cytoplasmic regulators that tune the activity of a particular motor species. However, in this same study, there was a small subset of cargos that were observed to move predominantly in one direction in cells. This type of motility was not observed with purified cargos studied in vitro, suggesting that this subset of cargos is regulated by a mechanism which requires cytosolic regulatory factors. Therefore, this study proposes that both a tug-of-war mechanism as well as a mechanism that regulates specific motor activities exist to coordinate bidirectional transport in cells. Which cargo types, or when cargos are regulated by each of these mechanisms remains unknown. Additionally, the identification of factors that regulate motor coordination remains an open area of study.

Intracellular transport is a highly complex process that must be tightly regulated and controlled to enable the efficient and proper distribution of cargos throughout the cell. While the above studies have provided insights into how this process works, studies aimed at achieving a better understanding of how intracellular transport is regulated in the cell are imperative to fully understand the mechanisms that underlie this process.

1.5 Neurodegenerative Disease

The importance of intracellular transport is emphasized by the association between defects in axonal transport and neurodegenerative disease. Mutations in microtubule motors that disrupt motor motility have been associated with neurodegenerative disease (Perlson et al., 2010). Such disruptions in motor motility prevent the proper transport of newly synthesized material into the axon and the proper transport of material that must be degraded out of the axon. This has been shown to result in the degeneration of axons, which inhibits signaling between neurons and leads to the classic symptoms of neurodegenerative disease, such as paralysis and dementia.

One disease caused by neurodegeneration is hereditary spastic paraplegia. While this disease is typically caused by mutations in the spastin gene, there have been three autosomal dominant missense mutations described in the KHC gene of kinesin-1 that cause this disease as well (Chevalier-Larsen and Holzbaur, 2006). These mutations are believed to prevent microtubule activation of ATP hydrolysis, affect the affinity of kinesin for microtubules, and disrupt dimerization of kinesin-1. Thus, these mutations severely disrupt kinesin-1 motility. Patients with this disease exhibit distal axon degeneration, a result of anterograde transport disruption.

Cytoplasmic dynein mutations have also been implicated in neurodegenerative disease. Patients with a mutation in the gene encoding the dynactin subunit, p150$^{\text{Glued}}$, exhibit a late-onset, slowly progressive form of the motor neuron disease, distal hereditary motor neuropathy type VIIB (Perlson et al., 2010). These patients experience adult-onset vocal fold paralysis, facial weakness, and distal limb muscle weakness and atrophy. This particular mutation disrupts the folding of p150$^{\text{Glued}}$, causing dynein to have a decreased affinity for the microtubule. In addition, this misfolding results in the formation of aggregates of this protein. These cells experience both a loss of function of dynein and accumulate toxic aggregates, which could further disrupt axonal transport. Together, these defects lead to neuronal degeneration.

Defects in axonal transport are observed in a number of other neurodegenerative diseases, including Alzheimer's disease and Parkinson's disease (Perlson et al., 2010). Whether defective motor transport is the cause of these diseases, or rather a result of changes in the cell due to these disease states is unclear. If defects in motor transport are not the root cause, they are thought to at least contribute to the disease state (Perlson et al., 2010).

Mutations in microtubule motor proteins exhibit clear implications in the onset and progression of neurodegenerative disease. The study of these motors to better elucidate their mechanisms of transport along microtubules will help to gain a more clear understanding of how these motors could be perturbed in disease states.

1.6 Motivation

The numerous studies described above have provided the field with a fundamental understanding of the mechanisms by which kinesin motors are able to walk processively along microtubules, with or without cargos. The majority of these studies have used a bottom-up approach, studying purified kinesin motility on microtubule tracks comprised of purified tubulin subunits. This approach has allowed for the study of motor motility under consistent conditions, without any heterogeneities that could arise from factors present in the cellular environment. These studies have developed a thorough understanding of how kinesin coordinates its processive motion along microtubule tracks in vitro.

To fully understand kinesin motility, we must understand how these motors function in the cell. The cell presents extremely complex microtubule tracks that kinesin motors must navigate. These microtubules are coated with microtubule associated proteins (MAPs), microtubule motor proteins, and post-translational modifications that regulate the binding of these MAPs and motors. In addition, MAPs and motors bound to microtubules regulate the microtubule architecture in cells, often stimulating the formation of microtubule bundles.

How kinesin motors navigate these complex microtubule tracks will be the focus of this dissertation. I aim to build on the complexity of previous in vitro assays to study kinesin motility on microtubules crowded with microtubule motor proteins and on a common microtubule architecture found in cells, microtubule bundles. In addition, I aim to gain a better understanding of how particular residues in the kinesin motor domain contribute to the processive motility of kinesin motors required for the transport on microtubule tracks. With this work, I provide new insights into how kinesin motors maintain processivity, even on complex microtubule tracks similar to those that could be encountered in the cell.

CHAPTER 2

MOTOR TRANSPORT OF SELF-ASSEMBLED CARGOS IN CROWDED ENVIRONMENTS

This section was performed together with Derek Wood, Erkan Tüzel, and Jennifer L. Ross (Conway and Ross, 2013; Conway et al., 2012). Derek Wood modified an existing particle tracking code (provided by Maria Kilfoil) to be used for the analysis of the self-assembled quantum dot cargos in this study. Erkan Tüzel has been working on modeling the system described here and participated in many valuable discussions regarding the interpretation of the results observed in my experimental system.

2.1 Introduction

The motility properties of kinesin-1 have been well characterized using in vitro assays. These assays have been used to understand the transport properties of both single kinesin motors and cargos carried by multiple kinesin motors (Beeg et al., 2008; Block et al., 1990; Romberg et al., 1998; Vale et al., 1996; Yildiz et al., 2004). While these studies have provided valuable insights into the mechanisms by which kinesin-1 is able to walk along microtubules, these studies were done on microtubules assembled *in vitro*, devoid of additional motors or microtubule associated proteins (MAPs). These conditions are very different from what motors must face in the cell, where microtubules are crowded with motors and MAPs (Gross et al., 2007).

Despite the crowded conditions motors face in the cell, cargo transport is still carried out efficiently, as it must since this is an essential process for the survival of all cell types (Hirokawa, 1998). How motors ensure this efficient transport on crowded microtubules is still unclear. Several recent studies have begun to shed light on this question. It has been shown that while stationary obstacles, such as the microtubule associated protein tau, disrupt kinesin processivity by causing motors to dissociate prematurely from the microtubule (Dixit et al., 2008; Ross et al., 2008; Telley et al., 2009; Vershinin et al., 2007), cargos transported by multiple motors were able to better handle these obstacles (Vershinin et al., 2007).

How kinesin motors navigate microtubules with motile obstacles, or traffic, is not well understood. Here, I study the transport of both single kinesin motors and artificial Qdot cargos transported by multiple kinesin motors on microtubules crowded with additional motors. I show that motor traffic along the microtubule results in a decrease in both single motor and cargo velocity. Additionally, I observe that single motor processivity is reduced on crowded microtubules while cargos are still able to be transported over long distances, as was observed previously for static obstacles (Vershinin et al., 2007). Cargos are able to navigate microtubules crowded with high densities of motors by associating new motor attachments that allow them to remain tethered to the microtubule longer. I also speculate that new motor attachments on adjacent protofilaments could allow cargos to switch protofilament tracks to circumvent obstacles. These studies provide insights into how cargo transport is tuned to ensure efficient transport of cargos on tracks crowded with motile obstacles.

2.2 Results

2.2.1 Experimental Set-Up

To study motor motility on crowded microtubules, different densities of unlabeled motile kinesin motors were used to crowd the microtubule surface. Single GFP-tagged kinesin motors or kinesin motors bound to artificial Qdot cargos were added to crowded microtubules to observe motility of single motors and cargos, respectively.

Kinesin motors were initially attached to Qdot cargos through a specific streptavidin-biotin linkage. To accomplish this, a HaloTag (Promega) was fused to the C-terminal end of the K560 human kinesin-1 construct. This 34 kDa tag forms a covalent bond with a variety of HaloTag ligands. Here, I used a PEG-biotin HaloTag ligand and streptavidin conjugated Qdots to initiate the formation of Qdot-kinesin complexes.

During the formation of these Qdot-kinesin complexes, Qdots were added in a 10-fold molar excess over kinesin. This ratio ensured the formation of Qdots with few kinesin bound, such that on average only one kinesin motor was able to interact with the microtubule at a time. To verify that single molecule levels of motors were bound to Qdot cargos, motility properties of single GFP-tagged kinesin motors were compared to those of Qdot-kinesin complexes on uncrowded microtubules. Because there is a pronounced increase in the observed run length of a cargo transported by two or more motors compared to a cargo transported by a single motor (Beeg et al., 2008; Block et al., 1990; Klumpp and Lipowsky, 2005; Korn et al., 2009; Kunwar et al., 2008; Muller et al., 2010; Vershinin et al., 2007), the distance a cargo is transported can be used to determine whether there are single or multiple motors bound to a cargo. I observed that single kinesin motors and Qdot-kinesin complexes had nearly identical run lengths (Figure 2.1A), indicating that Qdot cargos were transported by a single motor under these conditions.

However, when Qdot-kinesin complexes were added onto microtubules crowded with excess non-biotinylated kinesin motors, I found that these same Qdot cargos were transported distances greater than those observed on uncrowded microtubules (Figure 2.1B). These longer run lengths indicate that multiple motors associate with a single cargo on microtubules crowded with excess kinesin motors. Thus, I infer that when Qdot-kinesin complexes are added onto microtubules crowded with excess non-biotinylated motors, these excess motors are able to form non-specific interactions with Qdot cargos, resulting in the self-assembly of Qdot cargos that are transported by multiple motors.

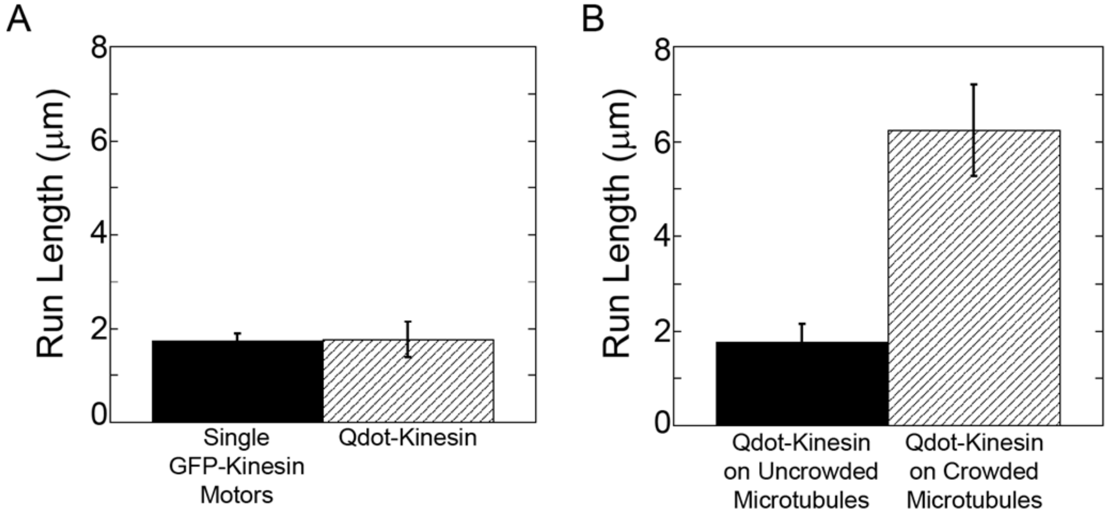

Figure 2.1. Run Length Comparison to Distinguish Single Motor versus Multi-Motor Qdot Cargos

A. Mean run length of single GFP-kinesin motors (N = 101) versus Qdot-kinesin complexes (N=19) on uncrowded microtubules. Error bars represent standard error of the mean. **B.** Mean run length of Qdot-kinesin complexes on uncrowded microtubules (N = 19) versus Qdot-kinesin complexes on microtubules crowded with 200 nM kinesin (N = 36). Error bars represent standard error of the mean.

Interestingly, these non-specific interactions occurred not only between non-biotinylated HaloTag motors and Qdots, but between GFP-tagged kinesin motors and Qdots as well. When Qdots were added to microtubules coated with 50 nM GFP-kinesin (no biotinylated kinesin present), I saw that Qdots were able to translocate efficiently along microtubules (Figure 2.2). This suggests that this interaction is not specific to the HaloTag and further demonstrates that biotin is not required for this non-specific interaction.

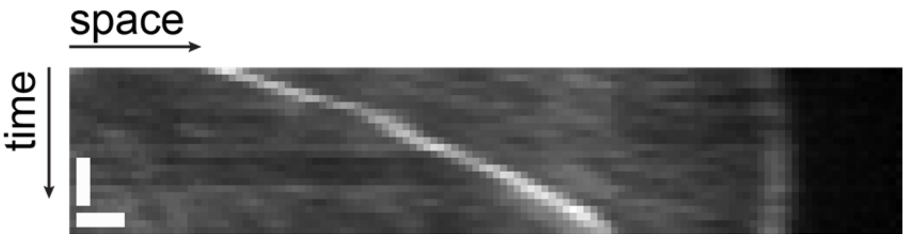

Figure 2.2 Qdots are Transported by Non-Biotinylated Kinesin Motors

Kymograph showing a Qdot transported on a microtubule coated with 50 nM GFP-kinesin. The kymograph was extended beyond the length of the microtubule in order to visualize the increased fluorescence intensity along the entire length of the microtubule due to the presence of GFP kinesin. Vertical scale bar is 21 seconds. Horizontal scale bar is 0.5 μm.

2.2.2 Non-Biotinylated Motors Transiently Interact with Qdot Cargos

While I was able to show that non-biotinylated kinesin motors can form non-specific interactions with Qdots, it is unclear how these non-specific interactions participate in the transport of Qdots. Do these motors bind the Qdot cargo and remain bound throughout the entire duration of Qdot transport or are they able to associate and dissociate throughout this transport process? Do motors bind and actively transport Qdots or do they weakly bind Qdots and act more like a conveyor belt over which the Qdot is passed along?

To better understand the nature of this non-specific interaction between non-biotinylated kinesin motors and Qdot cargos, I performed two-color single molecule experiments to visualize interactions between GFP-kinesin motors and 655 nm streptavidin Qdots during transport. These experiments were done on microtubules coated with a medium density of non-biotinylated kinesin motors (50 nM kinesin). I added 10% GFP-kinesin motors to non-biotinylated HaloTag kinesin motors to allow for the visualization of individual GFP-kinesin motors. In these assays, I witnessed events where a GFP-kinesin motor associated with a Qdot already bound to the microtubule (Figure 2.3A, B). I also observed events where a GFP-kinesin motor dissociated from a Qdot during transport (Figure 2.3C), events where a Qdot and GFP-kinesin bound the microtubule simultaneously, presumably already in complex (Figure 2.3D), events where a Qdot and GFP-kinesin dissociated from the microtubule simultaneously (Figure 2.3E), and events where a Qdot bound a GFP-kinesin motor already associated with the microtubule (Figure 2.3F).

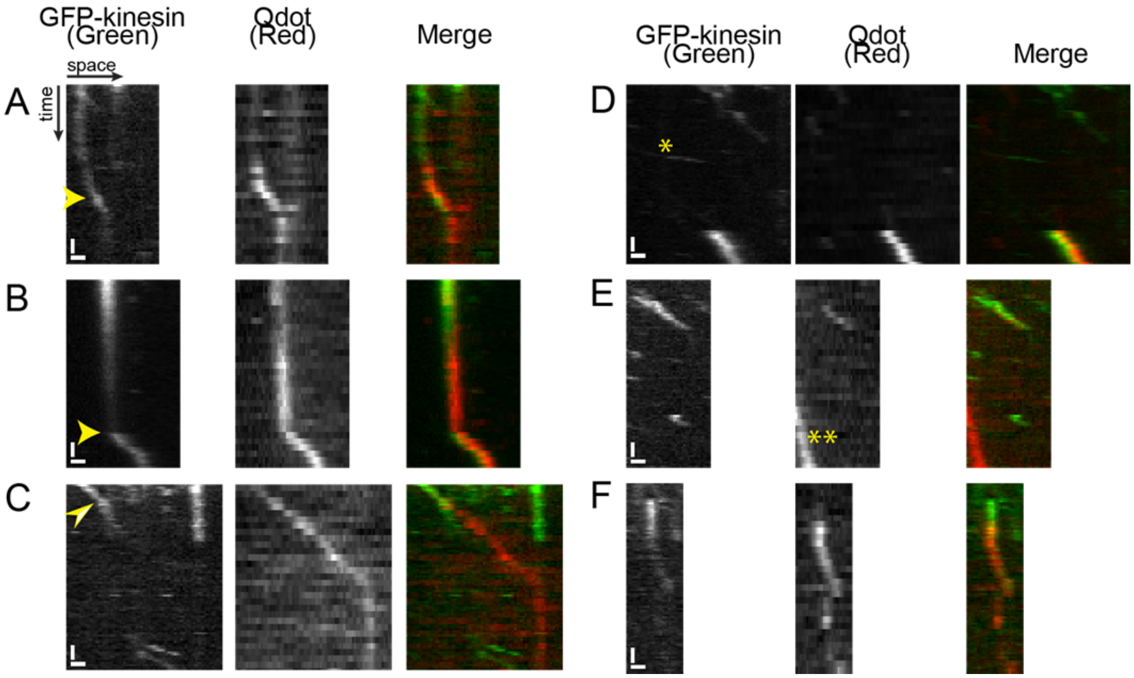

Figure 2.3 Two-Color Single Molecule Assays Show Association and Dissociation of Kinesin Motors to Qdot Cargos

A-F. Example kymographs depicting various ways in which Qdots were observed to associate or dissociate GFP-kinesin motors while translocating along the microtubule. Left kymographs show GFP-kinesin motility, middle kymographs show Qdot motility, and right kymographs show a merge of the two channels. Scale bars in the vertical direction are 10 s and in the horizontal direction are 0.5 µm. **A,B.** GFP-kinesin motor is observed to associate with a Qdot already bound to the microtubule. GFP-kinesin binding event is indicated by arrow head. **C.** GFP-kinesin motor is observed to dissociate from a Qdot while the Qdot is moving along the microtubule. GFP-kinesin dissociation event is indicated by arrow head. **D.** Qdot and GFP-kinesin are observed to bind the microtubule simultaneously. Single GFP-kinesin motors not associated with Qdots are also observed on the same microtubule (*). **E.** Qdot and GFP-kinesin are observed to dissociate from the microtubule simultaneously. A second Qdot is transported by unlabeled kinesin motors only (**). **F.** Qdot is observed to bind directly to a GFP-kinesin already bound to the microtubule.

In many cases, I observed that GFP-kinesin motors associated with Qdots walked with the Qdot during transport. From these experiments, I show that non-biotinylated kinesin motors form transient interactions with Qdots, as they are able to associate and dissociate with Qdot cargos during transport. In addition, I show that when a kinesin motor non-specifically binds a Qdot cargo, it can remain in complex with the Qdot to actively aid in its transport along the microtubule.

To further probe the interaction between non-biotinylated motors and Qdots, I investigated the binding affinity of non-biotinylated motors to Qdots. First, I used biotinylated polystyrene beads to perform bulk binding assays to pull down streptavidin Qdots and any Qdot-bound kinesin. I mixed biotinylated beads with 250 nM streptavidin Qdots and increasing concentrations of non-biotinylated HaloTag kinesin-1. After incubation, beads were pelleted to pull down streptavidin Qdots, and supernatant and pellet samples were run on a gel. Using both coomassie staining and western blotting, I was unable to detect any kinesin-1 bound to Qdots in these bulk binding assays (Figure 2.4A,B). These results suggest that binding of non-biotinylated motors to Qdots in solution is rare. Because I observed binding events often in my assays, I used my experimental set-up to determine the affinity of non-biotinylated motors for Qdots using a visual binding assay. I added 50 nM non-biotinylated HaloTag kinesin to microtubules and increasing concentrations of Qdots to these kinesin-coated microtubules. Qdots were visualized in TIRF and the ratio of bound Qdots to kinesin was determined (Figure 2.4C). From this data, I was able to calculate the K_D for Qdot binding to kinesin to be 1.3 mM. This low affinity further demonstrates the transient nature of the interaction between non-biotinylated kinesin motors and Qdots.

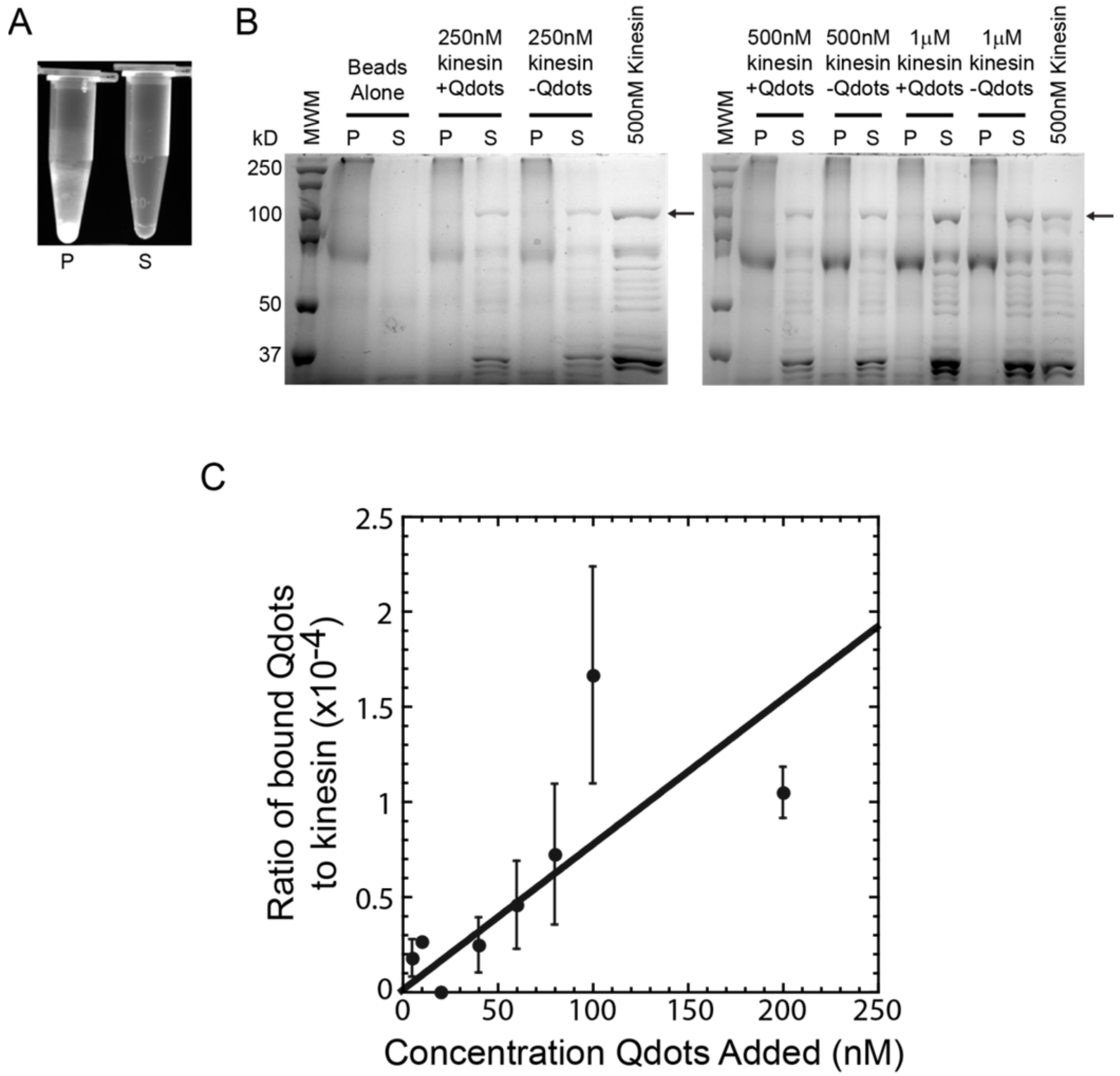

Figure 2.4 Binding Constant Estimate for Qdots Binding to Non-Biotinylated Kinesin

A. After Qdot incubation with biotinylated beads, sample is centrifuged to pellet beads. After separation of supernatant and pellet, samples were illuminated with UV light to fluoresce Qdots and determine their location. Left tube shows bead pellet with bound Qdots, right shows supernatant without Qdots. **B.** Coomassie stained SDS-PAGE gels showing pellet and supernatant samples. For all concentrations of kinesin added, kinesin is detected only in the supernatant (arrows, ~100 kD band). **C.** Ratio of bound Qdots to kinesin as a function of the concentration of Qdots added. Because so few Qdots were found to bind to kinesin along microtubules, I estimate the concentration of free Qdots is equal to the concentration of Qdots added. The measurements made were in the linear regime of binding. The data was fit to the linear equation: $y = mx$, which was fit best when $m = 7 \pm 1 \times 10^{-7}$ nM^{-1}, $R^2 = 0.5$. The inverse of this slope was used to estimate the affinity of kinesin for microtubules, which was found to be 1.3 mM. Error bars represent the standard error of the mean. Large error bars are a result of many microtubules with zero Qdots bound.

In my experiments, I started with Qdots that were specifically conjugated to a single kinesin motor through a specific streptavidin-biotin linkage. How many motors ultimately transport a single cargo on microtubules crowded with excess kinesin is unknown, as many new motors associate due to non-specific interactions. To estimate the number of kinesin motors that non-specifically bind Qdot cargos on microtubules with 50 nM non-biotinylated kinesin, I again used the two-color single molecule assay. In these experiments, I observed two populations of GFP-kinesin motors: those that were associated with Qdots and those that traveled separately as single motors (Figure 2.3.D). In the cases where GFP-kinesin motors were associated with Qdots, I could compare the intensity in the GFP-channel to the intensity of a single GFP-kinesin moving along the same microtubule. From these measurements, I was able to estimate the number of GFP-kinesin motors associated with each Qdot (Figure 2.5, green data). I observed that the highest percentage of Qdots were associated with zero GFP-kinesin motors and that the data decreased with increasing numbers of associated GFP-kinesin motors. However, in the case of 5 and 6+ GFP-kinesin motors, the data is increased compared to 3 and 4 motors. The increase observed for 6+ GFP-kinesin motors is an artifact as this includes all data for 6 motors and greater. The increase observed for 5 motors could be due to the presence of aggregated GFP-kinesin motors associated with Qdots.

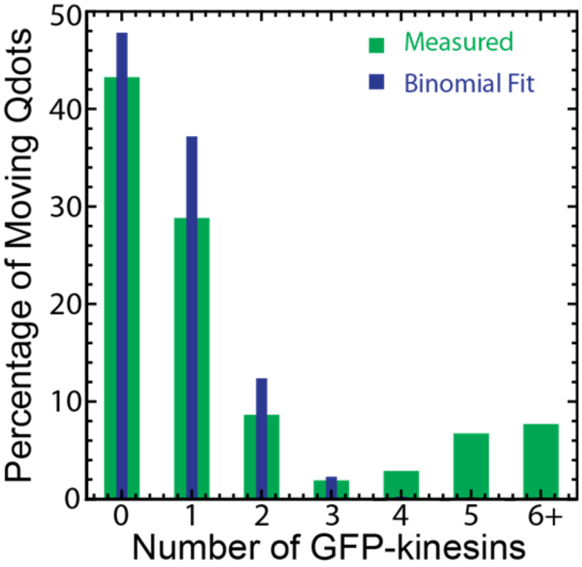

Figure 2.5 Number of Kinesin Motors Bound to Qdot Cargos

Histogram representing the number of GFP-kinesin motors bound to Qdots. Green data represents measurements from the two-color assays. Blue data represents the binomial fit used to estimate the total number of kinesin motors bound to Qdots in these experiments.

Because only 10% of the motors in this experiment were GFP-tagged, this quantification only represents a small population of the motors. To estimate the total number of kinesin bound to each Qdot, taking into account the HaloTag kinesin that is not visible, I fit the measured data to a binomial distribution. A binomial distribution is a discrete probability distribution that describes the possible ways of achieving a certain population size. This function is expressed as follows:

$$\begin{pmatrix} N \\ n \end{pmatrix} p^{n}(1-p)^{N-n}$$

Here, *N* refers to the population size; *n* refers to the sample size; and *p* is the sampling probability. In this function, the binomial coefficient:

$$\begin{pmatrix} N \\ n \end{pmatrix}$$

is referred to as 'N choose n'. This expression is defined as follows:

$$\frac{N!}{n!\,(N-n)!}$$

'N choose n' refers to the fact that there are *n* ways to achieve *N*. For example, if there were 2 motors on each Qdot cargo (*N* = 2), there could be 2 GFP-kinesin and 0 unlabeled kinesin; 1 GFP-kinesin and 1 unlabeled kinesin; or 0 GFP-kinesin and 2 unlabeled kinesin. These are the different possible ways to have *N* = 2 motors on the Qdot cargo.

In the case of this experiment, the population size, *N*, which is the total number of kinesin motors (labeled and unlabeled) on each Qdot cargo is unknown. To determine this population size, I sampled the number of kinesin motors on Qdot cargos by counting the number of GFP-kinesin motors. This measured data is therefore the sample size, *n*.

Because 10% of the motors added were GFP-tagged, the probability, *p*, of sampling one of these GFP-kinesin motors in this experiment is 10%.

Using these values, I calculated the binomial distribution for discrete values of N. For each of these distributions, I used a chi-squared test to calculate the goodness of fit:

$$\chi^2 = \sum \frac{(O - E)^2}{E}$$

For $N = 6$ motors, I calculated a χ^2 value of 0.03451. For $N = 7$ motors, I calculated a χ^2 value of 0.03435. For $N = 8$ motors, I calculated a χ^2 value of 0.05284. Because the lowest χ^2 value corresponds to the best fit, I found that the data was fit best when $N = 7$. Therefore, I determined that on average, there are a total of 7 motors bound to each Qdot in these experimental conditions.

2.2.3 Motor Density on Crowded Microtubules

To understand how different levels of crowding affect the transport of single motors and cargos, I probed motility on microtubules crowded with different concentrations of excess kinesin motors, ranging from 1 nM (not crowded) to 200 nM (highly crowded). To determine the actual levels of crowding for each condition, I calculated the motor density along these microtubules. GFP-tagged kinesin was added to microtubules at concentrations used in my experiments and kinesin binding to microtubules was visualized using TIRF microscopy. The fluorescence intensity along microtubules at each density was compared to the intensity of a single GFP-kinesin motor to estimate the number of motors bound per micron of microtubule. I observed a linear increase in motor density as the kinesin concentration was raised (Figure 2.6).

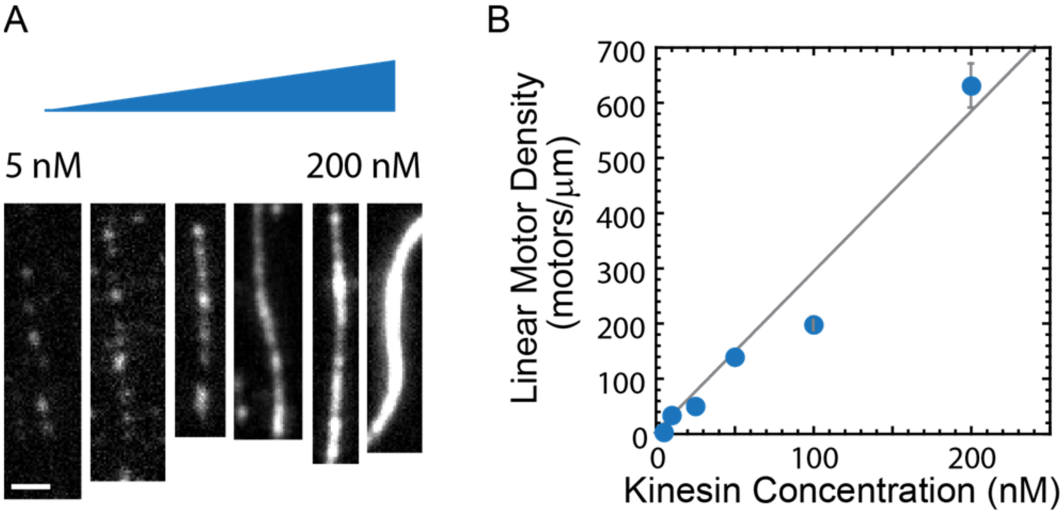

Figure 2.6 Motor Density on Crowded Microtubules

A. Representative images of GFP-kinesin binding along microtubules at 5, 10, 25, 50, 100, and 200 nM kinesin. Due to increasing levels of kinesin, these images are displayed with different linear look-up tables. For 5 and 10 nM, the gray scale is from 0 to 1,000 on a 16-bit scale. For 25 nM, the gray scale is from 0 to 2,500. For 50 and 100 nM, the gray scale is from 0 to 5,000. For 200 nM, the gray scale is from 0 to 10,000, which is saturated. Single GFP-kinesin motors are clearly visible at 5 and 10 nM. Scale bar is 1 μm. **B.** Linear motor density of GFP-kinesin along the microtubule as a function of added GFP-kinesin. N = 50 microtubules for each density. Error bars represent standard error of the mean. The data was fit to the linear equation: $y = mx$ which was fit best when $m = 2.9 \pm 0.2$, $R^2 = 0.96$.

At the highest kinesin concentration added (200 nM), I calculated that approximately 40% of the kinesin binding sites are saturated.

Using this data, I was also able to calculate the K_D value for kinesin binding to microtubules in my assays. I plotted the ratio of bound kinesin to tubulin dimers against the concentration of free kinesin (Figure 2.7).

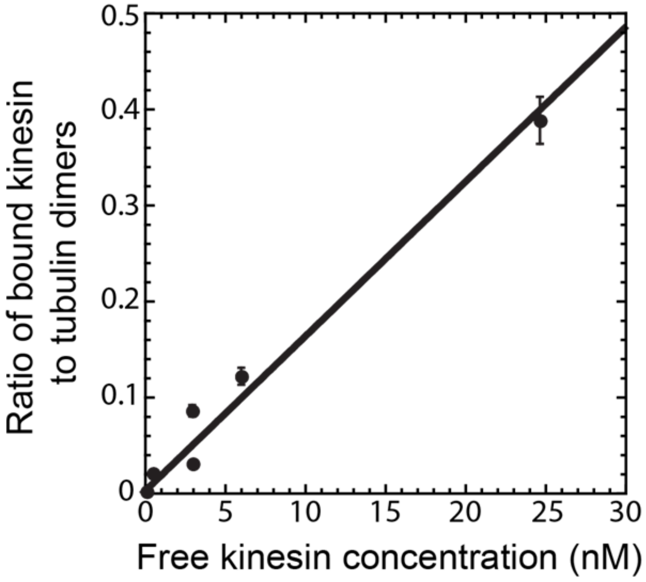

Figure 2.7 Binding Constant Estimate for Kinesin Binding to Microtubules

Ratio of bound kinesin to tubulin dimers plotted as a function of free kinesin concentration. The measurements made were in the linear regime of binding. The data was fit to the linear equation: $y = mx$, with the fit being best when $m = 0.0161 \pm 0.0009$ nM^{-1}, $R^2 = 0.97$.

The ratio of bound kinesin to tubulin dimers was determined by dividing the number of GFP-kinesin motors bound per μm of microtubule by the total number of tubulin dimers in 1 μm of microtubule (1625 tubulin dimers). The concentration of free GFP-kinesin was determined using the intensity of background GFP fluorescence for each chamber. I observed the relationship of the ratio of bound kinesin to tubulin dimers versus the concentration of free GFP-kinesin to be linear. To determine the K_D value for kinesin binding to microtubules, I used the following equation that describes the relationship between the ratio of bound kinesin, the concentration of free kinesin, the stoichiometry (S) of kinesin binding to tubulin, and the K_D:

$$ratio = S\frac{[kinesin_{free}]}{K_D + [kinesin_{free}]}$$

Because I observed a linear relationship between the ratio of bound kinesin versus free kinesin, I was not at saturating concentrations and can assume that I was in the dilute regime. In this dilute regime, I can make the assumption that the $[kinesin_{free}]$ is << K_D. Therefore, in the above equation, the denominator approaches K_D and the ratio of bound kinesin is a linear function of $[kinesin_{free}]$:

$$ratio = \frac{S}{K_D}[kinesin_{free}]$$

Here, the slope of this linear equation is equal to S/K_D. Because the stoichiometry (*S*) of kinesin binding to tubulin dimers is 1 motor head per 1 tubulin dimer, I know that the slope is equal to $1/K_D$. I fit the data to the linear equation: $y = mx$ and found that the data was fit best when $m = 0.0161 \pm 0.0009\ \text{nM}^{-1}$ ($R^2 = 0.97$). Because the slope, *m*, is equal to the inverse of the K_D, I was able to calculate the K_D of kinesin binding to microtubules to be 62 nM.

2.2.4 Motility of Single Motors versus Cargos on Crowded Microtubules

When single motors and cargos were added onto microtubules crowded with excess kinesin, distinct differences in motility were observed for both as crowding was increased (Figure 2.8). Interestingly, single motors and cargos behaved very differently from each other on crowded microtubules.

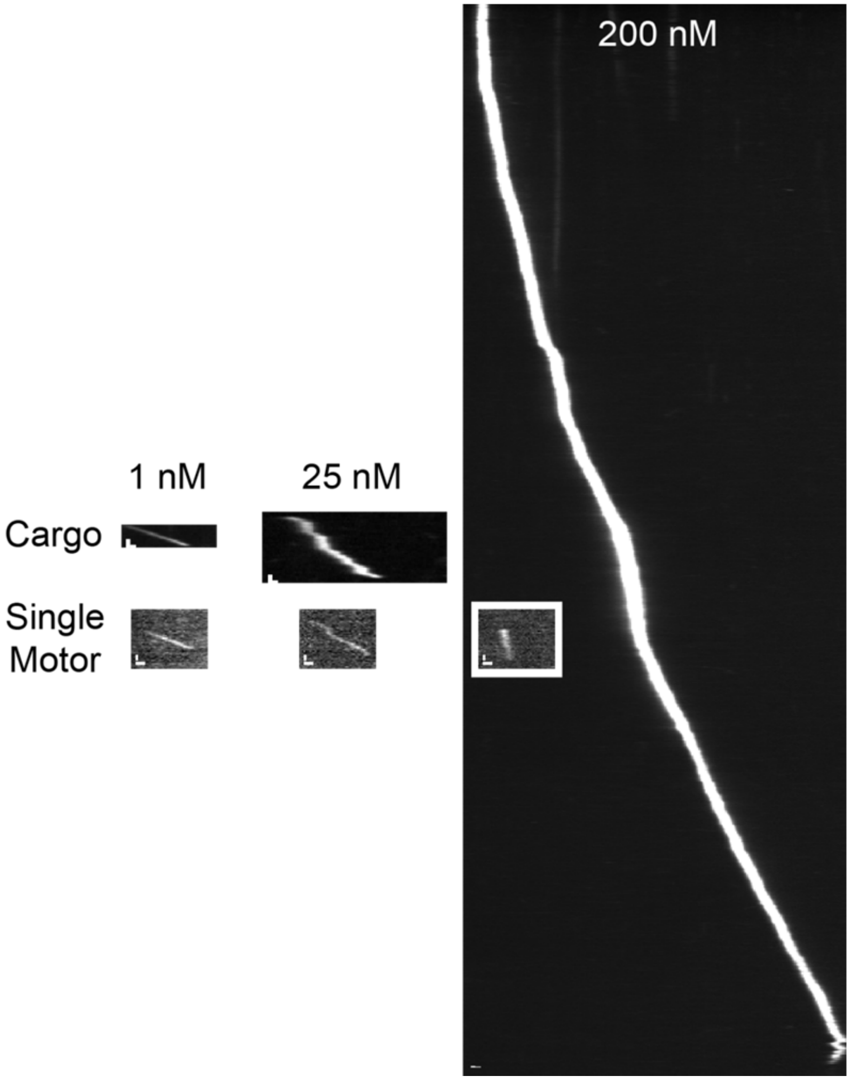

Figure 2.8 Representative Kymographs Showing Motility of Cargos versus Single Motors on Microtubules with Different Levels of Crowding

Kymographs showing cargo or single motor motility on microtubules with 1 nM, 25 nM, or 200 nM excess kinesin. Top kymographs show Qdot cargo motility, bottom kymographs show single GFP-kinesin motor motility. All kymographs are on the same scale. Vertical scale bars are 2 sec and horizontal scale bars are 0.5 μm.

As crowding was increased, I observed that single motor processivity was drastically reduced (Figure 2.9A). Single motors had run lengths of 1.75 μm on uncrowded microtubules, and these run lengths dropped to 0.23 μm on microtubules crowded with 200 nM kinesin. Conversely, cargo processivity was enhanced on crowded microtubules. On uncrowded microtubules, cargos were transported 1.75 μm, likely by a single motor that was initially attached to the Qdot cargo. However, on microtubules crowded with 200 nM kinesin, cargo run lengths increased to an average of 6.23 μm. This increase in processivity observed for cargos indicates that cargos are more likely to associate additional motors through non-specific interactions on crowded microtubules. These additional motors are able to help cargos navigate traffic better, allowing them to be transported over greater distances than if they were transported by a single motor.

Similarly, I observed that the total association time of cargos was enhanced on crowded microtubules as well (Figure 2.9B). On uncrowded microtubules (1 nM kinesin), cargos remained bound to the microtubule for an average of 8.23 seconds, while on crowded microtubules (200 nM kinesin), this association time was increased to 99.27 seconds. For single motors, I observed essentially no change in the total association time as microtubules became more crowded (Figure 2.9B).

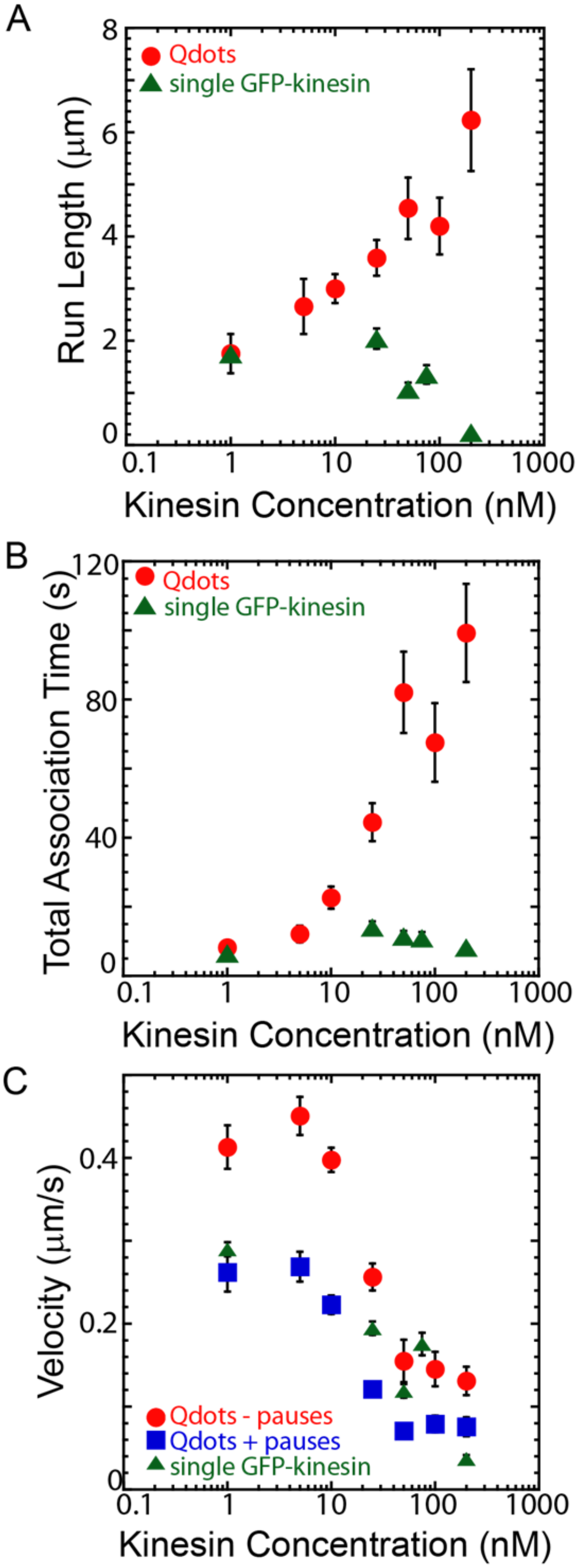
A
Qdots
single GFP-kinesin
Run Length (µm)
0
2
4
6
8
0.1
1
10
100
1000
Kinesin Concentration (nM)
B
Qdots
single GFP-kinesin
Total Association Time (s)
0
40
80
120
0.1
1
10
100
1000
Kinesin Concentration (nM)
C
Velocity (µm/s)
0
0.2
0.4
Qdots - pauses
Qdots + pauses
single GFP-kinesin
0.1
1
10
100
1000
Kinesin Concentration (nM)

Figure 2.9 Motility Properties of Single Motors and Cargos on Crowded Microtubules

A. Run length was measured as the total distance traveled. Red circles show Qdot cargo data, green triangles show single GFP-kinesin motor data. **B.** Total association time was measured as the total time motors or cargos remained bound to the microtubule. Red circles show Qdot cargo data, green triangles show single GFP-kinesin data. **C.** Velocity was measured in two ways: the overall velocity where the total run length was divided by the total association time (blue squares, Qdot cargos and green triangles, single GFP-kinesin motors). Second, for Qdot cargos, velocity was measured by averaging only the moving segments of runs, omitting all pauses (red circles). For all plots, N values for Qdot cargo measurements: [1 nM (N = 19); 5 nM (N = 36); 10 nM (N = 138); 25 nM (N = 106); 50 nM (N = 49); 100 nM (N = 22); 200 nM (N = 36)] and for single GFP-kinesin measurements: [1 nM (N = 101), 25 nM (N = 104); 50 nM (N = 55); 75 nM (N = 54); 200 nM (N = 103)]. Error bars represent standard error of the mean for all plots.

While single motors and cargos exhibited opposite motility properties in terms of run length and total association time, I observed similar trends in the velocity of single motors and cargos on crowded microtubules (Figure 2.9C). Velocity was first calculated by dividing the total distance traveled by the total association time of motors. I saw that single motors moved at velocities of 0.29 μm/sec on uncrowded microtubules and slowed to 0.04 μm/sec on crowded microtubules (200 nM kinesin). Similarly, I observed cargo velocities of 0.26 μm/sec on uncrowded microtubules and slower velocities of 0.08 μm/sec on crowded microtubules (200 nM kinesin). Because I observed cargos to pause more frequently on crowded microtubules (as discussed in section 2.2.5), I wanted to determine whether this decrease in cargo velocity observed was due to motors actually moving slower, or whether it was an artifact of increased pausing. To differentiate between these two possibilities, I calculated the velocity by averaging only the moving segments of each run, thereby omitting any pauses from this measurement. I found that the velocities calculated were increased compared to velocity measurements including pauses. However, I still observed the same trend that the velocity of cargos is slowed on crowded microtubules (Figure 2.9C). This shows that both single motors and cargos move slower in the presence of traffic, and this decrease in velocity is not due to merely pausing more frequently on these crowded microtubules.

2.2.5 Qdot Cargos Exhibit Pausing on Crowded Microtubules

As mentioned previously, I observed an increased frequency of pausing of cargos transported on crowded microtubules. While these pauses were distinct in some cases, for cargos moving at slow velocities, it was difficult to distinguish between a pause and slow motion by eye (Figure 2.10A, left kymographs).

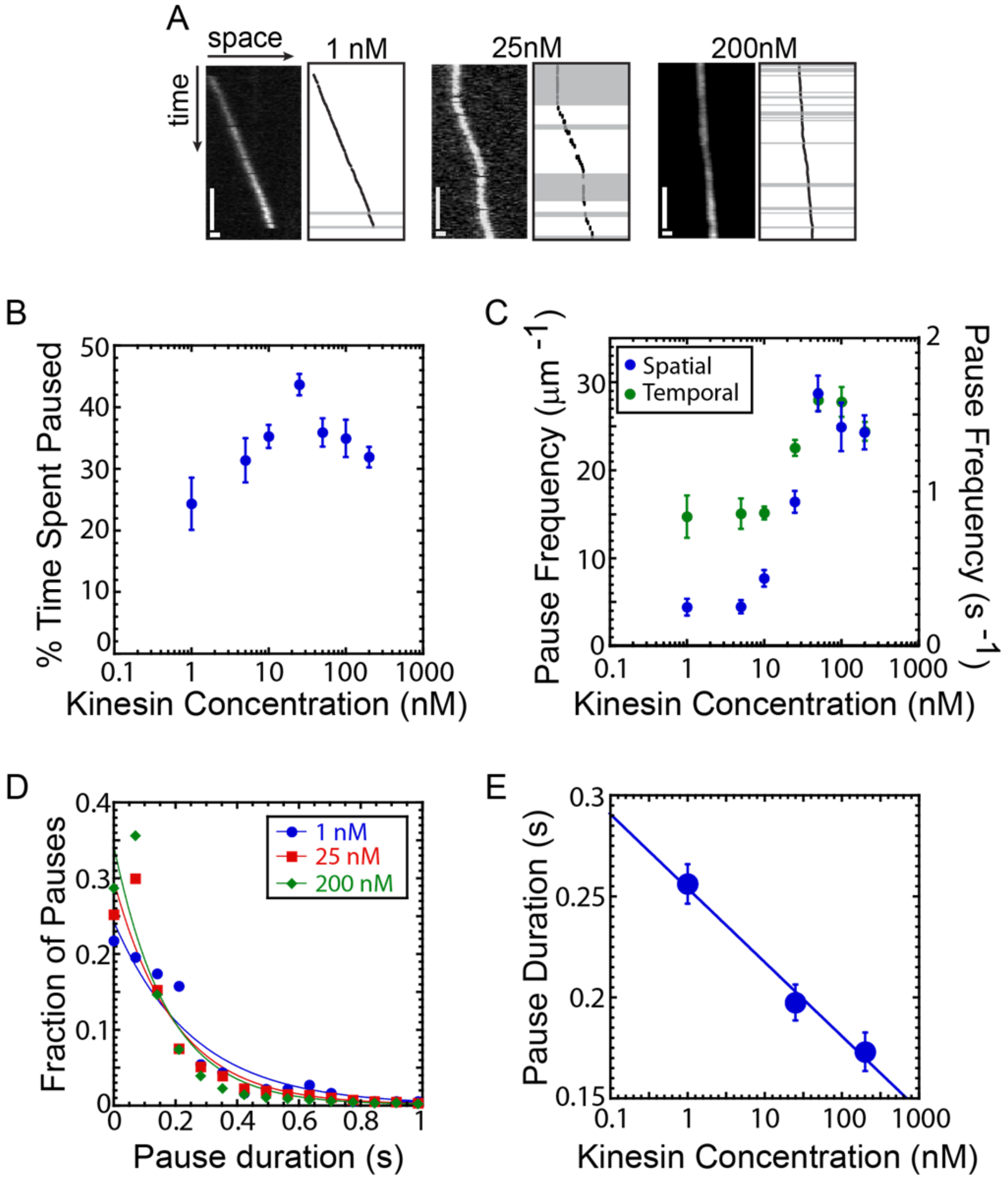

Figure 2.10 Pausing of Cargos on Crowded Microtubules

A. Representative kymographs showing segments of Qdot cargo runs on microtubules with 1 nM, 25 nM, and 200 nM kinesin. Left kymographs show raw data, right kymographs show kymographs generated by particle tracking code. Gray shading indicates pauses as determined by the program using the described threshold. Vertical scale bars are 2 seconds; horizontal scale bars are 0.5 μm. **B.** Percentage of time spent paused is measured as the percentage of time each individual cargo spent paused during its entire association time. For B and C: [1 nM (n = 19); 5 nM (n = 36); 10 nM (n = 138); 25 nM (n = 106); 50 nM (n = 49); 100 nM (n = 22); 200 nM (n = 36)]. Error bars represent standard error of the mean (SEM). **C.** Spatial and temporal pause frequency (blue and green circles, respectively) represent the average number of times a cargo pauses per micron or per second per run, respectively. **D.** Normalized distribution of cargo pause durations on microtubules with 1 nM (blue circles), 25 nM (red squares), and 200 nM (green diamonds) kinesin present. Each distribution was fit with an exponential decay shown as a line in the same color as the corresponding data. Decay constants representing characteristic pause durations for 1 nM, 25 nM, and 200 nM are 0.21 ± 0.03 s (R^2 = 0.92), 0.117 ± 0.007 (R^2 = 0.99), and 0.088 ± 0.004 (R^2 = 0.995), respectively. **E.** Decay constants from the exponential decay fits representing mean pause durations were plotted as a function of kinesin crowding. This data was found to decrease linearly with the log of kinesin concentration and was fit to the function: $y = m(\log(C)) + b$ and found m = -0.037 ± 0.004, b = 0.25 ± 0.006 (R^2 = 0.99).

To study pauses during cargo motility, I used the particle tracking program to set a specific threshold that allowed me to pull out pauses from motion of all cargos. I used a threshold of two standard deviations below the mean instantaneous velocity for each moving cargo to take into account the wide range of cargo velocities observed, which was dependent on levels of crowding. Pauses determined using this threshold are indicated in Figure 2.10A (right kymographs) by gray shading. I found that the percentage of time cargos spent paused during a run increased as crowding along the microtubule increased (Figure 2.10B). Additionally, I observed that the frequency of cargo pausing, both per second and per micron traveled, increased as crowding was increased (Figure 2.10C). To understand whether the duration of individual pauses was affected by the levels of crowding along the microtubule, I measured the duration of individual pauses by cargos for three representative concentrations: 1 nM, 25 nM, and 200 nM kinesin that correspond to low, medium, and high levels of crowding, respectively. For each concentration, the distribution of these pause durations was an exponential decay (Figure 2.10D). I fit each distribution to the exponential decay function:

$$y = A\exp\left(-{}^{t}\!/_{\tau}\right).$$

In a normalized distribution, the decay constant, τ, is equal to the mean. Therefore, τ, in this case represents the mean pause duration. I found that the mean pause duration became shorter as crowding on the microtubule increased (Figure 2.10E). To further demonstrate that these are three distinct distributions, I plotted the data as cumulative probability distributions (Figure 2.11) and fit the data with the cumulative probability function for an exponential decay: $y = 1 - \exp(-\beta x)$. Here, I show that these are three distinct distributions. From these results, I show that while cargos pause more frequently on crowded microtubules, the duration of these pauses actually become shorter with more motor traffic present on the microtubule.

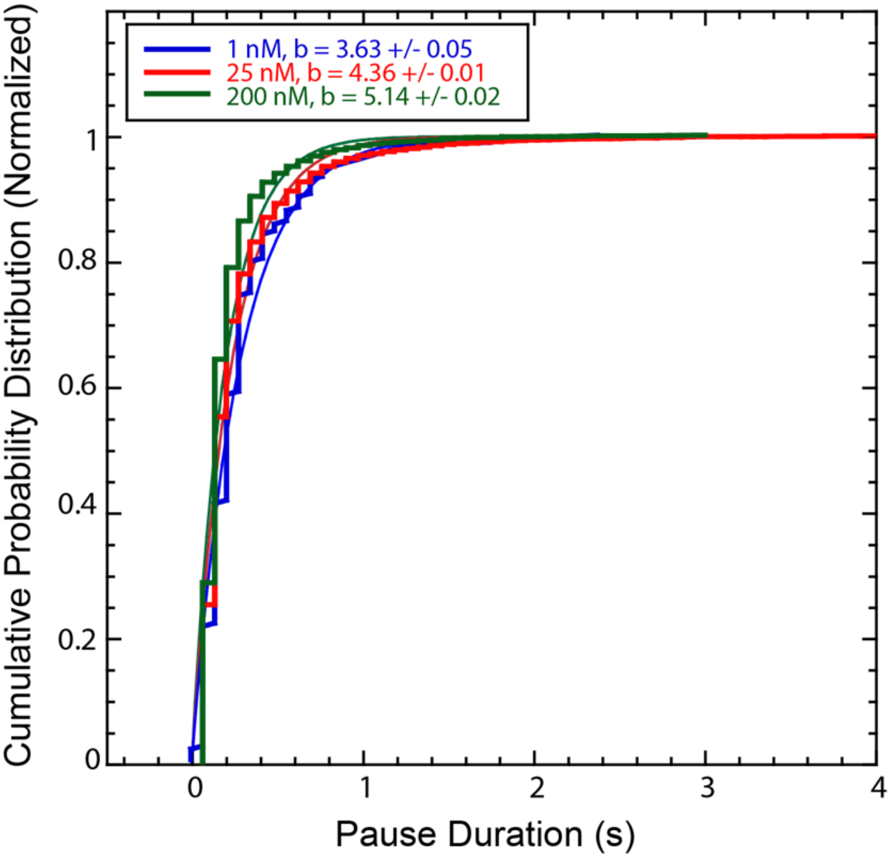

Figure 2.11 Cumulative Probability Distributions for Qdot Cargo Pause Durations

Qdot cargo pause duration data (solid thick lines) are fit to the cumulative probability function for an exponential decay (thin lines) with the equation: y = 1 – exp(-βx) for crowding kinesin concentrations of 1 nM (blue lines), 25 nM (red lines) and 200 nM (green lines). These three distributions were found to be distinct and fit best with values of β = 3.63 ± 0.005 (R^2 = 0.94), 4.36 ± 0.01 (R^2 = 0.90), and 5.14 ± 0.002 (R^2 = 0.84), respectively.

2.2.6 Qdot Cargos Reverse on Crowded Microtubules

I observed short reversals of cargos on crowded microtubules (Figure 2.12A). Because these reversals were short and difficult to distinguish by eye, I set a threshold using the particle tracking program to allow the program to identify reversals. To ensure that events pulled out as reversals were not artifacts of noise in the data, I set the threshold to 50 nm, meaning that a reversal event must be greater than 50 nm to be considered a reversal. This threshold is well above the resolution that exists for the time scale of the reversals (6 nm), ensuring that any reversals identified are not due to noise. Additionally, I measured reversals of stationary Qdots bound to the coverslip surface to estimate the noise floor. When I quantified the percentage of cargos that reversed at least once during their run, I observed a linear increase with the log of kinesin concentration (Figure 2.12B). The data measured was above the noise floor, which was calculated to be 5%.

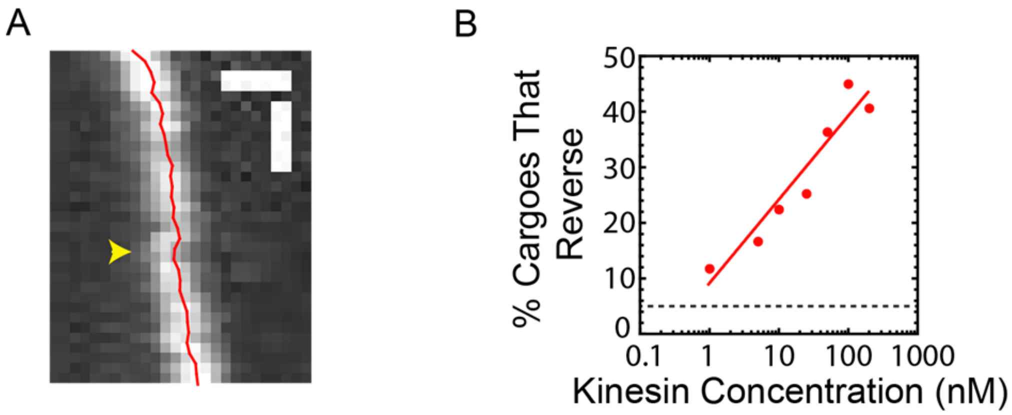

Figure 2.12 Cargo Reversals on Crowded Microtubules

A. Example kymograph showing cargo motility on crowded microtubules (50 nM kinesin). Kymograph shown is raw data, red trace shows kymograph generated by particle tracking program used to analyze data. Yellow arrowhead indicates short reversal in cargo motion in both raw data and data generated from particle tracking program. Vertical scale bar is 0.5 sec, horizontal scale bar is 0.5 μm. **B.** Percentage of cargos that reverse at least once during a run is plotted against the total concentration of kinesin added to crowd microtubules. Dotted line indicates noise floor, as determined by measurement of percentage of stationary Qdots that reversed. Data was fit to a linear fit of the log of kinesin concentration: $y = m*\log(x) + b$, where $m = 8 \pm 3$ and $b = 15 \pm 2$.

2.3 Discussion

In my assays, I observed that Qdot cargos were able to form non-specific interactions with non-biotinylated motors (Figure 2.13A). How non-biotinylated motors non-specifically associate with Qdot cargos is unclear. The Qdot streptavidin conjugates used in this study are comprised of a semiconductor core and shell that is coated with a polymer to attach streptavidin molecules. Three potential mechanisms by which motors could bind non-specifically to Qdots are (1) motors could bind non-specifically to streptavidin molecules, but this would be limited to the small number of streptavidin molecules on the Qdots, (2) motors could bind non-specifically to exposed polymer, or (3) motors could get caught in the polymer coating if the brush is splayed because of the high radius of curvature of the Qdot (Figure 2.13B).

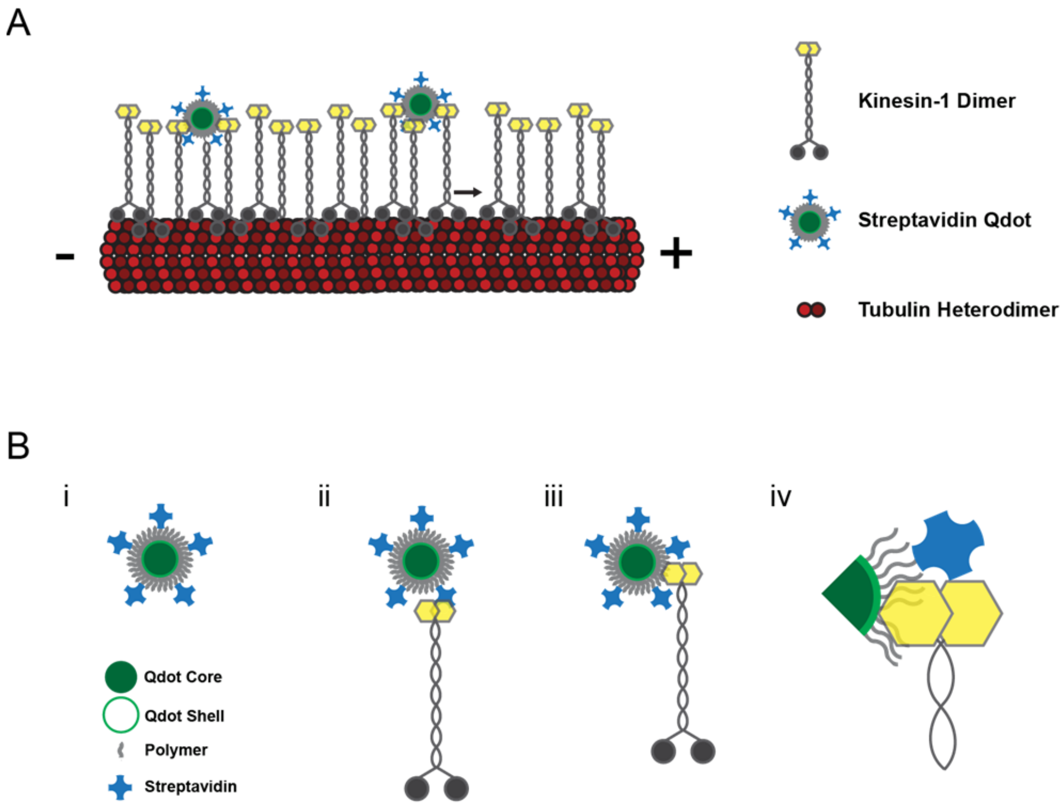

Figure 2.13 Non-Specific Interactions of Kinesin Motors with Quantum Dots

A. Representation of assay set-up with Qdot-kinesin added onto microtubules with high densities of excess motors. Arrow indicates the direction in which kinesin motors walk along the microtubule. Plus and minus signs denote the polarity of the microtubule filament. **B.** Potential mechanisms by which kinesin-1 could non-specifically associate with Qdots. **(i)** Representation of streptavidin conjugated Qdots used in this study. **(ii)** Kinesin-1 could bind Qdot via streptavidin molecule. **(iii)** Kinesin-1 could bind Qdot via polymer coating. **(iv)** Kinesin-1 could bind Qdot by getting lodged into splayed polymer coating.

Interestingly, bulk assays where only Qdots and non-biotinylated motors were mixed in solution did not show detectable binding events between Qdots and motors, suggesting that binding in solution, in the absence of microtubules, is rare. This is in contrast to my *in vitro* system, where binding events were observed frequently. This discrepancy can be explained when both the energy and local concentration of the species involved are considered.

Free in solution, kinesin motors and Qdots move purely by diffusion and have energies that are on the same order of magnitude, ~ 1 k_BT. Since I observe little binding between Qdots and non-biotinylated motors in solution, I conclude that such low energies are smaller than the energy barrier required for kinesin-Qdot binding. The result is that the probability that an interaction event between a kinesin motor and a Qdot would result in a non-specific binding event is low in free solution. However, in my assay, there are two parameters that lower the energy barrier required for Qdot-kinesin binding. First, in my assay, kinesin motors have a higher energy than in solution, as they generate force as they walk along microtubules. Kinesin motors produce a maximum of ~ 5 pN of force for every 8 nm step they take along the microtubule (Svoboda and Block, 1994; Svoboda et al., 1993). Thus, I can estimate that in my assay, kinesin motors can do maximal work on the order of ~ 10 k_BT. Given that I observed collisions between a non-biotinylated motor walking behind or in front of a Qdot to result in a high probability of binding, I conclude that the energy barrier for such binding is below 10 k_BT. The energy barrier of insertion of a particle into a polymer brush is on the order of 10 k_BT (Merlitz H, 2012), so the kinesin motor is likely to have enough energy to penetrate the brush. After intercalating into the brush, the motors might be kept there through van der Waals forces, but I was still able to observe motors dissociating from the Qdots, implying that the 10 k_BT of energy is also enough to escape the brush.

Another factor in my system that could lower the energy barrier required for Qdot-kinesin binding is the local concentration of each species. An increased concentration of either species will drive the binding reaction forward, resulting in the production of more Qdot-kinesin complexes. In my system, microtubules are attached to a glass surface and kinesin motors bind these microtubules with high affinity (K_d = 62 nM). This generates a high local concentration of motors and Qdots at the microtubule surface, favoring their interaction.

The ability of non-biotinylated motors to non-specifically bind Qdot cargos in my system allows for Qdot cargos to self-assemble and disassemble throughout transport. The transient nature of such cargos strongly resembles those thought to be used in slow axonal transport (Scott et al., 2011). Slow axonal transport is the predominant mechanism by which cytosolic proteins are transported along the axon (Tytell et al., 1981). This mechanism is distinct from that of fast axonal transport, which involves the transport of membranous cargos and membrane proteins. Fast axonal transport is understood relatively well; membrane proteins insert into membranous cargos which are transported by a fixed set of motors (Lorenz and Willard, 1978). The mechanism by which cytosolic proteins are transported is less clear. These proteins cannot insert into membranes, and thus must be transported through a mechanism different than that of membrane proteins. Studies have been carried out to characterize the motility of cytosolic proteins in axonal transport. These studies have revealed that the majority of cytosolic proteins are transported via slow axonal transport, and their transport is mostly carried out independent of membranous vesicles (Scott et al., 2011). While the basic transport properties of cytosolic proteins have been characterized, few studies have addressed the mechanism by which motors associate with these cargos to promote their transport. One recent study visualized the transport of fluorescently tagged cytosolic proteins in vivo and characterized the observed motility using computational modeling studies (Scott et al., 2011). With these studies, a mechanism was proposed that describes the transport of cytosolic proteins by a mechanism where motors transiently associate and dissociate with complexes of cytosolic proteins to promote their transport. This type of transport, driven by the transient association of motors, resembles that which occurs in my self-assembled Qdot system.

Interestingly, I observe several characteristics of transport in my system that resemble transport properties of slow axonal transport. First, the slow rate of Qdot cargo transport on crowded microtubules in my system is comparable to transport rates observed for cellular cargos in slow axonal transport. In cells, cargos transported by slow axonal transport have been shown to move at rates of 2-90 μm/sec (Brown, 2003). In my system, I observe that Qdot cargos move at rates of 35-120 nm/sec on microtubules crowded with 200-50 nM kinesin, respectively. Second, early reports on slow axonal transport describe short reversals in cargo motion (Wang et al., 2000), similar to the reversals observed in my system. Because these studies were carried out in cells where multiple motor types are present, the reversals observed here cannot be clearly differentiated between elastic recoil and retrograde motors. However, my system supports the idea that short reversals in anterograde cargo motion do not necessarily have to be a result of retrograde motors.

Compared to fast axonal transport, slow axonal transport is not well characterized. While recent studies have aimed to better characterize slow axonal transport, these studies have been restricted to in vivo studies and computational modeling. Here, I present a novel in vitro system that can be used to gain mechanistic insights into the transport process of slow axonal transport. The development of this in vitro system to study slow axonal transport can be used alongside current in vivo studies to provide a tool to systematically probe the transport properties of slow axonal transport.

In addition to acting as a system to study slow axonal transport, this system also allows for the study of kinesin motor motility on crowded microtubules. Here I studied how the motility of single kinesin motors compared to that of cargos transported on microtubules crowded with excess kinesin motors. The excess kinesin motors used in this study were motile motors, and can therefore be thought of as added traffic along the microtubule.

When velocities of single motors and cargos were measured on microtubules with different levels of crowding, I found that both single motor and cargo velocities were decreased as crowding along the microtubule was increased. This decrease in velocity could be due to motors waiting for the next available binding site along the microtubule to open up. Kinesin-1 has a specific binding site along the microtubule (Hirose et al., 1999; Uchimura et al., 2006). If this site is occupied by another motor, it will not be able to take its next step until the motor ahead moves. As microtubules become crowded with more motors, the probability that a motor’s next binding site will be occupied will increase, leading to an overall decrease in velocity. Such decreases in motor velocity on crowded microtubules were also observed in a recent study with kinesin-8 motors (Leduc et al., 2012).

While the effect of crowding on velocity was similar for both single motors and cargos, I observed drastic differences in processivity under these same conditions. I observed that single motor processivity was reduced in the presence of added traffic along the microtubule, while cargo processivity was enhanced. The reduction in processivity of single motors on crowded microtubules suggests that traffic poses as an obstacle for single motors. Numerous studies have shown that kinesin-1 will dissociate upon reaching static obstacles along the microtubule (Dixit et al., 2008; Ross et al., 2008; Telley et al., 2009; Vershinin et al., 2007), as these motors are unable to switch protofilament tracks (Ray et al., 1993). While the traffic in this study is a motile obstacle, I show that it moves very slow compared to single motor velocities. Thus, this traffic could act as a stationary obstacle on short timescales, causing single kinesin motors to dissociate prematurely from the microtubule. However, in the case of Qdot cargos, I showed that these cargos were able to associate new motors on crowded microtubules. While a single motor would dissociate upon reaching slow moving traffic, a cargo with multiple motors has additional motors that will keep the Qdot cargo tethered to the microtubule, allowing it to wait for the slow-moving obstacles to move. In addition to helping cargos navigate microtubules with obstacles, multiple motors on a cargo have been shown previously to increase processivity on uncrowded microtubules as well (Beeg et al., 2008; Block et al., 1990; Klumpp and Lipowsky, 2005; Korn et al., 2009; Kunwar et al., 2008; Muller et al., 2010; Vershinin et al., 2007). This is again attributed to having additional motors present to maintain cargo attachment to the microtubule if a single motor dissociates. Thus, on microtubules with high levels of traffic, multiple motors on a cargo help to increase processivity by increasing the inherent cargo run length as well as by helping cargos to navigate behind slow moving obstacles.

In experiments with 50 nM kinesin added to microtubules, I determined that there were 7 motors bound to Qdot cargos, and these cargos were able to travel approximately 4.5 μm before detaching. Previous studies of cargos carried by multiple motors show that cargos transported by 3 motors can transport cargos up to 4-6 μm (Korn et al., 2009; Kunwar et al., 2008). While I observed run lengths on a similar scale to what has been observed for cargos transported by only 3 motors, this can be explained by the fact that I have additional crowding in my experiments. I know from single motor data that traffic negatively affects kinesin processivity. While I observed increased run lengths on crowded microtubules with multiple motors, these run lengths are most likely shorter than what would be observed if these cargos were transported by the same number of motors on uncrowded microtubules. In addition, the 7 motors that were determined to be associated with Qdot cargos includes all motors associated with the Qdot, some of which may not be in contact with the microtubule.

During transport of Qdot cargos on crowded microtubules, I observed an increased frequency of pausing. These pauses are likely due to cargos encountering a slow-moving motor that is occupying the binding site needed for its next step. Interestingly, the mean pause duration actually decreased as traffic along the microtubule increased. While I would expect this mean pause duration to increase with increased traffic, as it would take longer for obstacles to move due to slower velocities, the decrease observed can be explained by the ability of Qdot cargos to associate more motors on these highly crowded microtubules. As Qdot cargos are transported along crowded microtubules, they are able to easily encounter and associate with motors along the protofilament on which they are traveling. As the levels of crowding increase along the microtubule, I believe that the probability of a Qdot associating with a motor on a neighboring protofilament increases. I speculate that a cargo associated with motors on multiple protofilaments would have the ability to switch protofilament tracks upon reaching an obstacle. This ability to circumvent obstacles would result in a decrease in pause duration compared to cargos that are unable to switch protofilaments and must wait for the obstacle to move.

Another effect of high levels of crowding on Qdot cargo motility were short reversals in cargo motion during transport. I believe that these reversals are a result of having multiple motors associated to a single cargo. If a motor bound to the front end of a cargo is traveling ahead of the other motors complexed to the cargo, the system will be under strain. If this front motor detaches from the microtubule, it would result in the system relaxing, which would be observed as the cargo rocking backwards to reposition itself over the remaining motors bound to the microtubule. These types of cargo reversals, or “bead flop” have been described previously using a microtubule gliding assay system, where it was shown that microtubules transported by 3 motors were observed to exhibit short jumps in both the forward and reverse direction during gliding (Leduc et al., 2007). In my experiments, I observed that cargo reversals increased linearly with the log of kinesin concentration added to microtubules. This is as expected as the probability of having multiple motors bound to a single cargo increases with increased crowding. In addition, the probability of having a front motor detach increases with increased crowding as well, as more obstacles in the form of traffic are introduced.

While I observed a linear increase in the percentage of cargos that reverse, it was linear with the log of the kinesin concentration. If the kinesin concentration were to be plotted on a linear scale, I would see that the data would gradually saturate, rather than continue to increase linearly. The fact that this percentage does not continue to increase linearly with increasing kinesin concentrations, but begins to saturate at higher kinesin concentrations could be due to the limited size of the Qdot cargo used in these assays. Because I suspect that the probability of a cargo reversal is related to the number of motors bound to the cargo, at higher kinesin concentrations, the Qdot surface exposed to the microtubule could become saturated with kinesin motors. Above a certain kinesin concentration, these Qdot cargos cannot add any additional motors, and the probability of a cargo reversal would be expected to no longer increase.

In these studies, I showed that cargos can reverse over short distances in the presence of a single motor type. While reversals observed in cargo transport are typically attributed to a switch in motor type (ie dynein taking over), it is interesting to note that some short reversals may actually be driven by kinesin motors alone.

From this study, I have shed light on the mechanisms by which cargos transported along crowded microtubules overcome motile obstacles to ensure efficient transport. I show that single motors alone are not able to navigate traffic efficiently. Cargos that are able to associate multiple motors move slow on microtubules with high levels of traffic, but are able to remain associated with the microtubule longer and I speculate that these cargos can circumvent obstacles by switching to a neighboring protofilament. These findings provide new insights into how cargos are efficiently transported on microtubules in cells, which are crowded with both motile and stationary obstacles.

2.4 Methods

2.4.1 Protein Purification. A human kinesin-1 construct truncated at amino acid 560 fused to either a C-terminal Halo Tag (Promega) or GFP tag and a 6X His Tag was expressed using a pET17b expression vector. Expression with IPTG and affinity purification with Nickel beads (Qiagen) were carried out as described previously (Pierce and Vale, 1998). HaloTag-kinesin and GFP-kinesin concentrations were quantified by comparison to known BSA standards on a Coomassie-stained SDS-PAGE gel.

2.4.2 Qdot-motor attachment. To label quantum dots (Qdots) with HaloTag kinesin, I used the HaloTag PEG-Biotin Linker (Promega) that covalently binds the HaloTag to generate a biotinylated kinesin. Qdot streptavidin conjugates, 525 nm emission (Invitrogen) were then bound to the kinesin. HaloTag kinesin, HaloTag PEG-Biotin Linker, and Qdot streptavidin conjugates were mixed in a 1:10:10 ratio, respectively, to ensure only one kinesin molecule per quantum dot. HaloTag kinesin and HaloTag PEG-

Biotin Linker were incubated together first for 10 minutes at room temperature. Qdot streptavidin conjugates were then added and incubated for an additional 10 minutes at room temperature. Complexes were then kept on ice.

2.4.3 Microtubule Preparation. Rhodamine labeled microtubules were prepared using a 1:13.5 ratio of labeled:unlabeled tubulin. Rhodamine labeled tubulin was purchased from Cytoskeleton, Inc. Unlabeled tubulin was purified from porcine brain as described previously (Peloquin et al., 2005). To prepare microtubules, both unlabeled and rhodamine labeled tubulin were brought to 5 mg/mL in PEM-100 (100 mM K-Pipes, pH 6.8, 2 mM $MgSO_4$, 2 mM EGTA) and incubated for 10 minutes on ice. Tubulin was centrifuged at 4°C for 10 minutes at 366,000 xg to remove tubulin aggregates. The remaining tubulin in the supernatant was mixed with 1 mM GTP and polymerized at 37°C for 20 minutes. 50 μM Taxol was added to stabilize polymerized microtubules, followed by another 20 minute incubation at 37°C. Polymerized microtubules were centrifuged at 25°C for 10 minutes at 14,000 x g to separate unincorporated tubulin. The microtubule pellet was resuspended in 50 μL PEM-100 with 40 μM Taxol.

2.4.4 In Vitro Assays. Assays were carried out in 10 μL flow chambers made of a glass slide attached to a cover slip with double-stick tape. Prior to use, cover slips were biologically cleaned and treated with dimethyldichlorosilane solution, 2% w/v (GE Healthcare). Flow chambers were first incubated with 2% anti-tubulin antibody in PEM-100 for 5 minutes to attach microtubules, followed by a 5 minute incubation with 5% Pluronic F-127 (Sigma) in PEM-100 to block the surface. Rhodamine-labeled microtubules (0.05 mg/mL microtubules, 20 μM Taxol in PEM-100) were allowed to bind for 10 minutes. Excess microtubules were removed with a wash step (10 mM DTT, 20 μM Taxol in PEM-100). To ensure a subset of Qdots with kinesin would reach the microtubule in crowded conditions, Qdots were bound to the microtubule in a rigor state for 10 minutes (10 nM quantum dot labeled kinesin, 100 mM DTT in PEM-100). For assays in which the final kinesin concentration was 1 nM and 5 nM kinesin, 1 nM and 5 nM Qdots with kinesin were bound during this step, respectively. Finally, motility mix was added to the chamber (same concentration of Qdots with kinesin as in previous step plus unlabeled HaloTag kinesin to achieve the correct final concentration of kinesin, 0.05% Pluronic F-127, 25 μM Taxol, 0.25 mg/mL BSA, 50 mM DTT, 0.5 mM ATP, 15 mg/mL glucose, 0.5 mg/mL glucose oxidase, 0.15 mg/mL catalase in PEM-100)

2.4.5 Two-Color Assays. Assays were set up similar to the *in vitro* assays described earlier. In the two-color assays, HaloTag PEG-Biotin Linker was not present. Following the wash step to remove excess microtubules, motility mix was added that contained Qdot streptavidin conjugates, 655 nm emission (Invitrogen) and a final concentration of 50 nM kinesin (100 nM 655 nm Qdots, 45 nM unlabeled HaloTag kinesin, 5 nM GFP kinesin, 0.05% Pluronic F-127, 25 μM Taxol, 0.25 mg/mL BSA, 50 mM DTT, 0.5 mM ATP, 15 mg/mL glucose, 0.5 mg/mL glucose oxidase, 0.15 mg/mL catalase in PEM-100).

Qdot and GFP kinesin motility were observed using Total Internal Reflection Fluorescence (TIRF) microscopy. Both Qdots and GFP kinesin were illuminated using a 50 mW 488 Cyan laser (Spectra-Physics). Images were taken over a period of two minutes, and were recorded in both channels. GFP kinesin was imaged using a 500 ms exposure and 655 nm Qdots were imaged using a 200 ms exposure. Qdots were imaged every three frames.

Kymographs of GFP kinesin associated with Qdots were generated. Line scans through the first pixel of these GFP kinesin runs were used to determine the intensity of GFP associated with Qdots. The same was done for a single GFP kinesin motor traveling on the same microtubule, which was not associated with a Qdot. Intensity plots were fit to a gaussian to determine the intensity of GFP present. The intensity found for GFP which was associated with a Qdot was divided by the intensity of a single GFP kinesin motor on the same microtubule to determine the number of GFP kinesin motors associated with each Qdot.

2.4.6 Imaging. An image of the microtubules was acquired using epi-fluorescence prior to imaging Qdots. Ten minute recordings of the Qdot motility were taken with a 70 ms exposure time using Total Internal Reflection Fluorescence (TIRF) microscopy with a 50 mW 488 Cyan laser (Spectra-Physics) illumination built around an inverted Nikon Ti-E microscope (Nikon). The microscope uses a 60x 1.49 NA objective and images were collected using an electron multiplier CCD camera (Cascade II, Roper Scientifics) after a 4x beam expander. The final pixel size was 67.5 nm. Images were acquired with no delay and saved as nd2 files and exported as 16-bit tif files.

2.4.7 Data Analysis. Image sequences were imported and analyzed using custom MatLab programs modified from those used previously (Gao and Kilfoil, 2009). The program finds and tracks particles in sequences of Qdot images, finds microtubule tracks in the epi-fluorescence image, and correlates the Qdot motion with the microtubule to break out motion along the microtubule. It also analyzes run data for pauses and backward motion. I tested the resolution limits of the optical system and data analysis software using a fixed Qdot. The fixed Qdot was tracked for 100 – 1000 frames and the standard deviation was determined from the localizations. For small numbers of frames, the resolution was 6 nm, as previously reported for similar experimental systems (Ali et al., 2008). For longer movies, there was an uncorrectable drift that resulted in a larger resolution of 20 nm. This is still an order of magnitude higher resolution than the standard optical resolution of the microscope, calculated to be about 200 nm for the wavelengths I use and the 1.49 NA objective used.

Every frame in the image stack is first analyzed with a localization algorithm to extract the position of individual quantum dot cargos. This localization algorithm finds the centroid by fitting a 2D Gaussian to each Qdot cargo. The best-fit localization determined by a least squares fitting is taken to be the Qdot cargo position. The original image of the microtubule is then skeletonized, resulting in a list of pixel values that can be fit dynamically with an Nth order polynomial curve. This curve represents the position of the microtubule in space and is used as a reference to project the path of the Qdot cargo (which is culled from the results of the localization routine) along the microtubule. The displacement vector of the Qdot cargo at each time step is transformed into the basis defined by the normal and tangential unit vectors along the microtubule. This projection allows for more accurate calculations of its working velocity. Reverse motion is determined by negative tangential velocities. To ensure noise in the data was not mistaken as a reversal event, a threshold was set to allow only backwards motions occurring over a distance greater than 0.05 μm to count as a reversal event. Data was further analyzed for pause events by using a threshold on the velocity; velocity lower than two standard deviations below the mean instantaneous velocity is considered to be paused. By filtering out such pauses, I can accurately calculate the moving velocity of the Qdot cargos, as well as investigate pausing behavior. Data was affected by boxcar averaging, as expected, so no averaging was used.

2.4.8 Estimate of the Kinesin binding constant from images. I estimated the binding affinity by taking images of GFP-kinesin binding to microtubules with increasing concentrations of added kinesin. Using the lowest concentration, I estimated the intensity of a single GFP-kinesin. I recorded all images with the same exposure, camera, and laser settings so that the intensity of a single GFP-kinesin was consistent for each. The intensity along the length of microtubules coated with GFP-kinesin was measured using ImageJ. The background intensity was subtracted from each image using line scans that extended perpendicular through the microtubule. The intensity of the corrected intensity along the microtubule was divided by the intensity of a single GFP-kinesin to calculate the number of GFP-kinesins along the microtubule. This number of GFP-kinesins along the microtubule was divided by the length of the microtubule to find the number of kinesins per unit length. The ratio of bound GFP-kinesins to the number of tubulin dimers was determined by dividing the number of GFP-kinesins per unit length by 1625 dimers, since that is the number of dimers in 1 μm of a 13-protofilament microtubule. The background intensity from GFP-kinesin images was used to determine the concentration of free kinesin not bound to microtubules.

The ratio of bound kinesins to the tubulin dimers was plotted as a function of free kinesin concentration in the background, and it was found that the relationship was still linear. The linear behavior can be understood starting from the known dependence for binding:

$$ratio = S\frac{[kinesin_{free}]}{K_D + [kinesin_{free}]}.$$

In the dilute regime, $[\mathrm{kinesin}_{\mathrm{free}}] << K_D$, and the denominator approaches K_D. In this limit, the ratio is a linear function of the free kinesin concentration:

$$ratio = \frac{S}{K_D}[kinesin_{free}]$$

Since the known stoichiometry of kinesin binding is 1 kinesin motor head to 1 dimer, the slope of the linear fit is inversely proportional to the binding affinity, K_D. Fitting my data to a linear equation, the best slope is given by 0.0161 ± 0.0009 nM^{-1}. The goodness of fit is $R^2 = 0.97$. Inverting this slope gives an effective affinity of 62 nM.

2.4.9 Estimate of the Qdot binding constant to kinesin using bulk assay.

Biotinylated 1 μm polystyrene beads (Spherotech) were washed 5 times in PEM-100.

Washed beads were mixed with 250 nM streptavidin Qdots and incubated for 1 hour at room temperature. Beads were centrifuged 2 minutes at 14,000 xg to remove unbound Qdots. Beads were then resuspended in 200 μL κ-casein and incubated for 1 hour at room temperature. Beads were then centrifuged to remove excess κ-casein. Increasing concentrations of non-biotinylated HaloTag kinesin (25 nM to 1 μM) were added to beads-Qdots and incubated for 1 hour at room temperature. Control samples without Qdots were used to determine the amount of kinesin present in the dead-volume between the large polystyrene beads. Beads were pelleted at 14,000 xg and the supernatant was separated. UV light was used to verify that Qdots had pelleted with biotinylated beads (Figure 2.4A). Supernatant and pellet samples were run on an SDS-PAGE gel. Kinesin-1 was detected using coomassie staining and western blotting using an anti-kinesin heavy chain antibody (Millipore, MAB1614).

2.4.10 Estimate of the Qdot binding constant to kinesin using visual assay. I created chambers with microtubules adhered to the surface, as usual in my assays. I added 50 nM kinesin without biotin and increasing concentrations of Qdots: (5 nM to 200 nM). I allowed the kinesin and Qdots to bind to the microtubules as usual. I quantified the number of Qdots binding to microtubules in three regions of the chamber by taking a single still frame of each region. I divided by the length of the microtubule and averaged the number of Qdots per μm. The ratio of bound Qdots to the number of kinesin motors per unit length was calculated and plotted as a function of the added number of Qdots. Since so few Qdots bound to the microtubules, the free concentration of Qdots is likely equivalent to the concentration of added Qdots. The data showed a linear dependence, and was fit to a line equation with a single fit parameter. As above for kinesin, the slope is equivalent to the stoichiometry divided by the equilibrium dissociation constant. The stoichiometry is unknown, but assuming it is one gives a lower bound on the value of K_D.

The data was best fit with a slope of 7.6 ± 1.6 x 10^{-7} nM^{-1}, which corresponds to a K_D value of 1.3 mM.

CHAPTER 3

KINESIN MOTILITY ON MICROTUBULE BUNDLES

I would like to acknowledge Joshua Pringle and Amanda Tan, who purified the MAP65 used to make antiparallel microtubule bundles in this study. Additionally, I would like to thank Professor Patricia Wadsworth and Sai Balchand for their help with getting started with the CAD cell culture.

3.1 Introduction

In addition to obstacles and traffic along the microtubule, motors also face a complex architecture of cytoskeletal tracks when traveling in the cell. Rather than existing as single filaments, microtubules often exist within a bundle. There is an abundant number of microtubule-associated proteins (MAPs) in the cell that function to crosslink microtubules, resulting in the formation of these microtubule bundles. The spacing between microtubules within these bundles is determined by the size of the crosslinking MAP (Chen et al., 1992).

Due to the inherent structural polarity of microtubules, there are three different types of microtubule bundles that can form: 1) parallel bundles where all microtubule plus ends point in the same direction, 2) antiparallel bundles where microtubules alternate polarity, with microtubule plus ends adjacent to a microtubule minus end, and 3) randomly oriented microtubules where there is no specific orientation of microtubules within the bundle.

MAPs are essential for the proper organization and maintenance of the microtubule cytoskeleton (Hirokawa, 1994). Depending on the region of the cell and the stage of the cell cycle, different microtubule organizations are required. For example, parallel microtubules are found in the axon of neurons (Heidemann et al., 1981). This enables the polarized transport of new material into the axon by anterograde transport and the recycling of material back to the cell body by retrograde transport (Holzbaur, 2004). Antiparallel bundles are found in the spindle midzone during mitosis and facilitate the separation of genetic material during cell division (Loiodice et al., 2005). Randomly oriented microtubule bundles are known to exist in dendrites (Baas et al., 1988). These bundle types are initiated and maintained by specific, and often multiple, MAPs.

To date, in vitro studies aimed at understanding kinesin motility have mostly examined kinesin motors on single microtubules. How kinesin motors navigate bundled microtubules, a microtubule architecture that is prominent throughout the cell, is unknown. Here I study kinesin motility on three different types of microtubule bundles: 1) tightly packed, randomly oriented microtubule bundles formed by depletion forces (Figure 3.1A), 2) spaced, antiparallel microtubule bundles formed by MAP65 (Figure 3.1B), and 3) parallel microtubule bundles formed from neuronal processes (Figure 3.1C). I show that MAPs could help to organize microtubule bundles to promote kinesin motility in comparison to motility on tightly packed bundles. Interestingly, I also show that single kinesin motors often switch microtubule tracks within PEG and MAP65 bundles. This switching is observed as reversals in the direction of motility on bundles that contain antiparallel microtubules. Such reversals in direction are not observed on parallel microtubule bundles, indicating that they are likely due to kinesin switching to an oppositely oriented microtubule.

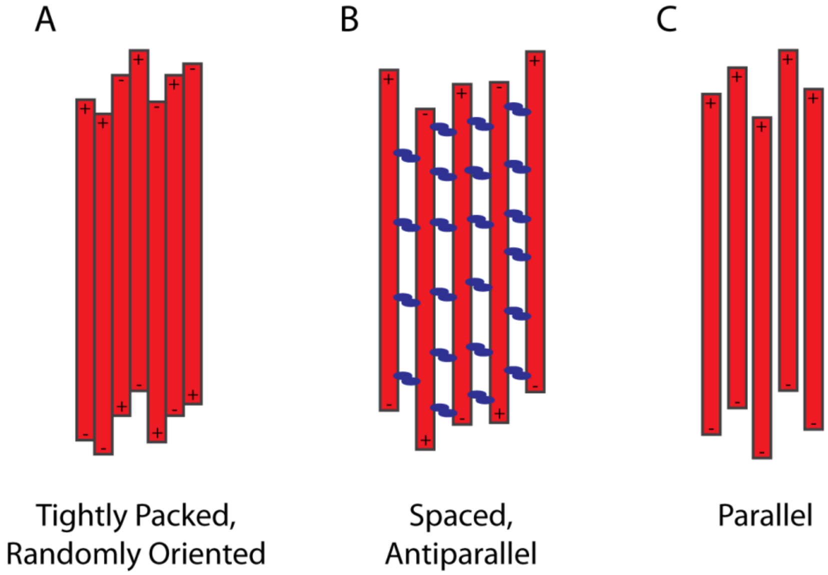

Figure 3.1 Microtubule Bundle Types

Kinesin motility will be studied on three types of microtubule bundles. **A.** Tightly packed bundles will be formed in the presence of PEG, creating microtubule bundles with randomly oriented microtubules. **B.** Bundles with antiparallel microtubules will be formed by the presence of MAP65, creating microtubule bundles with a 25 nm spacing between filaments. **C.** Microtubule bundles formed in neuronal-like processes of differentiated CAD cells will be comprised of parallel microtubules.

3.2 Results

3.2.1 Kinesin Motility on Single Microtubules in the Presence of PEG

To study tightly packed, randomly oriented microtubule bundles, I used polyethylene glycol (PEG) mw 40,000 to generate depletion forces to bundle microtubules (Needleman et al., 2005). Depletion forces arise when large structures (in this case, microtubules) are present in solution with small particles (in this case, PEG). When two microtubules come in close enough proximity such that the PEG polymer can no longer fit in between, the PEG is excluded to the outside of the microtubules, creating an osmotic pressure that pushes the two microtubules together. Thus, when microtubules were mixed in solution with PEG, I was able to form tightly packed bundles of microtubules (Figure 3.4A). These bundles formed with microtubules in random orientations and consisted of a combination of parallel and antiparallel oriented microtubules (Needleman et al., 2005).

Before looking at the motility of kinesin molecules on these bundles, I first characterized the effect of PEG alone on kinesin binding and motility. I compared kinesin binding and motility on single microtubules in the presence of 0% or 5% PEG (mw 40,000). I first noticed a striking difference in the amount of kinesin bound to microtubules in the presence of PEG (Figure 3.2A). I measured the mean intensity of GFP-kinesin fluorescence along microtubules and observed an approximately 8-fold increase in kinesin binding on microtubules with 5% PEG (Figure 3.2B). This observed increase in the mean fluorescence intensity along microtubules in the presence of PEG could be due to 1) more individual motors bound along the microtubule or 2) the ability of PEG to cause multiple motors to associate together. To determine whether PEG causes multiple motor associations, I compared the fluorescence intensity of individual puncta on single microtubules in the absence and presence of PEG. A higher intensity of puncta in the presence of PEG would imply that there are multiple motors in each puncta, and that PEG induces the formation of multiple-motor aggregates. I found that individual puncta on single microtubules in the absence and presence of PEG had similar fluorescence intensities (Figure 3.2C), indicating that PEG does not induce the formation of multiple-motor associations. Thus, puncta along microtubules in the presence of PEG correspond to single motors, and the increase in fluorescence observed along these microtubules is due to the association of more individual motors along the length of the microtubule. This increase in binding of kinesin motors to microtubules in the presence of PEG suggests that PEG increases the affinity of kinesin motors to microtubules. For further single molecule studies of kinesin in the presence of PEG, I used a 6-fold dilution of kinesin motors compared to what is used on microtubules in the absence of PEG in order to better observe single motors.

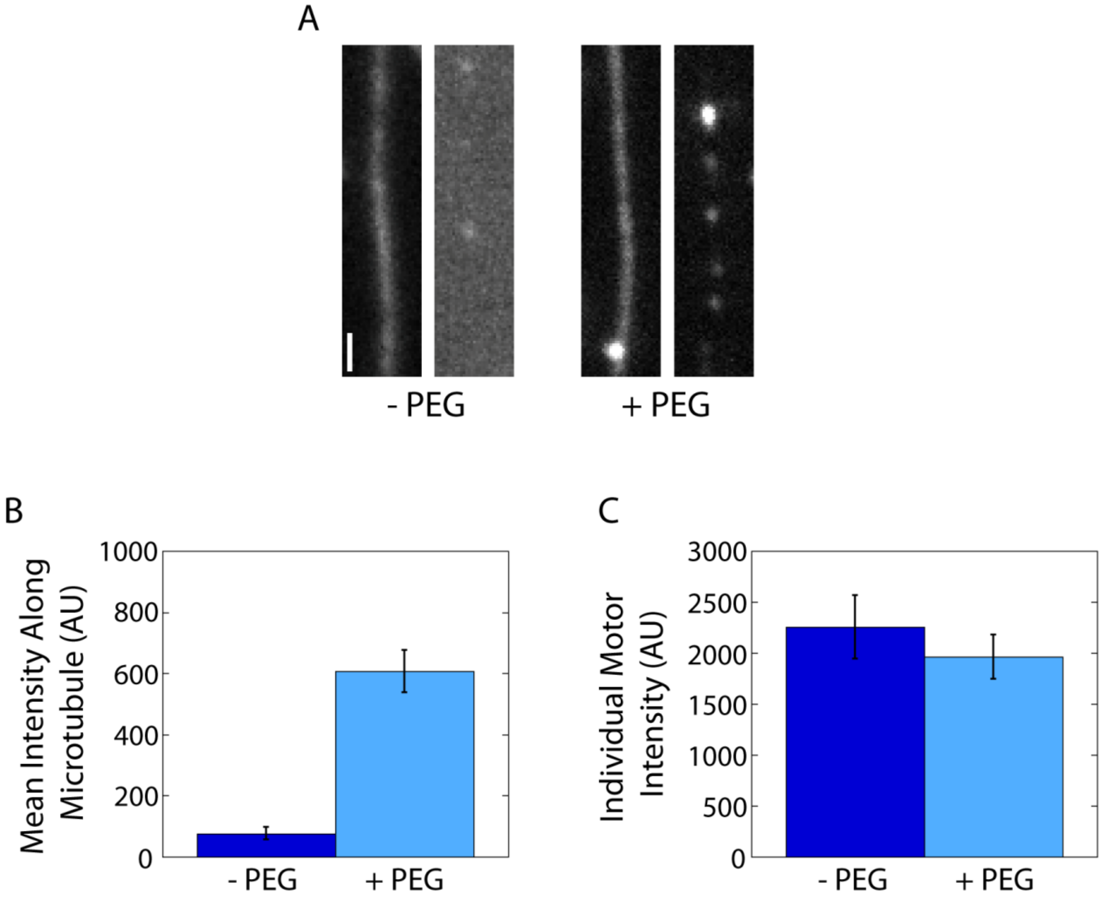

Figure 3.2 Effect of PEG on Kinesin Binding to Microtubules

A. Representative images show kinesin binding in the presence and absence of PEG when identical concentrations of kinesin motors are added. Left image shows microtubule and right image shows kinesin molecules bound to the microtubule. Scale bar is 1 μm. **B.** Mean intensity along microtubules in the GFP channel was measured to estimate the amount of kinesin motors bound to microtubules in the absence and presence of PEG. For each condition, 50 microtubules were measured. Error bars represent the standard error of the mean. **C.** Intensity of individual kinesin motors on single microtubules in the absence and presence of PEG. For motors in the absence of PEG, N = 61; for motors in the presence of PEG, N = 90. Error bars represent the standard error of the mean.

In addition to differences observed in kinesin binding in the presence of PEG, I also observed differences in the motility properties of kinesin motors (Figure 3.3A). I observed that the run length of kinesin was enhanced in the presence of PEG (Figure 3.3B). In the presence of 0% PEG, motors traveled an average of 1.2 μm before detaching, whereas in the presence of 5% PEG, motors traveled an average of 2.8 μm. For distributions of measurements, see Appendix A, Figures A.1A and A.2A. Likewise, I observed that the association time, or the total time a motor remained bound to the microtubule before dissociating, increased from 4.1 sec in the absence of PEG to 11.7 sec in the presence of 5% PEG (Figures 3.3C, A.1B, A.2B). I did not observe any effect of PEG on the velocity of motors. For all velocity measurements in this study, I calculated the moving velocity of motors. This measurement takes into account only the moving portions of a run, omitting any visible pauses from the measurement. I observed that motors moved at approximately 0.35 μm/sec both in the absence and presence of PEG (Figures 3.3D, A.1C, A.2C). Interestingly, I also observed that the percentage of motors that paused during a run was higher in the presence of PEG (Figure 3.3E).

From these studies, I show that PEG increases the interaction of kinesin motors with microtubules. This polymer enables motors to travel farther distances before dissociating from the microtubule and also causes increased pausing of motors during motility.

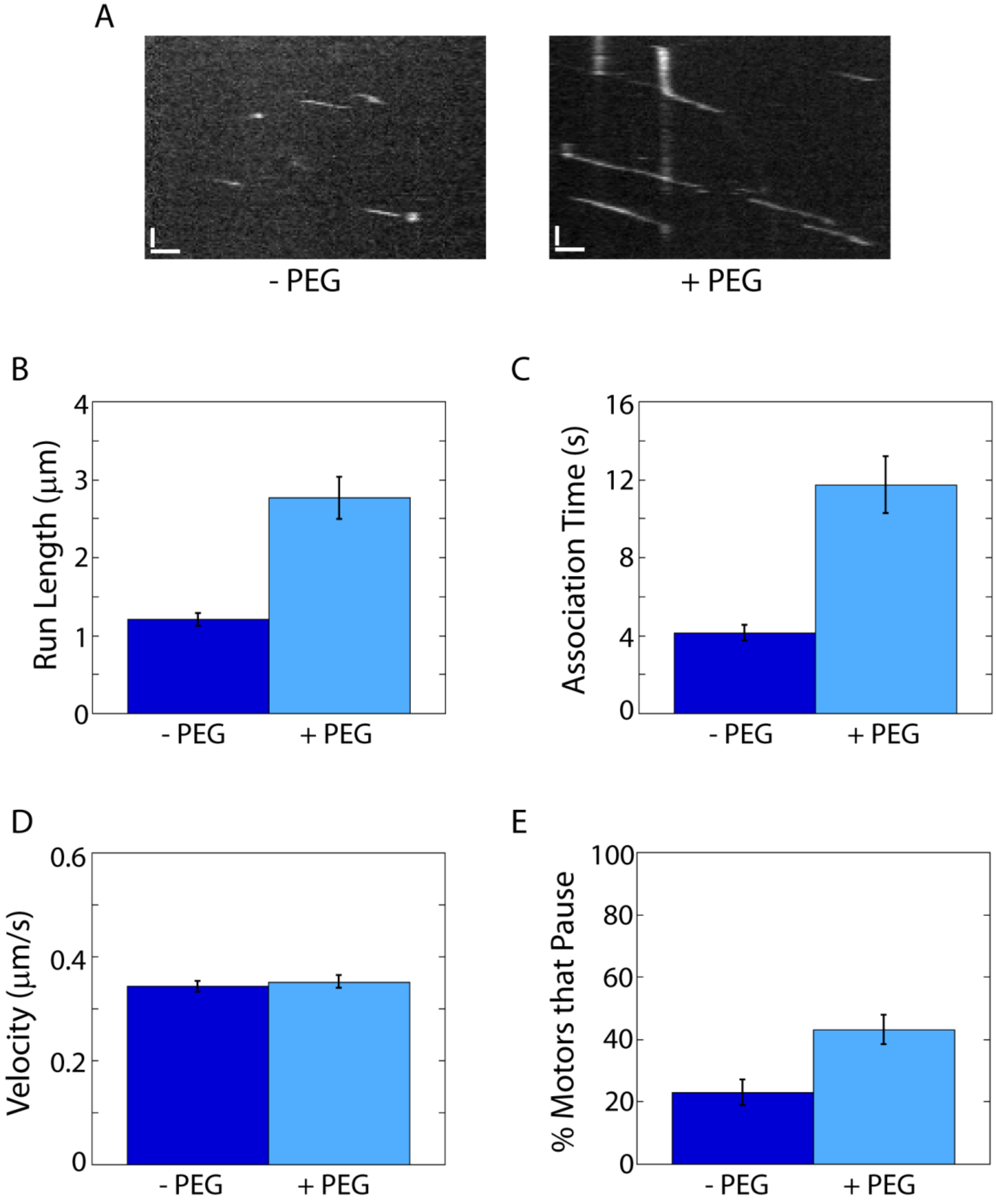

Figure 3.3 Kinesin Motility on Single Microtubules in the Presence of PEG

A. Representative kymographs showing kinesin motility on microtubules in the absence and presence of PEG. Vertical scale bars are 5 seconds. Horizontal scale bars are 1 μm. **B.** Run length measured as the total distance traveled by motors in the absence and presence of PEG. Error bars represent the standard error of the mean. **C.** Association time measured as the total time motors remained bound to the microtubule in the absence and presence of PEG. Error bars represent the standard error of the mean. **D.** Moving velocity of motors on microtubules in the absence and presence of PEG. Error bars represent the standard error of the mean. **E.** Percentage of motors that pause at least once during a run in the absence and presence of PEG. Error bars represent the standard error of proportion. **B-E.** For data taken in the absence of PEG, N = 105. For data taken in the presence of PEG, N = 109.

3.2.2 Kinesin Motility on PEG Bundles

I next studied kinesin motility on microtubule bundles formed in the presence of PEG (Figure 3.4A). By comparing the fluorescence intensity of a bundle of labeled microtubules to the fluorescence intensity of single labeled microtubules that were imaged in the absence of PEG, I determined that there are, on average, 7 microtubules per bundle when formed in the presence of 5% PEG.

On PEG bundles, I observed two types of kinesin motility: 1) kinesin motors walked in a single direction along the microtubule bundle (Figure 3.4B, middle kymograph) and 2) kinesin motors were able to reverse direction while walking along the microtubule bundle, presumably by switching to a neighboring microtubule oriented in the opposite direction (Figure 3.4B, left kymograph).

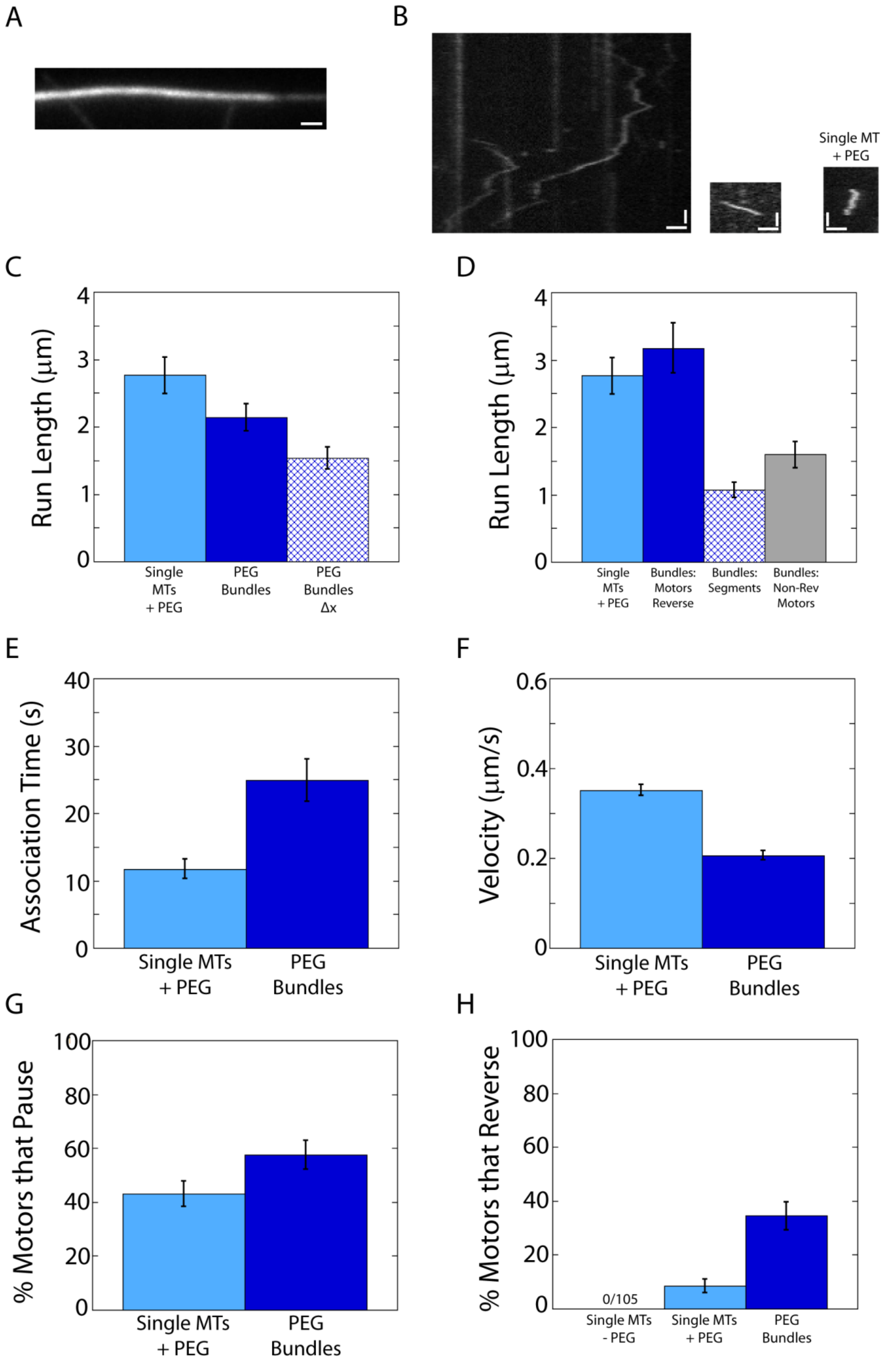
A
B
Single MT
+ PEG
C
Run Length (µm)
0
1
2
3
4
Single MTs + PEG
PEG Bundles
PEG Bundles Δx
D
Run Length (µm)
0
1
2
3
4
Single MTs + PEG
Bundles: Motors Reverse
Bundles: Segments
Bundles: Non-Rev Motors
E
Association Time (s)
0
10
20
30
40
Single MTs + PEG
PEG Bundles
F
Velocity (µm/s)
0
0.2
0.4
0.6
Single MTs + PEG
PEG Bundles
G
% Motors that Pause
0
20
40
60
80
100
Single MTs + PEG
PEG Bundles
H
% Motors that Reverse
0
20
40
60
80
100
0/105
Single MTs - PEG
Single MTs + PEG
PEG Bundles

Figure 3.4 Kinesin Motility on PEG Bundles

A. Image of a microtubule bundle formed in the presence of 5% PEG. Image was acquired using a 500 ms exposure time. Scale bar is 1 μm. **B.** Left kymograph shows examples of kinesin runs on PEG bundles with clear reversals in motor direction. Middle kymograph shows examples of kinesin runs on PEG bundles with no reversals in motor direction. Right kymograph depicts a reversal event observed on single microtubules in the presence of PEG. Vertical scale bars are 5 seconds. Horizontal scale bars are 1 μm. **C.** Run length was measured as the total distance traveled on single MTs + PEG and PEG Bundles; and as the final distance traveled (Δx) for motors on PEG bundles. Error bars represent the standard error of the mean. **D.** Run lengths of motors that reverse direction on PEG bundles were compared to those of motors that do not reverse direction on PEG bundles. In addition, the average distance traveled before or after reversing direction on PEG bundles was measured (segments). Error bars represent the standard error of the mean. **E.** Association time was measured as the total time motors remained bound to single microtubules with PEG and PEG bundles. Error bars represent the standard error of the mean. **F.** Moving velocity of motors on single microtubules with PEG and PEG bundles. Error bars represent the standard error of the mean. **G.** Percentage of motors that pause at least once during a run on single microtubules with PEG and PEG bundles. Error bars represent the standard error of proportion. **H.** Percentage of motors that reverse directions at least once during a run on single microtubules without PEG, single microtubules with PEG, and PEG bundles. Error bars represent the standard error of proportion. **C-H.** For single microtubules with PEG, N = 109; for PEG bundles, N = 87; for motors that reverse on PEG bundles, N = 30; for motors that do not reverse on PEG bundles, N = 57.

I compared the motility properties of kinesin motors walking on single microtubules in the presence of PEG to those of kinesin motors walking on PEG bundles. To compare the run length of motors on single microtubules versus microtubule bundles, I first measured the total run length, or total distance traveled, of all motors (Figures 3.4C, A.3A, A.4A). For motors that move in a single direction, this was the total distance traveled between when the motor landed on the microtubule and when the motor dissociated from the microtubule; for motors that reverse directions during a run, this was the absolute sum of all forward and reverse segments of the run. I found that there was no statistically significant difference in the average total run length of motors on PEG bundles compared to motors on single microtubules in the presence of PEG ($p > 0.05$). I also measured the run length as the final distance traveled, or Δx, for motors on PEG bundles. For motors that move in a single direction, this would be the same distance as calculated previously; for motors that reverse directions, this was calculated as the distance between where the motor landed on the microtubule and where the motor finally dissociated from the microtubule (Figure 3.4C).

Next, I looked at run lengths of motors that reverse directions on PEG bundles separately from those motors that travel only in one direction. I observed that motors that reverse directions have longer total run lengths (absolute sum of all segments) compared to motors that do not reverse directions during a run. I found that the total run length of motors that reverse direction was comparable to that of motors on single microtubules in the presence of PEG (Figures 3.4D, A.3B, A.4B). However, of motors that reverse direction on PEG bundles, the average distance traveled before or after a reverse in direction (individual segments of a run) was much shorter, and more comparable to the run lengths of motors traveling on PEG bundles that do not reverse direction (Figure 3.4D).

The total association time was measured as the total time a motor remained bound to the microtubule for motors on PEG bundles and for motors on single microtubules in the presence of PEG. I found that the total association time of motors on PEG bundles was longer than that of motors on single microtubules in the presence of PEG (Figures 3.4E, A.3C, A.4C). On single microtubules in the presence of PEG, motors remained bound for an average of 11.7 sec, whereas on PEG bundles, motors remained bound for an average of 24.9 sec. I also observed that motors traveling on PEG bundles moved slower compared to motors on single microtubules in the presence of PEG. Motor velocity dropped from 0.35 μm/sec on single microtubules with PEG to 0.21 μm/sec on PEG bundles (Figures 3.4F, A.3D, A.4D). The velocity of motors that reverse direction on PEG bundles was calculated by averaging the velocities of individual segments of these runs. When the percentage of motors that pause during a run on single microtubules with PEG was compared to that on PEG bundles, I observed that more motors paused while traveling on PEG bundles (Figure 3.4G).

As stated previously, I observed kinesin motors to reverse directions while walking on PEG bundles. I quantified the percentage of motors that reverse during a run and found that 34% of motors walking on PEG bundles reversed direction (Figure 3.4H). I did observe a small percentage of motors, 8%, that reversed direction on single microtubules in the presence of PEG (Figures 3.4B and 3.4H). I believe this small number could be due to the presence of a second, nearby microtubule that did not create an obvious increase in fluorescence to indicate an overlapping microtubule; or rather a second microtubule landed during imaging and was not present when the initial microtubule image was captured. Another possible explanation is that PEG increases the diffusive state of kinesin, creating motility that appears like reversals. This could occur if kinesin lands on the microtubule in an orientation such that the microtubule binding domain is not oriented close to the microtubule. Positive residues in other regions of the motor could induce diffusion of the motor through these charged regions. In my typical assays, I would expect the motor to diffuse away from the microtubule if it did not form interactions with its microtubule binding domain. However, the presence of PEG in these experiments could keep the motor in close proximity through depletion forces, allowing it to diffuse along the microtubule instead of away from the filament. It should be noted that I did not see any reversals in direction when looking at kinesin motility on single microtubules in the absence of PEG (Figure 3.4H).

Here I show that kinesin motility is reduced on the tightly packed, randomly oriented microtubule bundles created in the presence of PEG. Compared to motility on single microtubules in the presence of the same concentration of PEG used to make these bundles, I see that kinesin velocity is reduced, and processivity of motors that do not reverse is also reduced on PEG bundles. In addition, I see that more motors pause when traveling on PEG bundles compared to single microtubules in the presence of PEG.

3.2.3 Kinesin Motility on Single Microtubules in the Presence of MAP65

In the cell, microtubule bundles are formed by the presence of microtubule-associated proteins (MAPs) that crosslink microtubules. Bundles formed by MAPs differ from the PEG bundles studied previously in that these bundles are spaced apart due to the presence of the crosslinking MAP. Here I study kinesin motility on antiparallel bundles formed in the presence of MAP65. This protein is a member of the MAP65 family, which consists of MAP65, Ase1, and PRC1, homologs in plant, yeast, and human, respectively (Loiodice et al., 2005). MAP65 homodimerizes (Li et al., 2007a) to selectively crosslink anti-parallel microtubules (Gaillard et al., 2008; Loiodice et al., 2005;

Subramanian et al., 2010). Negative-stain electron microscopy of microtubules incubated with MAP65 show that microtubules are crosslinked with a 25 nm spacing between filaments (Chan et al., 1999).

I first investigated the effect of MAP65 alone on kinesin motility. Kinesin motility on single microtubules with 110 nM MAP65 was compared to motility on single microtubules with 0 nM MAP65 present (Figure 3.5A). I observed a reduction in run length of kinesin motors walking on single microtubules in the presence of 110 nM MAP65 (Figures 3.5B, A.5A, A.6A). Kinesin motors traveled an average of 1.4 μm on microtubules with 0 nM MAP65 added, whereas in the presence of 110 nM MAP65, this run length dropped to 0.81 μm. No difference was observed when the association time of motors on microtubules with and without MAP65 was compared (Figures 3.5C, A.5B, A.6B). I also observed that MAP65 causes a reduction in velocity of kinesin motors (Figures 3.5D, A.5C, A.6C). On microtubules with 0 nM MAP65 present, motors moved at an average velocity of 0.38 μm/sec, whereas in the presence of 110 nM MAP65, this velocity dropped to 0.28 μm/sec. In addition, I observed a slight increase in the percentage of motors that pause during a run in the presence of MAP65 (Figure 3.5E). Without MAP65 present, I observed that 32% of motors pause. This percentage increased to 41% in the presence of MAP65.

From these studies, I show that MAP65 affects kinesin motility on single microtubules by causing a reduction in processivity and motor velocity, as well as an increase in pausing.

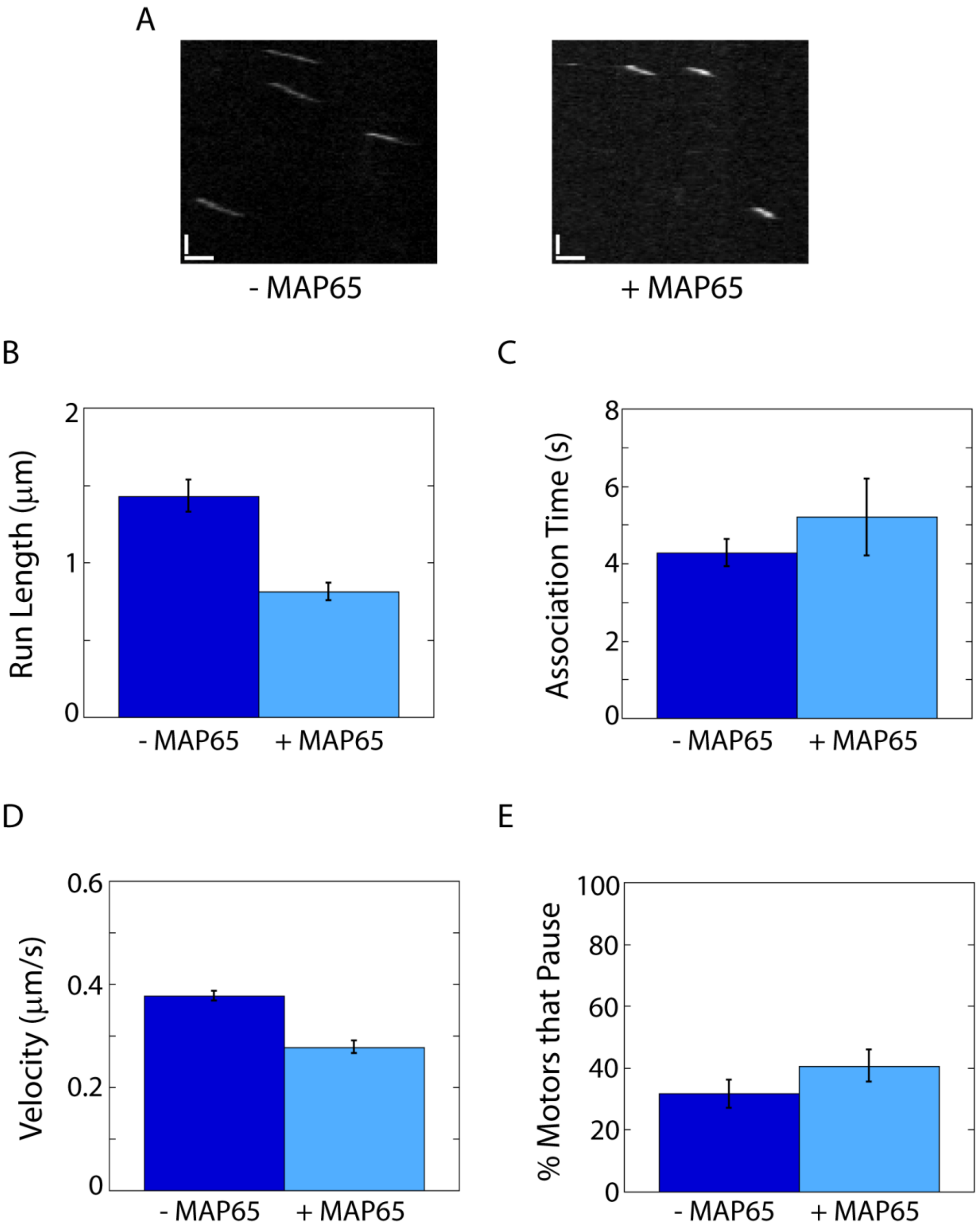

Figure 3.5 Kinesin Motility on Single Microtubules in the Presence of MAP65

A. Representative kymographs showing kinesin motility on microtubules in the absence and presence of MAP65. Vertical scale bars are 5 seconds. Horizontal scale bars are 1 µm. **B.** Run length measured as the total distance traveled by motors in the absence and presence of MAP65. Error bars represent the standard error of the mean. **C.** Association time measured as the total time motors remained bound to microtubules in the absence and presence of MAP65. Error bars represent the standard error of the mean. **D.** Moving velocity of motors on microtubules in the absence and presence of MAP65. Error bars represent the standard error of the mean. **E.** Percentage of motors that pause at least once during a run in the absence and presence of MAP65. Error bars represent the standard error of proportion. **B-E.** For data taken in the absence of MAP65, N = 104. For data taken in the presence of MAP65, N = 91.

3.2.4 Kinesin Motility on MAP65 Bundles

I next studied motility of kinesin on anti-parallel microtubule bundles formed by MAP65 (Figure 3.6A). As was described for PEG bundles, I calculated the number of microtubules in MAP65 bundles by comparing the fluorescence intensity to that of single microtubules. I found that, on average, there were 16 microtubules in bundles formed by MAP65.

Similar to PEG bundles, I observed that kinesin motors were able to reverse direction while traveling on MAP65 bundles (Figure 3.6B, left and middle kymographs). I also observed motors that walk only in a single direction on these bundles (Figure 3.6B, right kymograph).

I compared the run lengths of motors on single microtubules in the presence of MAP65 to those of motors on MAP65 bundles. Run lengths were calculated as described for kinesin motors on PEG bundles. I first measured the total distance traveled by motors (Figures 3.6C, A.7A, A.8A) and found that motors on MAP65 bundles traveled greater distances compared to motors on single microtubules in the presence of MAP65 ($p < 0.05$). When I measured the final distance, or Δx, traveled by all motors on MAP65 bundles (Figure 3.6C), I observed that there was no statistically significant difference compared to the total distance traveled by motors on these bundles ($p > 0.05$) or compared to the run lengths of motors on single microtubules in the presence of MAP65 ($p > 0.05$).

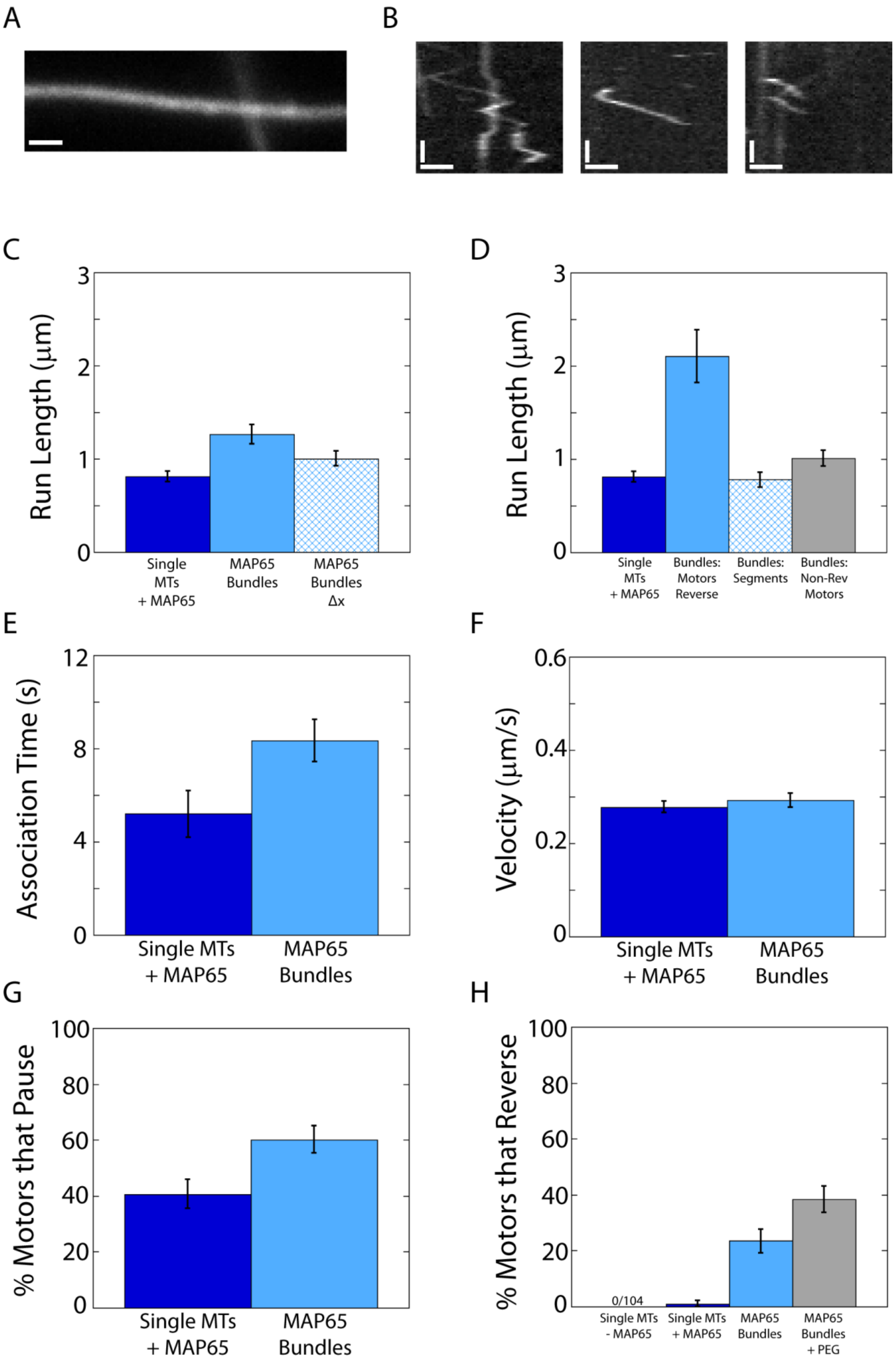
A
B
C
Run Length (μm)
0
1
2
3
Single MTs + MAP65
MAP65 Bundles
MAP65 Bundles Δx
D
Run Length (μm)
0
1
2
3
Single MTs + MAP65
Bundles: Motors Reverse
Bundles: Segments
Bundles: Non-Rev Motors
E
Association Time (s)
0
4
8
12
Single MTs + MAP65
MAP65 Bundles
F
Velocity (μm/s)
0
0.2
0.4
0.6
Single MTs + MAP65
MAP65 Bundles
G
% Motors that Pause
0
20
40
60
80
100
Single MTs + MAP65
MAP65 Bundles
H
% Motors that Reverse
0
20
40
60
80
100
0/104
Single MTs - MAP65
Single MTs + MAP65
MAP65 Bundles
MAP65 Bundles + PEG

Figure 3.6 Kinesin Motility on MAP65 Bundles

A. Image of a microtubule bundle formed in the presence of MAP65. Image was acquired using a 200 ms exposure time. Scale bar is 1 μm. **B.** Representative kymographs showing kinesin motility on MAP65 bundles. Left and middle kymograph show examples of kinesin reversals on MAP65 bundles. Right kymograph shows examples of kinesin that travel in a single direction on MAP65 bundles. Vertical scale bars are 5 seconds. Horizontal scale bars are 1 μm. **C.** Run length was measured as the total distance traveled on single MTs + MAP65 and MAP65 bundles; and as the final distance traveled (Δx) for motors on MAP65 bundles. Error bars represent the standard error of the mean. **D.** Run lengths of motors that reverse direction on MAP65 bundles were compared to those of motors that do not reverse direction on MAP65 bundles. In addition, the average distance traveled before or after reversing direction on MAP65 bundles was measured (segments). Error bars represent the standard error of the mean. **E.** Association time was measured as the total time motors remained bound to single microtubules with MAP65 and MAP65 bundles. Error bars represent the standard error of the mean. **F.** Moving velocity of motors on single microtubules with MAP65 and MAP65 bundles. Error bars represent the standard error of the mean. **G.** Percentage of motors that pause at least once during a run on single microtubules with MAP65 and MAP65 bundles. Error bars represent the standard error of proportion. **H.** Percentage of motors that reverse directions at least once during a run on single microtubules without MAP65, single microtubules with MAP65, MAP65 bundles, and MAP65 bundles with PEG. Error bars represent the standard error of proportion. **C-H.** For single microtubules with MAP65, N = 91; for MAP65 bundles, N = 98, for motors that reverse on MAP65 bundles, N = 23; for motors that do not reverse on MAP65 bundles, N = 75.

Next I measured separately the total run lengths of kinesin motors that reversed direction on MAP65 bundles versus motors that walked only in one direction along MAP65 bundles. I found that the total run length of motors that reversed direction on MAP65 bundles was greater than both the run lengths of motors that did not reverse direction on MAP65 bundles, as well as motors traveling on single microtubules in the presence of MAP65 (Figures 3.6D, A.7B, A.8B). I found that the run lengths of motors that did not reverse direction on MAP65 bundles were comparable to run lengths of kinesin motors on single microtubules in the presence of MAP65 (Figures 3.6D, A.7B, A.8B). For motors that reverse direction on MAP65 bundles, I measured the average distance traveled before or after a reverse in direction (individual segments of a run). I found that the average length of these segments was comparable to both motors on MAP65 bundles that do not reverse and to motors on single microtubules in the presence of MAP65 (Figures 3.6D, A.7B, A.8B).

I measured the total association time of motors on single microtubules in the presence of MAP65 and on MAP65 bundles (Figures 3.6E, A.7C, A.8C) and observed longer association times for motors on MAP65 bundles ($p < 0.05$). On single microtubules in the presence of MAP65, I see that motors remain bound for 5.2 sec, whereas on MAP65 bundles, this association time is increased to 8.4 sec. I did not observe a change in motor velocity on MAP65 bundles compared to single microtubules in the presence of MAP65 (Figures 3.6F, A.7D, A.8D). Motors on both single microtubules with MAP65 and MAP65 bundles traveled at approximately 0.28 μm/sec. I observed that the percentage of motors that pause is higher for motors on MAP65 bundles compared to single microtubules in the presence of MAP65. I observed that 41% of motors on single microtubules in the presence of MAP65 paused, whereas 60% of motors on MAP65 bundles were observed to pause.

As shown in the left and middle kymographs of Figure 3.6B, I observed that kinesin motors were able to reverse direction during a run on MAP65 bundles. I observed that 23% of motors on MAP65 bundles reversed direction, compared to 1% of motors on single microtubules in the presence of MAP65 (Figure 3.6H). As discussed for single microtubules in the presence of PEG, I do not believe that these reversals in motion on single microtubules are true reversals of motors. I suspect that there is another microtubule nearby that was not present in the initial microtubule image. I did not see any motors reverse on single microtubules in the absence of MAP65 (Figure 3.6H). As introduced earlier, MAP65 bundles have a 25 nm spacing in between filaments, whereas PEG bundles consist of tightly packed filaments. I added 5% PEG to pre-formed MAP65 bundles that were already bound the chamber surface with anti-tubulin antibodies. I saw that the percentage of motors that reverse on these microtubule bundles was increased compared to MAP65 bundles alone, as I observed 38% of motors to reverse when PEG was added.

Unlike in the case of PEG bundles, where I observed kinesin motility to be disrupted on these tightly packed bundles, I do not see that kinesin motility is disrupted on MAP65 bundles in comparison to single microtubules with the same concentration of MAP65 present. I see no effect of the formation of bundles on kinesin motor velocity. I see that for motors that reverse direction, kinesin processivity is actually increased on MAP65 bundles compared to single microtubules with MAP65 present, while motors that do not reverse exhibit no difference in processivity compared to single microtubules with MAP65.

3.2.5 Kinesin Motility on Cellular Bundles

Finally, I studied kinesin motility on parallel microtubule bundles derived from neuronal-like cells. For these experiments, I used CAD cells, a mouse central nervous system catecholaminergic cell line (Qi et al., 1997). Upon serum starvation, these cells differentiate to form neuronal processes (Figure 3.7A). These processes have been shown by EM to contain parallel arrays of microtubules and neurofilaments (Qi et al., 1997). Studies have shown that many of the major MAPs typically found in axons are missing in differentiated CAD cells. However, MAP1b and LIS1 are thought to be present in these processes (Bisig et al., 2009; Li et al., 2006). In addition, both acetylated and tyrosinated tubulin have been detected in the neuronal processes of these differentiated cells (Bisig et al., 2009; Li et al., 2006).

To study kinesin motility on these cellular bundles, I modified an existing protocol used to expose and stabilize the actin cytoskeleton of keratocytes (Sivaramakrishnan and Spudich, 2009). I treated differentiated CAD cells with detergent and Taxol to simultaneously expose and stabilize the microtubule cytoskeleton. Using BODIPY-Taxol, I showed that microtubule filaments are preserved after this procedure (Figure 3.7B). I was then able to add purified kinesin motors to this exposed microtubule network to study motility on axonal-like processes.

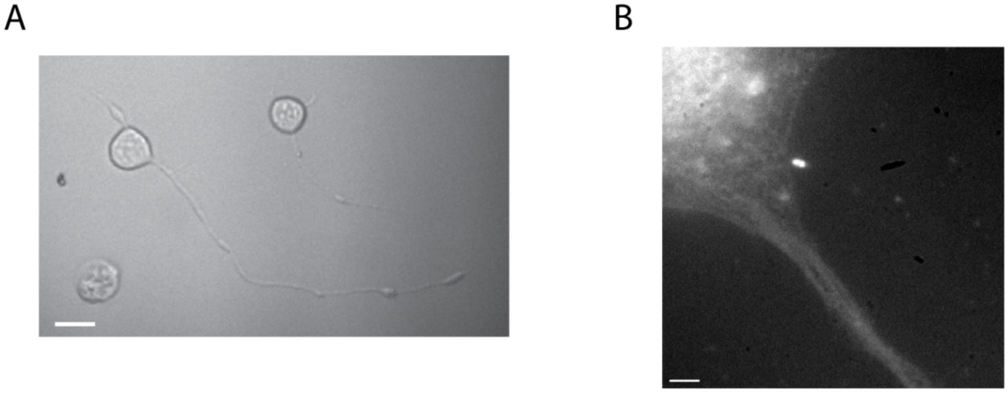

Figure 3.7 CAD Cells as a Model to Study Parallel Microtubule Bundles

A. Differentiated CAD cells imaged with transmitted light. Scale bar is 3 μm. **B.** Differentiated CAD cell following exposure of microtubule cytoskeleton. BODIPY-taxol was added to cytoskeleton to verify the presence of microtubules after treatment. Scale bar is 3 μm.

I compared kinesin motility on CAD cell bundles to motility on single microtubules polymerized in vitro (Figure 3.8A). Unlike the PEG and MAP65 bundles studied, I did not observe any motors that reversed direction while walking on these cellular bundles. I measured run lengths of kinesin motors on CAD cell bundles and single microtubules polymerized in vitro (Figures 3.8B, A.9A, A.10A) and found that there was no statistically significant difference in run lengths between these two types of tracks ($p > 0.05$). I also found that there was no significant difference between motor association times (Figures 3.8C, A.9B, A.10B) on CAD cell bundles versus single microtubules polymerized in vitro ($p > 0.05$). I did observe a statistically significant decrease in velocity of motors on CAD cell bundles compared to motors on single microtubules polymerized in vitro ($p < 0.05$). On single microtubules polymerized in vitro, motors moved at 0.44 μm/sec, whereas on CAD cell bundles, this velocity was decreased to 0.35 μm/sec (Figures 3.8D, A.9C, A.10C). This decrease in velocity observed for motors on CAD cell bundles could be due to the presence of endogenous MAPs along these microtubules. In addition, I did not observe a difference in the percentage of motors that paused on single microtubules polymerized in vitro versus on CAD cell bundles (Figure 3.8E).

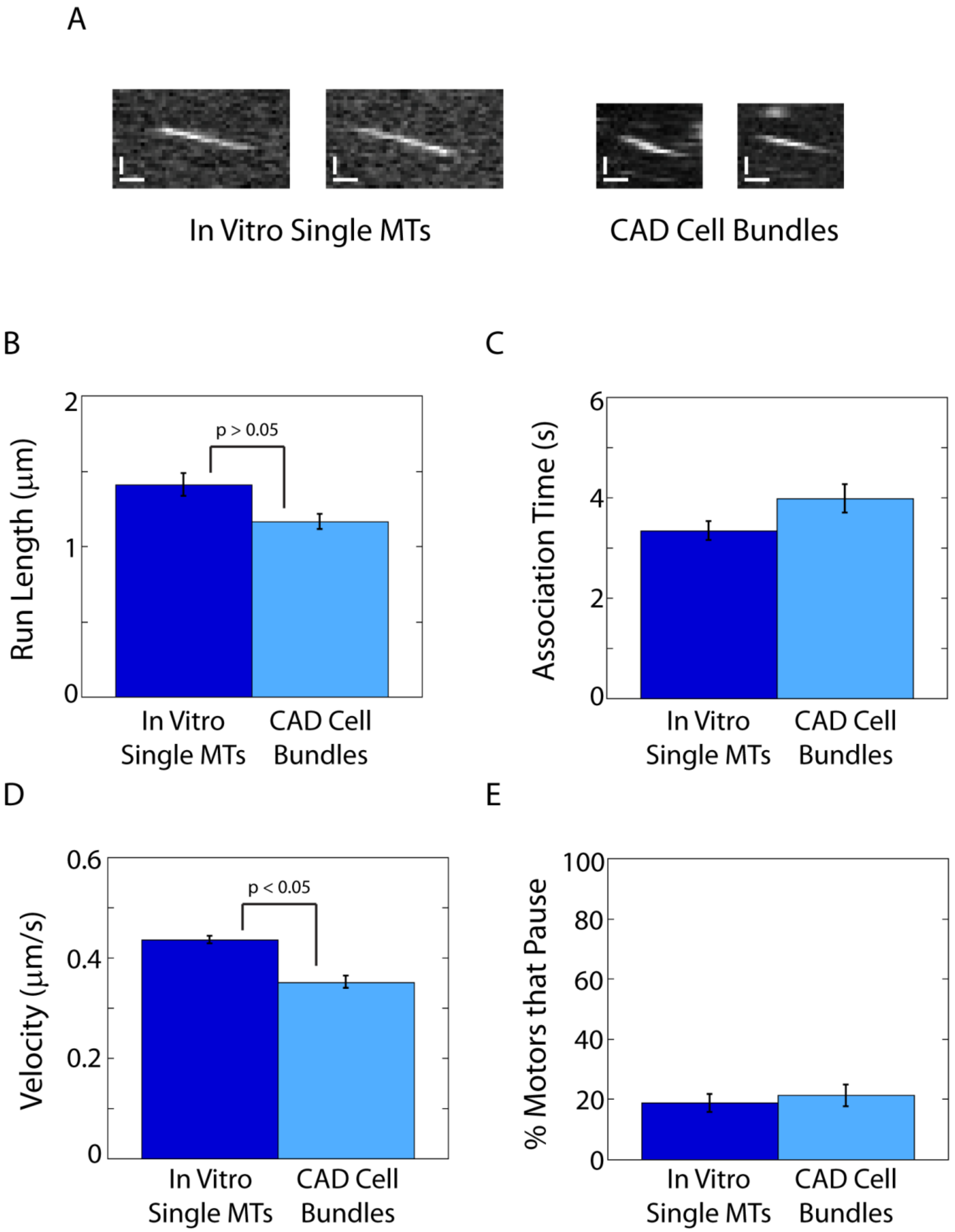

Figure 3.8 Kinesin Motility on Cellular Bundles

A. Representative kymographs showing kinesin motility on single microtubules polymerized in vitro and on microtubule bundles derived from CAD cells. Vertical scale bars are 2.5 seconds. Horizontal scale bars are 0.5 μm. **B.** Run length measured as the total distance traveled by motors on single microtubules polymerized in vitro and on microtubule bundles derived from CAD cells. Error bars represent the standard error of the mean. **C.** Association time measured as the total time motors remained bound to microtubules on single microtubules polymerized in vitro and on microtubule bundles derived from CAD cells. Error bars represent the standard error of the mean. **D.** Moving velocity of motors on single microtubules polymerized in vitro and on microtubule bundles derived from CAD cells. Error bars represent the standard error of the mean. **E.** Percentage of motors that pause at least once during a run on single microtubules polymerized in vitro and on microtubule bundles derived from CAD cells. Error bars represent the standard error of proportion. **B-E.** For data taken on single microtubules polymerized in vitro, N = 160. For data taken on microtubule bundles derived from CAD cells, N = 122.

3.3 Discussion

I have examined the motility properties of kinesin-1 on microtubule bundles. Here, I have studied three different types of bundles: 1) tightly spaced, randomly oriented bundles formed in the presence of PEG, 2) antiparallel bundles with a 25 nm spacing between microtubules, and 3) parallel bundles derived from axonal-like processes.

To create tightly spaced, randomly oriented microtubule bundles, I chose to use polyethylene glycol (PEG). While there are other crowders that could be used to induce bundle formation through depletion forces, I chose PEG due to the fact that it is an inert polymer. Other polymers, such as methylcellulose, are highly charged and could disrupt the interactions of kinesin motors with microtubules. Thus, PEG allows me to create depletion forces to form microtubule bundles without disturbing electrostatic interactions within the system.

PEG acts as a molecular crowder, and can thus create an environment that resembles that of the cytoplasm, which is crowded with high concentrations of protein. The high concentration of protein in the cytoplasm generates an osmotic pressure within the cell, which has been estimated to be approximately 0.22 atm (Lodish et al., 2000). I calculated the osmotic pressure produced by the presence of PEG in my assays to be 0.03 atm. This pressure created by 5% PEG is lower than that which is estimated in vivo. However, it is still interesting to consider the fact that the PEG in these assays generates an osmotic pressure within the system, a pressure that is absent in most in vitro assays. Future studies using different sized PEG polymers to create osmotic pressures that more closely resemble that which is present in the cytoplasm could provide further insights on the effect of intracellular pressure on motor transport.

I showed that PEG, in addition to initiating microtubule bundle formation, also affects the motility of kinesin motors on single microtubules. I observed an increased interaction of kinesin motors with microtubules in the presence of PEG. This was evident by both an 8-fold increase in kinesin binding along microtubules and an approximately 2-fold increase in the run length of kinesin motors on single microtubules in the presence of PEG. The observed increase in interaction between kinesin and microtubules could be due to PEG induced depletion forces that act to keep kinesin motors in close contact with the microtubules. The increase in run length of motors on single microtubules in the presence of PEG could indicate that motors are more processive in the presence of PEG. Alternatively, it is possible that these motors dissociate after a typical run length of approximately 1μm, but are kept in close range of the microtubule because of depletion forces, which allows them to immediately rebind the microtubule and continue walking. Because I used a 500 ms exposure time for these studies, it is possible that an event where kinesin unbinds and quickly rebinds would be viewed as continued processive motion in this time frame.

I also observed an approximate 2-fold increase in the percentage of kinesin motors that pause on single microtubules in the presence of PEG. One explanation for this increase is that because the run lengths of motors double on microtubules with PEG, the probability that a motor will pause during its run could double as well, since it is walking for twice as long. A second explanation is that the additional pausing observed is due to obstacles along the lattice that would normally cause a motor to dissociate. In the presence of PEG, it is likely that motors would be able to remain bound to the microtubule upon encountering such obstacles, allowing it to wait for this obstacle to move. Such events would be observed as a pause in a kinesin run. A third explanation for this increase in pausing is that the PEG could induce a physical change to the microtubule lattice that increases the propensity of kinesin to pause while traversing these tracks.

Like PEG, I also observed that MAP65 alone affects kinesin motility on single microtubules. However, rather than enhancing motility, MAP65 reduced kinesin motility on single microtubules. I showed that the run length and velocity of kinesin motors were reduced on single microtubules with MAP65. I also observed a slight increase in the percentage of motors that pause in the presence of MAP65. This negative effect on kinesin motility suggests that the binding of MAP65 along the microtubule disrupts kinesin motility. MAP65 could disrupt the motility of kinesin by either specifically binding to and blocking the microtubule binding site of kinesin or by sterically blocking kinesin motility due to its size and position along the microtubule. Because kinesin and MAP65 have different binding sites along the microtubule, as kinesin binds predominantly to β-tubulin (Song and Mandelkow, 1993) while MAP65 binds to α-tubulin (Li et al., 2007b), I believe that MAP65 disrupts kinesin motility through a steric mechanism, rather than acting as a roadblock. I can compare my results with MAP65 to a known roadblock for kinesin, tau. In the presence of tau, kinesin run lengths are reduced by about 50%, however the velocity of motors is unaffected (Dixit et al., 2008). Thus, in the presence of a roadblock, kinesin motors are expected to show a reduced run length, but no change in velocity, resulting in a reduced association time of motors. In the presence of MAP65, I observed a reduction in run length, but also saw a reduction in velocity. These results are different than what is observed with tau, which acts as a physical roadblock for kinesin, and therefore suggests that MAP65 inhibits kinesin through a mechanism other than acting as a roadblock. This, together with the fact that MAP65 does not compete with kinesin-1 for a binding site on the microtubule (Li et al., 2007b; Song and

Mandelkow, 1993) supports the idea that MAP65 inhibits kinesin motility through a steric mechanism.

When I observed kinesin motility on PEG bundles, I saw that motility was reduced on these tracks compared to single microtubules in the presence of PEG. This was shown by a reduction in run length for motors that did not reverse direction, a reduction in velocity, and an increase in the percentage of motors that pause on PEG bundles. While I did not observe a statistically significant reduction in run length when the total run length was calculated for all motors on PEG bundles, I observed a pronounced difference when the total run lengths of motors that reverse direction were calculated separately from those of motors that do not reverse. The total run lengths of motors that reverse direction on PEG bundles were similar to the run lengths of motors on single microtubules in the presence of PEG. However, the run lengths of motors that did not reverse direction were about half the length of motors on single microtubules in the presence of PEG. I observed a similar reduction when I calculated individual segment lengths of motors that reverse direction on PEG bundles. I also observed an increase in the percentage of motors that pause on PEG bundles, as well as a reduction in velocity of these motors, compared to motors on single microtubules with PEG. I believe that the decrease in velocity observed could be due to an increase in the number of short pauses of motors. While I calculated the velocity as the moving velocity so that pauses were excluded, short pauses could exist that are shorter than a single 500 ms time frame. These would not be distinguishable from motion and would therefore be included in the average moving velocity of motors.

The fact that kinesin motility is reduced on PEG bundles compared to motility on single microtubules with PEG suggests that the architecture of PEG bundles creates obstacles for kinesin motors that disrupt motor motility. Two possibilities for how the bundle architecture could disrupt motility are depicted in Figure 3.9A. One possibility is that staggered overlapping microtubules create roadblocks for kinesin motors (Figure 3.9A, black arrowhead, a). A second possibility is that pockets are created within the bundle between overlapping segments of microtubules (Figure 3.9A, blue arrowheads, b). Motors could walk within these pockets, but the contact point where the two microtubules merge will act as an obstacle. I show that motors that are able to switch microtubule tracks (as indicated by a reversal) are able to overcome the reduction in processivity observed for motors that do not reverse. I presume that these motors are able to switch to a neighboring microtubule upon encountering an obstacle, enabling them to circumvent obstacles formed by the bundle architecture.

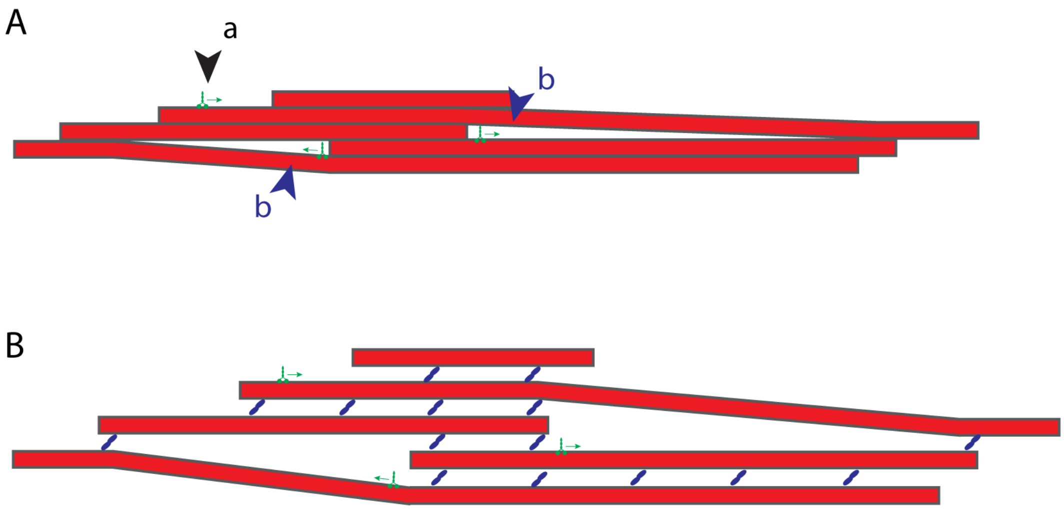

Figure 3.9 Kinesin Motility on PEG versus MAP65 Microtubule Bundles

A. Schematic showing potential architecture of tightly packed PEG bundles. Microtubules are shown as red filaments, kinesin motors are shown in green. Black arrow points to a motor that could encounter a staggered, overlapping microtubule as an obstacle. Blue arrows point to motors that are walking in a pocket within the microtubule bundle. **B.** Schematic showing potential architecture of microtubule bundles formed in the presence of MAP65. Here, microtubules are spaced apart by 25 nm due to the presence of MAP65.

The ability of overlapping microtubules to pose as obstacles for kinesin motors is supported by previous work that has shown that kinesin motors have a high propensity for dissociating at perpendicular microtubule intersections when traveling on the ‘underpass’ microtubule (Ross et al., 2008). Such intersections are obstacles that are similar to what could be encountered by kinesin motors traveling on PEG bundles, in that there is a microtubule filament blocking the path. Interestingly, in these microtubule intersection studies, a small percentage of motors on ‘underpass’ microtubules were able to switch microtubule tracks and walk along the perpendicular microtubule (Ross et al., 2008). Such events could be similar to the reversal events observed in my studies here, where kinesin motors switch to an oppositely oriented microtubule.

Unlike in the case of PEG bundles, I did not observe MAP65 bundle architecture to negatively affect kinesin motility. I saw an increase in the total run length of motors on MAP65 bundles, which I found to be attributed to the subset of motors that are able to switch microtubules within the bundle. When I measured the run lengths of motors that reverse direction separately from those motors that do not reverse direction, I found that motors that reverse direction had much longer run lengths compared to motors on single microtubules in the presence of MAP65, whereas motors that do not reverse direction had run lengths comparable to those of motors on single microtubules in the presence of MAP65. In addition, I measured the length of individual run segments of motors that reverse direction and found that the average length before or after reversing direction was similar to the run length of motors on single microtubules in the presence of MAP65. Thus, I see that motors are able to travel the same distance on MAP65 bundles as motors on single microtubules in the presence of MAP65, with the exception of motors that are able to switch microtubule tracks, which I show to be more processive. This gain in processivity of motors that switch tracks over motors on single microtubules with

MAP65 suggests that motors on MAP65 bundles could be able to circumvent the obstacles (MAP65 molecules) that were shown to reduce the run length of kinesin motors on single microtubules.

While kinesin velocity was reduced on PEG bundles, I saw that kinesin velocity was unaffected by the architecture of MAP65 bundles. I did, as with PEG bundles, see a similar increase in the percentage of motors that pause on MAP65 bundles.

Taken together, these results suggest that the overall motility of kinesin is unaffected by the architecture of MAP65 bundles, which is in contrast to what was observed for kinesin motility on PEG bundles. One explanation for this difference is that the spacing between microtubules in MAP65 bundles creates a more organized bundle architecture that does not affect kinesin motility. As depicted in Figure 3.9B, microtubules themselves no longer pose as roadblocks as could occur in PEG bundles. While the MAP65 molecules crosslinking the microtubules in these locations could act as obstacles, they do not block motility on all protofilaments of that face of the microtubule, as tightly packed microtubules could in PEG bundles. Therefore, if a kinesin motor is walking along a protofilament that is not obstructed by MAP65, it could pass between these microtubules. This idea is further supported by the fact that a reduction in processivity was not observed for motors on CAD cell bundles, which are presumably also spaced apart by MAPs. It is also possible that I did not observe reduced processivity on MAP65 bundles because the run lengths were already shortened due to the presence of MAP65. These reduced run lengths were shorter than the reduced run lengths of kinesin motors on PEG bundles. Thus, on MAP65 bundles, it could be that kinesin motors never reached the length scale needed to observe a reduction in processivity that is caused by the bundle architecture.

On bundles formed from both PEG and MAP65, I observed some kinesin motors to reverse directions during a run. I believe these reversals occur when a kinesin motor switches tracks to a neighboring microtubule oriented in the opposite direction. This is supported by the fact that I did not observe any kinesin motors to reverse on parallel microtubule bundles derived from neuronal processes of CAD cells, where all microtubules are oriented in the same direction.

How kinesin motors switch to adjacent microtubule tracks is unclear. I speculate that this could occur in one of two ways. First, motors could unbind, diffuse, and rebind to a neighboring microtubule within the 500 ms exposure time. If the motor landed on an adjacent microtubule oriented in the opposite direction within 250 nm of where the motor dissociated, this event would appear as a reversal in motility. Motors traveling within the bundle could be confined after dissociation from their original track. Rather than diffusing away from the microtubule, as is often observed in assays with single microtubules, diffusion of these motors is more likely to be restricted to short distances, increasing the probability that they will find a new binding site in close proximity on an adjacent microtubule. Future work with brighter fluorophores, such as quantum dots, that would allow for imaging with higher temporal and spatial resolution could allow for the visualization of such diffusion events.

Depending on the position of microtubules within the bundle, a second mechanism by which kinesin motors could switch microtubule tracks during a run is if these motors actually step from one microtubule onto a neighboring microtubule track. While it is generally thought that kinesin-1 is very strict in its stepping pattern, only walking along a single protofilament with 8 nm steps, several studies have demonstrated that there is an approximately 15-20% probability that kinesin-1 will side-step onto an adjacent protofilament (Schaap et al., 2011; Yildiz et al., 2008). These side-steps were observed with high resolution studies using quantum dots and atomic force microscopy (Schaap et al., 2011; Yildiz et al., 2008). Thus, it can be conceived that if a microtubule within a bundle is located in close enough proximity to the protofilament path on which a kinesin motor is traversing, that it could step onto this neighboring microtubule. In my studies, I observe motors to switch onto oppositely oriented microtubules. If motors were to step onto an oppositely oriented microtubule, they would have to reorient their motor domains such that they would be correctly directed to walk towards the plus end of the new microtubule track. Previous work has demonstrated that the kinesin-1 neck linker is a flexible polypeptide that can swivel during motility (Gutierrez-Medina et al., 2009; Hunt and Howard, 1993). Single kinesin motors propelling a microtubule in a filament gliding assay have been shown to be able to rotate the microtubule 360^o, an action which has been attributed to the flexibility of the kinesin neck linker. This ability of the kinesin neck linker to swivel during motility could allow a kinesin motor to reorient its motor domain upon side stepping onto an adjacent, oppositely oriented microtubule within a bundle. While this mechanism of switching to adjacent microtubules is unlikely in the case of MAP65 bundles, where microtubules are spaced apart by 25 nm, it is a mechanism that could explain track switching in tightly packed, PEG bundles.

I observed that a larger percentage of motors switch directions on PEG bundles compared to MAP65 bundles (34% versus 23%, respectively). This suggests that the tight spacing between microtubules in PEG bundles enables motors to more easily switch microtubule tracks, possibly by enabling motors to switch by side-stepping onto adjacent microtubules. It is likely that motors on MAP65 bundles are restricted to diffusion-based track switching whereas motors on PEG bundles could switch tracks by side-stepping or diffusion. While I saw only a 10% increase in the percentage of motors that switch tracks on PEG bundles compared to on MAP65 bundles, this percentage is not entirely representative of the number of motors that switch tracks, and is likely depressed compared to the true percentage. In MAP65 bundles, all microtubules are oriented antiparallel to each other. This means that any kinesin motor that switches to an adjacent microtubule track will be detected, as it will always result in a reversal in kinesin motion. In the case of PEG bundles, microtubules are oriented randomly, with some adjacent microtubules aligned parallel, and others aligned antiparallel. Motors that switch to a parallel microtubule track will not be detected, as I do not have high enough resolution to identify these events. Thus, the reported percentage for motors that switch microtubule tracks on PEG bundles is most likely even higher than what I have measured here. I further show that tighter spacing between microtubules within a bundle increases the probability of motors switching microtubule tracks by adding PEG to pre-formed MAP65 bundles. This addition of PEG increases the percentage of motors that reverse direction from 23% on MAP65 only bundles to 38% on MAP65 bundles with PEG.

The studies presented here shed light on the mechanisms by which kinesin motors move on complex microtubule cytoskeletons, specifically microtubule bundles. These bundles are found in many areas of the cell. In neurons, for example, parallel microtubule bundles populate axonal processes while randomly oriented microtubule bundles are found in dendrites. All cell types generate antiparallel microtubule bundles during cell division at the spindle midzone. Transport of cargos by molecular motors along these microtubule bundle architectures is imperative for cell function.

Here I demonstrate how kinesin motors navigate these complex microtubule networks. I show that MAPs are important for not only generating microtubule bundles in cells, but for maintaining spacing between microtubules within a bundle. I show that this spacing between microtubules could prevent overlapping, staggered microtubules from posing as obstacles for kinesin motors. In addition, I show that the bundled architecture of microtubules could help to promote motility by allowing motors to switch microtubule filament tracks during transport to circumvent obstacles. The importance of such a mechanism is emphasized by the fact that cargos have been observed to switch microtubule tracks in vivo. In *Ustilago maydis* fungal cells, an antiparallel array of bundled microtubules populates the center of the cell. Here, cargos carried by kinesin-3 are observed to exhibit bidirectional motion in the absence of dynein motors (Schuster et al., 2011). This suggests that these cargos are able to readily switch microtubule tracks within this antiparallel bundle. From the studies presented here, I propose that microtubule bundles formed by MAPs are imperative for the long distance transport of cargos, as they function to organize microtubule filaments within the bundle and provide adjacent tracks that motors can easily switch between to potentially avoid obstacles along their path.

3.4 Methods

3.4.1 Protein Purification. A human kinesin-1 construct truncated at amino acid 560 fused to a C-terminal GFP tag and a 6x His Tag was expressed using a pET17b expression vector. Expression with IPTG and affinity purification with Nickel beads (Qiagen) were carried out as described previously (Pierce and Vale, 1998). A MAP65 construct fused to an N-terminal 6x His Tag was expressed using a pET28a expression vector. This MAP65 construct was provided by the Dixit Lab. Expression with IPTG and purification with Nickel beads (Qiagen) were carried out as described previously (Tulin et al., 2012). GFP-kinesin and MAP65 protein concentrations were quantified by comparison to known BSA standards on a Coomassie-stained SDS-PAGE gel.

3.4.2 Microtubule Polymerization. Labeled microtubules were prepared using a 1:4 ratio of labeled:unlabeled tubulin. Unlabeled tubulin was purified from porcine brain as described previously (Peloquin et al., 2005). Tubulin was labeled using DyLight 649 or DyLight 550 dyes as described previously (Hyman et al., 1991). To prepare microtubules, both unlabeled and labeled tubulin were brought to 5 mg/mL in PEM-100 (100 mM K-Pipes, pH 6.8, 2 mM $MgSO_4$, 2 mM EGTA). Tubulin was centrifuged at 4^oC for 10 minutes at 366,000 xg to remove tubulin aggregates. The remaining tubulin in the supernatant was mixed with 1 mM GTP and polymerized at 37^oC for 20 minutes. 50 μM Taxol was added to stabilize polymerized microtubules, followed by another 20 minute incubation at 37^oC. Polymerized microtubules were centrifuged at 25^oC for 10 minutes at 14,000 x g to separate unincorporated tubulin. The microtubule pellet was resuspended in 50 μL PEM-100 with 40 μM Taxol.

3.4.3 Motility on Single Microtubules. Assays were carried out in 10 μL flow chambers made of a glass slide attached to a cover slip with double-stick tape. Prior to use, cover slips were biologically cleaned and treated with dimethyldichlorosilane solution, 2% w/v (GE Healthcare). Flow chambers were first incubated with 2% anti-tubulin antibody in PEM-100 for 5 minutes to attach microtubules, followed by a 5 minute incubation with 5% Pluronic F-127 (Sigma) in PEM-100 to block the surface. Labeled microtubules (0.05 mg/mL microtubules, 20 μM Taxol in PEM-100) were allowed to bind for 10 minutes. Excess microtubules were removed with a wash step (10 mM DTT, 20 μM Taxol in PEM-100). Finally, motility mix was added to the chamber (2 nM GFP kinesin, 0.05% Pluronic F-127, 25 μM Taxol, 0.25 mg/mL BSA, 50 mM DTT, 0.5 mM ATP, 15 mg/mL glucose, 0.5 mg/mL glucose oxidase, 0.15 mg/mL catalase in PEM-100). For motility on single microtubules in the presence of PEG, 5% PEG mw 40,000 was added to the microtubule wash step and motility mix. For these assays, only 0.3 nM GFP-kinesin was added to the motility mix.

3.4.4 Motility on PEG Microtubule Bundles. PEG microtubule bundles were made by mixing 0.05 mg/mL polymerized microtubules with 5% (w/w) PEG mw 40,000 and 20 μM Taxol in PEM-100. Assays were carried out in 10 μL flow chambers as described for motility assays on single microtubules. Flow chambers were first incubated with 2% anti-tubulin antibody in PEM-100 for 5 minutes to attach microtubules, followed by a 5 minute incubation with 5% Pluronic F-127 (Sigma) in PEM-100 to block the surface. PEG microtubule bundles were allowed to bind for 10 minutes. Excess microtubules were removed with a wash step (10 mM DTT, 20 μM Taxol, 5% PEG in PEM-100). Finally, motility mix was added to the chamber (0.14 nM GFP kinesin, 0.05% Pluronic F-127, 25 μM Taxol, 0.25 mg/mL BSA, 50 mM DTT, 0.5 mM ATP, 5% PEG, 15 mg/mL glucose, 0.5 mg/mL glucose oxidase, 0.15 mg/mL catalase in PEM-100).

3.4.5 Motility on MAP65 Microtubule Bundles. MAP65 microtubule bundles were made by mixing 0.05 mg/mL polymerized microtubules with 112 nM MAP65 and 20 μM Taxol in PEM-100. Assays were carried out in 10 μL flow chambers as described for motility assays on single microtubules. Flow chambers were first incubated with 2% anti-tubulin antibody in PEM-100 for 5 minutes to attach microtubules, followed by a 5 minute incubation with 5% Pluronic F-127 (Sigma) in PEM-100 to block the surface. Microtubules labeled with DyLight 550 were added to the chamber and incubated for 10 minutes. MAP65 microtubule bundles formed from microtubules labeled with DyLight 649 were then allowed to bind for 10 minutes. Excess microtubules were removed with a wash step (10 mM DTT, 20 μM Taxol, 112 nM MAP65 in PEM-100). Finally, motility mix was added to the chamber (0.7 nM GFP kinesin, 0.05% Pluronic F-127, 25 μM Taxol, 0.25 mg/mL BSA, 50 mM DTT, 0.5 mM ATP, 112 nM MAP65, 15 mg/mL glucose, 0.5 mg/mL glucose oxidase, 0.15 mg/mL catalase in PEM-100).

3.4.6 CAD Cell Culture. CAD cells were maintained in DMEM/F12 (Gibco, 12400-024) media with 10% FBS. To induce differentiation, CAD cells were plated on 20 mm glass bottom dishes (20,000-40,000 cells per plate) in DMEM/F12 plus 10% FBS. After cells adhered to the glass dish, cells were rinsed two times in DMEM/F12 without FBS. Fresh DMEM/F12 media without FBS was added and the cells were left for 2-3 days to grow processes.

3.4.7 Motility on CAD Cell Microtubule Bundles. To expose the microtubule cytoskeleton of differentiated CAD cells, a previously described protocol for studying the actin cytoskeleton was modified (Sivaramakrishnan and Spudich, 2009). Cells were washed two times in 85% PBS, followed by exposure to Extraction Buffer (50 mM Imidazole, pH 6.8, 50 mM KCl, 0.5 mM $MgCl_2$, 0.1 mM EDTA, 1 mM EGTA, 50 mM Taxol, 1% Triton X-100, 4% PEG, mw 40,000) for 4 minutes. A Taxol Solution (85% PBS with 50 μM Taxol) was added to the cells for 45 minutes to stabilize the microtubule cytoskeleton. Cells were then rinsed (1 mg/mL BSA, 50 μM Taxol in PEM-100) for 5 minutes. Finally, motility mix was added to the cells (0.7 nM GFP kinesin, 25 μM Taxol, 1 mg/mL BSA, 50 mM DTT, 0.5 mM ATP, 15 mg/mL glucose, 0.5 mg/mL glucose oxidase, 0.15 mg/mL catalase in PEM-100). For experiments where the microtubule cytoskeleton was observed with fluorescent Taxol, was added as a tenth of the final Taxol concentration (5 μM BODIPY-taxol with 45 μM unlabeled taxol).

3.4.8 Imaging. An image of the microtubules was acquired using epi-fluorescence prior to imaging GFP-kinesin in TIRF. Two minute recordings of kinesin motility were taken with a 500 ms exposure time using Total Internal Reflection Fluorescence (TIRF) microscopy with a 50 mW 488 Cyan laser (Spectra-Physics) illumination built around an inverted Nikon Ti-E microscope (Nikon). The microscope uses a 60x 1.49 NA objective and images were collected using an iXon electron multiplier CCD camera (Andor) after a 4x beam expander. The final pixel size was 67.5 nm. Images were acquired with no delay and saved as nd2 files and exported as 16-bit tif files.

3.4.9 Data Analysis. Kinesin motility was analyzed using kymographs generated from the ImageJ plugin, MultipleKymograph. For velocity measurements, only the moving segments of runs were measured, so as to omit pauses from the overall velocity measurement. To determine the number of microtubules in PEG and MAP65 bundles, the fluorescence intensity of a single microtubule was compared to that of the microtubule bundle. Fluorescence intensity was determined by drawing a line perpendicular to the microtubule in ImageJ to create a plot profile. This data was fit to a Gaussian function in Kaleidagraph to determine the height of the fluorescence peak, which corresponds to the average fluorescence of the microtubule or microtubule bundle. The fluorescence intensity of a microtubule bundle was divided by the average fluorescence of a single microtubule to determine the number of microtubules within the bundle.

CHAPTER 4

STUDY OF KINESIN MOTOR DOMAIN MUTANTS

4.1 Introduction

Intracellular transport relies on the proper function of microtubule motor proteins (Hirokawa, 1998). While there are numerous motor proteins involved in this transport process, disruption of just one motor type is enough to result in transport defects, and has been shown to be linked to the onset of neurodegenerative disease (Perlson et al., 2010). A thorough understanding of the mechanism by which motor proteins function to transport cargo is imperative for tackling neurodegenerative disease. A common method used to gain mechanistic insights into protein function is to study specific mutants, where known amino acids have been substituted.

One study aimed at characterizing the kinesin-1 motor domain used random mutagenesis to create mutations within the *Drosophila* kinesin heavy chain (KHC) (Brendza et al., 1999). These mutants were screened in vivo to determine which affected axonal transport in *Drosophila.* One of the mutants that arose from this study, E164K, was found to be lethal in *Drosophila*. Only 50% of flies with this mutation survived through later stages of development, and no flies survived to adulthood (Brendza et al., 1999). A recent study of this E164K mutation in *Drosophila* examined the effect this mutation has on cargo transport (Djagaeva et al., 2012). By measuring the flux of labeled organelles past a certain point in *Drosophila* axons, it was shown that the flux of dense core vesicles was only approximately 35% of that observed in neurons with wildtype kinesin, while no mitochondria were observed in the segment examined with mutant motors (Djagaeva et al., 2012).

This E164K mutant was further studied in vitro to gain a better understanding of the role of this particular amino acid in kinesin motor motility. It was found that this mutant did retain some motility, as microtubule gliding assays with this protein showed movement of microtubules, although microtubule gliding rates were reduced 4-fold compared to wildtype motors (Brendza et al., 1999).

Further biochemical studies were carried out to better characterize the differences between the E164K mutant and wildtype kinesin (Klumpp et al., 2004). For these studies, a second mutant was also studied where this residue was mutated to an alanine, E164A (Klumpp et al., 2003). First, it was found that ATP binding was 3-fold tighter in the case of E164K and E164A mutants compared with wildtype motors (Klumpp et al., 2004; Klumpp et al., 2003). Second, it was observed that while the ATP turnover rates of E164K and E164A mutants were reduced 2 to 4-fold, respectively, compared to wildtype motors, ATP hydrolysis rates were 2 to 4 times faster than that of wildtype kinesin (Klumpp et al., 2004; Klumpp et al., 2003). Third, these studies showed that only approximately 30% of the E164K and E164A kinesin mutants' active sites were able to hydrolyze ATP (Klumpp et al., 2004; Klumpp et al., 2003).

From these studies, it was hypothesized that these mutants are able to carry out the ATPase cycle normally on the first motor head, but get stalled on the second head (Klumpp et al., 2004; Klumpp et al., 2003). In this scenario, the first head of the mutant kinesin motors would be able to release ADP and tightly bind the microtubule (Figure 4.1B). This head would then bind ATP, resulting in conformational changes that allow the second head to swing forward and bind the microtubule ahead of head 1. At this point, head 2 of a wildtype motor would only weakly bind the microtubule at first, and following ATP hydrolysis on head 1, would release its ADP and then tightly bind the microtubule. However, in the case of these mutants, the fast ATP hydrolysis at head 1 is thought to cause head 2 to tightly bind the microtubule prematurely, before its release of ADP. This would inhibit ATP from binding to head 2, stalling the ATPase cycle. This hypothesis led to the conclusion that these mutant motors are unable to walk processively along the microtubule, and remain bound to the microtubule in a rigor state (Klumpp et al., 2004; Klumpp et al., 2003).

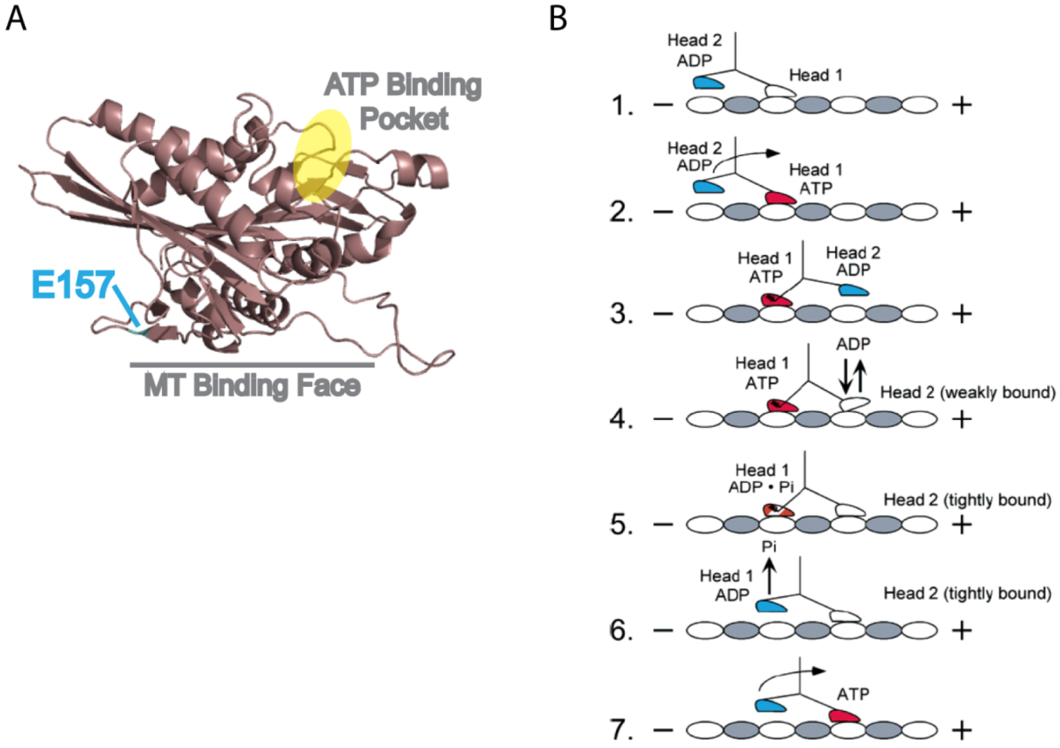

Figure 4.1 Kinesin E157 Residue is Located on the Motor Domain

A. Crystal structure showing the human kinesin motor domain. Amino acid residue E157 is highlighted in cyan. ATP binding pocket is highlighted in yellow. Structure constructed from PDB file 1BG2. **B.** ATPase cycle of the kinesin-1 motor. Different nucleotide states are indicated by motor domain coloring. Red indicates the ATP-bound state, blue indicates the ADP-bound state, and white indicates the apo state. Figure was reprinted from Klumpp et al, 2003. Copyright (2003) American Chemical Society.

While biochemical studies are a powerful tool in characterizing protein function, these studies provide information on the average behavior of many molecules. Here, I use Total Internal Reflection Fluorescence (TIRF) microscopy to visualize and study the motility properties of individual kinesin mutants. I study these mutants in the human kinesin gene, E157A and E157K. I show that both mutants are actually able to take many consecutive steps, allowing for their processive motion along the microtubule. While these mutants move slower and have shorter run lengths compared to wildtype motors, they are able to take up to 100 consecutive steps before dissociating. In addition, I show that motility of E157K motors are drastically reduced in gliding assays compared to motility in single molecule studies of this mutant. These results show that while both single E157A and E157K mutant motors possess some defects in motility, E157K motility defects are more pronounced in a multiple-motor assay. I hypothesize that the E157K mutant could have a defect in its ability to work cooperatively with multiple motors. The results presented here are in contrast to conclusions from prior studies and provide an interesting avenue to study mechanisms by which cargo transport can be disrupted.

4.2. Results

4.2.1 Single Molecule Studies of Kinesin E157 Mutants

To further characterize the motility defects of kinesin E164 mutants, I introduced this mutation into a GFP-tagged human kinesin construct. In the human construct this residue corresponds to amino acid 157. As in the *Drosophila* construct, this residue is located close to the microtubule binding surface and is far from the nucleotide binding site (Figure 4.1A). I created two mutants, E157A and E157K, where I replaced the negatively charged glutamic acid with either a neutrally charged alanine or a positively charged lysine, respectively.

I used Total Internal Reflection Fluorescence (TIRF) microscopy to study the motility properties of single kinesin motors. Contrary to what was concluded from earlier studies of these kinesin mutants, I observed that these mutants were not stalled on the microtubule, but were in fact able to walk processively along microtubules (Figure 4.2A). While both wildtype and mutant motors were able to walk processively, there were differences in motility between these motors. I observed a reduction in run length of kinesin E157A and E157K mutant motors compared to wildtype motors (Figures 4.2B, A.11A, A.12A). While wildtype motors moved an average of 1.6 μm before dissociating from the microtubule, this was reduced to approximately 0.8 μm for both mutant motors. I observed a slight reduction in the total association time, or total time motors remained bound to the microtubule, of mutant motors compared to wildtype motors (Figures 4.2C, A.11B, A.12B). I saw that wildtype motors remained bound for an average of 3.6 sec, while E157A and E157K mutants remained bound for 2.5 sec and 2.8 sec, respectively. I also observed these mutant motors to move slower in comparison to wildtype motors (Figures 4.2D, A.11C, A.12C). Wildtype motors moved at an average rate of 0.45 μm/sec, while mutant motors both moved at approximately 0.31 μm/sec. Last, I observed that the percentage of wildtype motors that pause during a run was greater than that of both E157A and E157K mutant motors (Figure 4.2E). I saw that 26% of wildtype motors paused, whereas only 5% of E157A and 14% of E157K motors paused.

Here I demonstrate that while E157A and E157K kinesin motors exhibit shorter run lengths and slower velocities compared to wildtype motors, these mutants are still able to walk processively along the microtubule, taking up to 100 consecutive steps before dissociating.

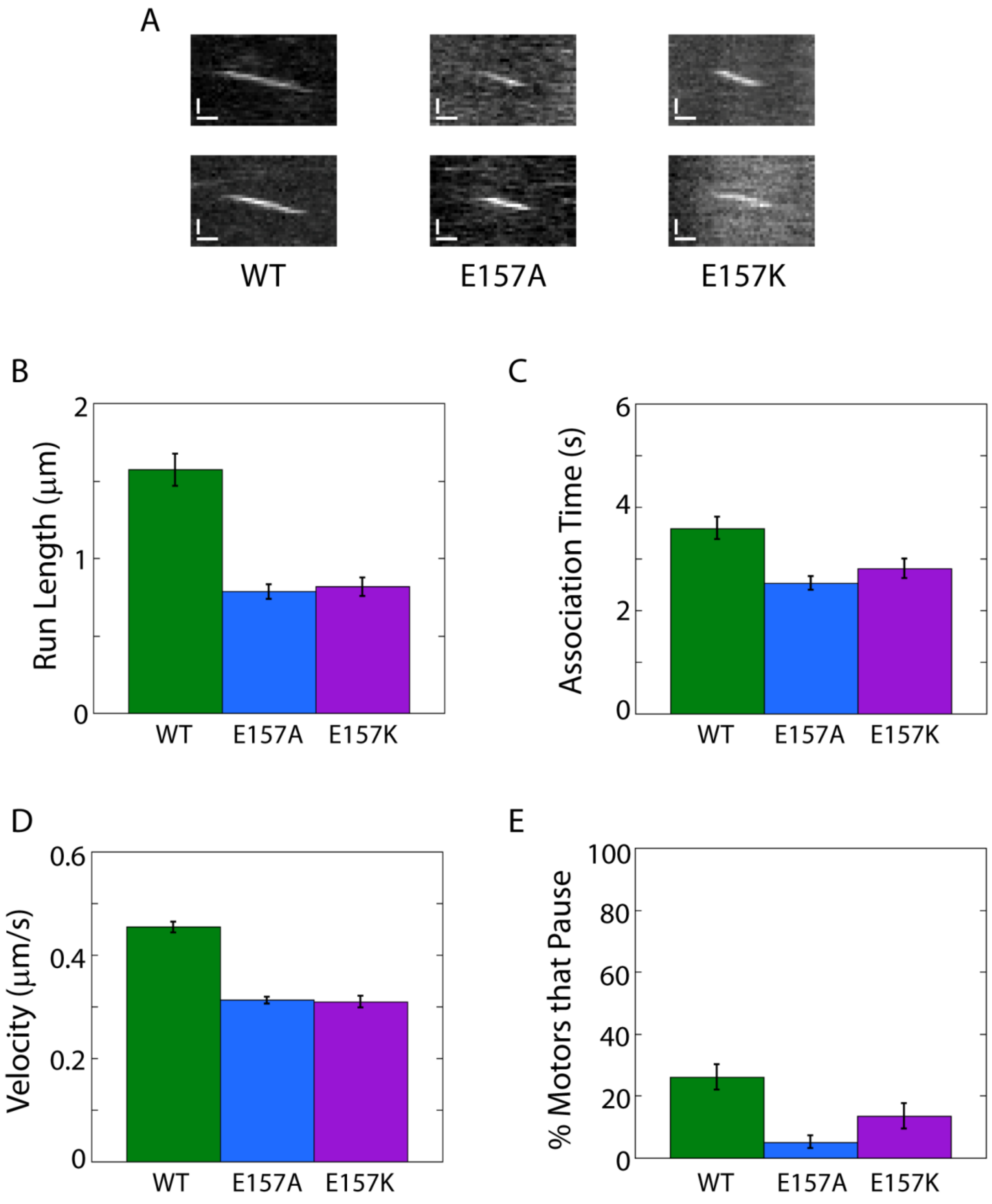

Figure 4.2 Single Molecule Studies of Mutant Kinesin Motors

A. Kymographs depicting single motor motility of wildtype and mutant kinesin motors. Horizontal scale bars are 0.5 μm. Vertical scale bars are 2.5 sec. **B.** Run length was measured as the total distance traveled by wildtype or mutant motors before dissociation. Error bars represent the standard error of the mean. **C.** Total association time was measured as the total time wildtype or mutant motors were associated with the microtubule during a run. Error bars represent the standard error of the mean. **D.** Moving velocity of wildtype and mutant motors. Error bars represent the standard error of the mean. **E.** Percentage of wildtype and mutant motors that pause at least once during their run. Error bars represent the standard error of proportion. **B-E.** For all plots, number of motors measured for WT, E157A, and E157K was 115, 117, and 74, respectively.

4.2.2 Multiple-Motor Studies of Kinesin E157 Mutants

I next examined how multiple mutant kinesin motors cooperate to transport cargo. I used the microtubule gliding assay, where kinesin motors are attached to the chamber surface such that their motor domains are oriented into the chamber. When microtubules are added in the presence of ATP, kinesin motors bind and propel these filaments though the chamber, which is observed as microtubule gliding. This assay is one method used to study multiple motor transport, as many kinesin motors work together to move a single microtubule.

I performed microtubule gliding assays on three different surface densities of wildtype or mutant kinesin motors (Figure 4.3A). With wildtype kinesin, I observed that microtubule gliding velocities increased as the surface density of kinesin decreased (Figure 4.3B). I observed a similar dependence of gliding velocity on the surface density of motors in assays with the E157A kinesin mutant. Despite this similar trend, the gliding velocities of microtubules in assays with the E157A kinesin mutant were reduced by a factor of approximately 1.4 for all three surface densities tested.

Interestingly, I did not observe a surface density dependence on the gliding velocity of microtubules in assays with the E157K mutants (Figure 4.3B). Gliding velocities did not increase as the surface density of motors decreased in this case, but rather remained relatively constant. Like the E157A kinesin mutant, microtubule gliding velocities in assays with E157K kinesin were reduced compared to wildtype. In assays with the highest motor density, gliding velocities with E157K kinesin were similar to those with E157A kinesin and were reduced by a factor of approximately 1.4 compared to wildtype. At the lowest surface density, gliding velocities with E157K kinesin were reduced more dramatically, by a factor of 5, compared to wildtype kinesin.

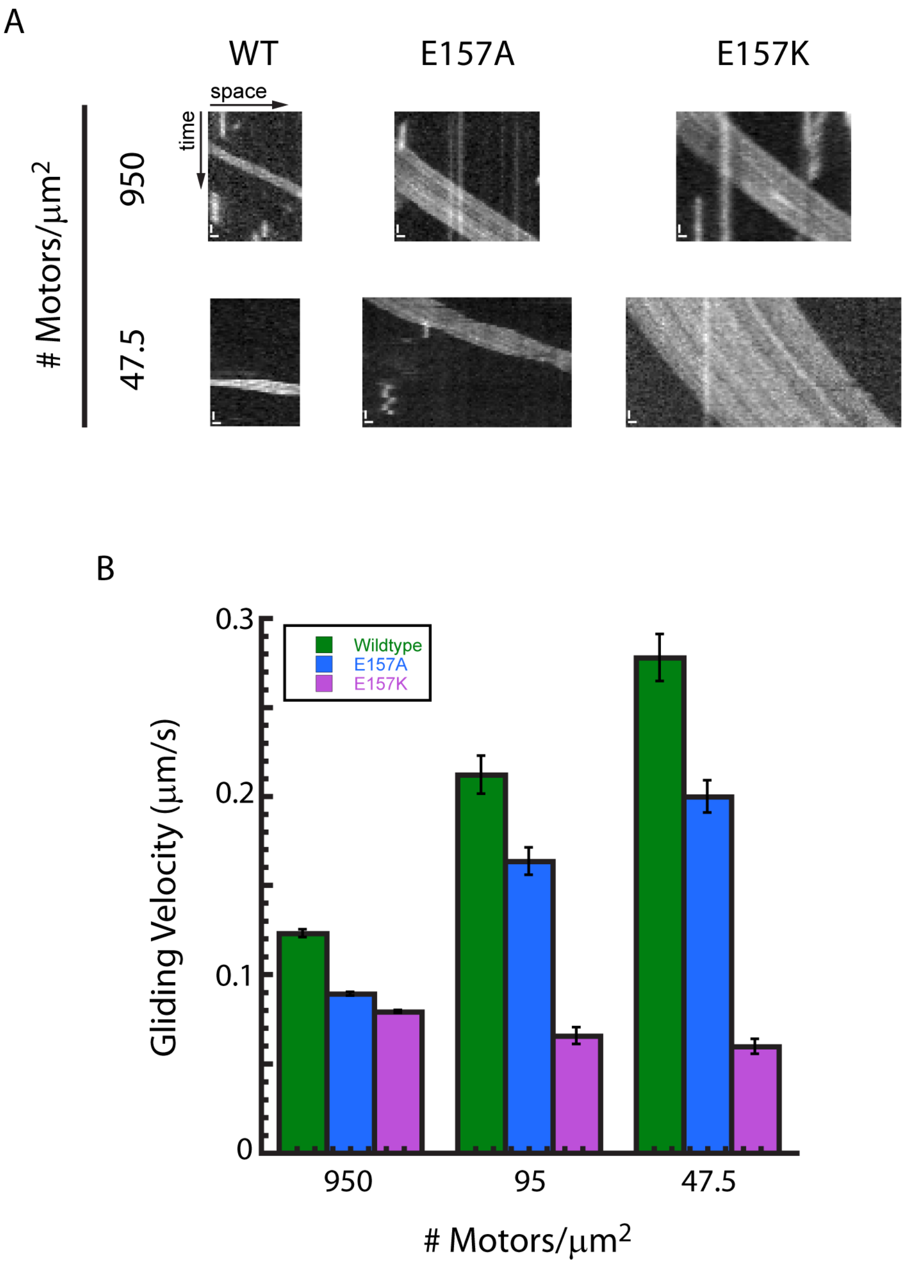

Figure 4.3 Multiple-Motor Gliding Assays with Wildtype and Mutant Kinesin Motors

A. Example kymographs of gliding assays with wildtype or mutant kinesin motors on different surface densities of motors. Horizontal scale bars are 1 µm. Vertical scale bars are 20 sec. **B.** Gliding velocities of microtubules on different surface densities of wildtype and mutant kinesin motors. Number of microtubules measured for WT, E157A, and E157K motors on 950 motors/µm^2, respectively: 60, 60, 60. For 95 motors/µm^2: 67, 60, 60. For 47.5 motors/µm^2: 51, 60, 67. Error bars represent standard error of the mean.

Here I show that in multiple motor gliding assays, E157A kinesin motors exhibit a similar reduction in velocity compared to wildtype motors as was observed in single molecule assays. With high motor densities, E157K mutants also show a similar reduction in velocity as was observed in single molecule assays. However, on lower motor surface densities, I see a greater reduction in velocity of microtubules propelled by E157K motors compared to wildtype motors.

4.3 Discussion

Drosophila possessing the kinesin E164K mutation exhibit severe transport defects, rendering this mutation lethal (Brendza et al., 1999; Djagaeva et al., 2012). Studies aimed at understanding how this mutation disrupts kinesin motility concluded that this mutation created a rigor kinesin that was unable to walk along microtubules (Klumpp et al., 2004; Klumpp et al., 2003). Such a mutation would understandably disrupt transport and lead to lethality. From the results presented here, I show that this mutant, while possessing motility defects, is not a rigor mutant. I show that both E157A and E157K kinesin mutants are able to take up to 100 steps before dissociating from the microtubule, and are therefore able to walk processively along microtubules. Knowing that these mutants are not truly rigor, I aimed to fully characterize these mutants to better understand the mechanism by which these mutants disrupt transport.

From single molecule studies, I observed that both E157A and E157K kinesin mutants exhibit slower velocities and shorter run lengths compared to wildtype kinesin motors. I observed that the velocity of mutants was reduced approximately 1.4-fold compared to wildtype motors. This decrease in velocity could be explained by a reduced ATP turnover rate, as was observed in previous studies of these mutants (Klumpp et al., 2004; Klumpp et al., 2003). The approximately 2-fold reduction in run length observed for both E157A and E157K mutants could be due to either a cooperativity defect between the two kinesin motor heads of a single dimer, or could be due to a decreased affinity of these mutant motors for microtubules. Previous work has suggested that in *Drosophila*, Glu^{164} could be involved in an electrostatic interaction with a positively charged residue on the other motor head at the dimer interface (Brendza et al., 1999). Such an interaction could mediate cooperativity between the two motor domains, disruption of which would likely lead to loss of coordination between the two heads, and thus a decrease in processivity. Alternatively, it should be noted that single molecule experiments with the E157K kinesin mutant required five times the amount of protein compared to wildtype kinesin in order to witness motility events. This suggests that the E157K mutant could have a decreased affinity for microtubules. Further studies are needed to directly measure the effect of this mutation on the binding affinity of E157K to microtubules, but such a decrease in affinity could also explain a decrease in motor processivity. Alternatively, there could be a high probability of these motors to bind, and quickly unbind microtubules due to cooperativity defects that disrupt coordination between the two heads, which could prevent motors from taking any steps. If these events were fast, it is possible that they would not be observed given the time resolution used in these studies to visualize GFP-tagged motors. I also observed that a lower percentage of mutant motors paused during a run compared to wildtype kinesin motors. This difference could be due to the shorter run lengths observed for mutant motors. If there is a probability that a motor will pause during a run, motors that move shorter distances will have a lower probability of pausing.

I showed that when the negatively charged Glu^{157} was mutated to either a neutral charge or a positive charge, both mutants exhibited similar behavior in single molecule assays. This suggests that the observed differences in the single molecule motility of these mutants is due to the loss of a negative charge at this particular residue.

In microtubule gliding assays, many motors work together to transport a single filament. I observed a velocity dependence on the surface density of kinesin motors for assays with both wildtype and E157A kinesin. I showed that for these motors, microtubule gliding velocities increased as the surface density of motors decreased. This has been observed previously for wildtype motors and is thought to be due to negative interference which occurs when high densities of motors transport a single microtubule (Bohm et al., 2000). While I saw a similar trend in that velocity increased as the surface density of motors decreased for both wildtype and E157A motors, I observed a reduced gliding velocity for E157A motors in comparison to wildtype motors. Across all surface densities tested, there was an approximately 1.4-fold decrease in motor velocity of E157A motors compared to wildtype. This decrease was similar to the decrease observed in single motor assays.

Interestingly, I did not see a velocity dependence on surface density in the case of E157K mutants. Rather, gliding velocities were relatively constant on all E157K kinesin surface densities. On the highest motor surface density (950 motors/μm^2), gliding velocities were similar to those of E157A and were reduced 1.4-fold compared to wildtype motors. Again, this was similar to the decrease in velocity observed in single motor studies. However, as the surface density of motors was decreased, there was a further fold reduction in velocity of E157K motors compared to wildtype motors. On the lowest motor density (47.5 motors/μm^2), I showed that E157K gliding velocities were reduced by a factor of 5 compared to wildtype velocities. On these lower surface densities, I am eliminating the effects of negative interference that occurs on crowded surfaces and am better probing the cooperative nature between motors transporting a single filament. The fact that E157K gliding velocities do not increase as this negative interference is relieved suggests that these motors could have a defect in their ability to cooperate with other motors to transport a single cargo, as such a large reduction in velocity was not observed in the case of single molecule assays.

An alternative explanation as to why I observe such large reductions in gliding velocities with E157K mutant motors could be explained if only a small percentage of these mutant motors successfully bind and walk along microtubules, while the majority bind and release without stepping. Unlike in single molecule assays, motors in gliding assays are all bound to the surface and I am forced to observe the effect of all motor interactions with microtubule. Events where kinesin motors bind briefly and release without taking any steps would slow the overall gliding velocity of filaments. This type of drag would not be relieved upon diluting the surface density of motors if there is a certain percentage of binding events that do not produce productive motion of filaments. Thus, this could be another explanation for the large reduction in gliding velocities observed with E157K mutants.

These studies provide insight into the behavior of single E157A and E157K kinesin mutants as well as how multiple motors cooperate to transport a single cargo. I show that while both mutants exhibit reduced velocities and run lengths compared to wildtype motors in single motor assays, they are still processive and able to move up to 0.8 μm along a microtubule before dissociating. Multiple motor gliding assays suggest that E157K mutants could possess a defect in their ability to work cooperativity with multiple motors. Alternatively, these motors could be defective in their ability to bind and walk along microtubules, with a high percentage of binding events resulting in release from microtubules without any stepping. Here, I show that transport defects observed in vivo with these mutant motors are not a result of these mutants binding in a rigor state to microtubules. I show that these mutants are able to disrupt motility either through a defect in cooperativity between multiple motors transporting a single cargo or through an inability to productively bind and walk along microtubules.

4.4 Methods

4.4.1 Constructs. A human kinesin-1 construct truncated at amino acid 560 fused to a C-terminal GFP tag and a 6X His Tag was used. E157A and E157K kinesin mutants were generated using site-directed mutagenesis. Mutants were verified by sequencing.

4.4.2 Protein Purification. Wildtype and mutant kinesin constructs were expressed using a pET17b expression vector. Expression with IPTG and affinity purification with Nickel beads (Qiagen) were carried out as described previously (Pierce and Vale, 1998). GFP-kinesin concentration was quantified by comparison to known BSA standards on a Coomassie-stained SDS-PAGE gel.

4.4.3 Microtubule Preparation. Rhodamine labeled microtubules were prepared using a 1:13.5 ratio of labeled:unlabeled tubulin. Rhodamine labeled tubulin was purchased from Cytoskeleton, Inc. Unlabeled tubulin was purified from porcine brain as described previously (Peloquin et al., 2005). To prepare microtubules, both unlabeled and rhodamine labeled tubulin were brought to 5 mg/mL in PEM-100 (100 mM K-Pipes, pH 6.8, 2 mM $MgSO_4$, 2 mM EGTA) and incubated for 10 minutes on ice. Tubulin was centrifuged at 4^oC for 10 minutes at 100,000 xg to remove tubulin aggregates. The remaining tubulin in the supernatant was mixed with 1 mM GTP and polymerized at 37^oC for 20 minutes. 50 μM Taxol was added to stabilize polymerized microtubules, followed by another 20 minute incubation at 37^oC. Polymerized microtubules were centrifuged at

25°C for 10 minutes at 14,000 x g to separate unincorporated tubulin. The microtubule pellet was resuspended in 50 μL PEM-100 with 40 μM Taxol.

4.4.4 Single Molecule Assays. Assays were carried out in 10 μL flow chambers made of a glass slide attached to a cover slip with double-stick tape. Prior to use, cover slips were biologically cleaned and treated with dimethyldichlorosilane solution, 2% w/v (GE Healthcare). Flow chambers were first incubated with 2% anti-tubulin antibody in PEM-100 for 5 minutes to attach microtubules, followed by a 5 minute incubation with 5% Pluronic F-127 (Sigma) in PEM-100 to block the surface. Rhodamine-labeled microtubules (0.05 mg/mL microtubules, 20 μM Taxol in PEM-100) were allowed to bind for 10 minutes. Excess microtubules were removed with a wash step (10 mM DTT, 20 μM Taxol in PEM-100). Finally, motility mix was added to the chamber (1 nM WT or E157A kinesin; or 5 nM E157K kinesin, 0.05% Pluronic F-127, 25 μM Taxol, 0.25 mg/mL BSA, 50 mM DTT, 0.5 mM ATP, 15 mg/mL glucose, 0.5 mg/mL glucose oxidase, 0.15 mg/mL catalase in PEM-100).

4.4.5 Gliding Assays. Assays were carried out in 10 μL flow chambers made of a glass slide attached to a cover slip with double-stick tape. Flow chambers were first incubated with kinesin for five minutes, followed by a chamber wash (5 mg/mL BSA, 120 μM Taxol, 40 mM DTT in PEM-100). Rhodamine-labeled microtubules (0.05 mg/mL microtubules, 20 μM Taxol in PEM-100) were then allowed to bind for 2 minutes. Finally, motility mix was added to the chamber (50 μM Taxol, 50 mM DTT, 1 mM ATP, 15 mg/mL glucose, 0.5 mg/mL glucose oxidase, 0.15 mg/mL catalase in PEM-100).

4.4.6 Imaging. For single molecule assays, an image of the microtubules was acquired using epi-fluorescence prior to imaging single GFP-kinesin motors. Two minute recordings of GFP-kinesin motility were taken with a 500 ms exposure time using Total Internal Reflection Fluorescence (TIRF) microscopy with 50 mW 488 Cyan laser

(Spectra-Physics) illumination built around an inverted Nikon Ti-E microscope (Nikon). The microscope uses a 60x 1.49 NA objective and images were collected using an electron multiplier CCD camera (Cascade II, Roper Scientifics) after a 4x beam expander. The final pixel size was 67.5 nm. Images were acquired with no delay and saved as nd2 files and exported as 16-bit tif files. For gliding assays, rhodamine-labeled microtubules were imaged using epi-fluorescence. Microtubules were imaged with a 500 ms exposure, every 10 seconds for a total duration of 5 minutes. Imaging was performed with a Nikon Ti-E microscope using a 60x 1.49 NA objective. Images were collected using an electron multiplier CCD camera (Cascade II, Roper Scientifics). The final pixel size was 270 nm. Images were saved as nd2 files and exported as 16-bit tif files.

4.4.7 Data Analysis. Single molecule motility was analyzed using kymographs generated by the ImageJ plugin, MultipleKymograph. For velocity measurements, the moving velocity was calculated by measuring only moving segments of runs, thereby excluding any pauses from the measurement. Gliding velocities were measured using the ImageJ plugin, MtrackJ (Meijering et al., 2012).

CHAPTER 5

CONCLUSIONS AND FUTURE DIRECTIONS

5.1 Summary

Motor proteins must transport cargos over long distances along microtubule tracks to mediate the widespread distribution of cargos throughout cells. These microtubule tracks form complex architectures and are crowded with microtubule-associated proteins and other motor proteins. How motors navigate these complex tracks to ensure efficient transport of cargos is unclear. An understanding of the mechanisms by which motors navigate complex cytoskeletal tracks is imperative for a more detailed understanding of intracellular transport, a process that has many implications for neurodegenerative disease.

In this dissertation, I have used in vitro assays to reconstitute kinesin motor motility using purified components. The most basic of these assays uses wildtype motors on microtubules polymerized from purified tubulin subunits, stripped of any associated microtubule-associated proteins and motors. Using this system, I have systematically studied how motors navigate microtubule tracks with specific complexities added. Specifically, I have discussed how motor traffic, microtubule bundle architecture, and motor domain mutations affect the transport properties of kinesin-1, as well as mechanisms used by kinesin-1 to help efficiently navigate these complex tracks.

5.1.1 Transport of Self-Assembled Qdot Cargos

I first studied how the transport of single kinesin motors and cargos transported by kinesin motors was affected by traffic along the microtubule. In these experiments, I added excess motile kinesin motors to microtubules to create traffic along these tracks. I was able to show that the quantum dot (Qdot) cargos used in this system were able to form non-specific attachments to motors along the track. Such a system where cargo-motor complexes can self-assemble dynamically resembles a proposed mechanism for the transport of proteinaceous cargos in slow axonal transport (Scott et al., 2011).

I showed that in the case of both single kinesin motors and cargos transported by multiple kinesin motors, transport was slowed in the presence of motor traffic along the microtubule. Interestingly, I found that while this traffic caused a severe reduction in processivity of single motors, cargo processivity actually increased due to the ability of cargos to form non-specific attachments to motors along the microtubule, enabling their transport by multiple motors. In addition, I showed that while cargos paused more frequently as traffic was increased, the duration of these pauses actually decreased in more crowded conditions. I suggest that on microtubules with higher crowding, Qdot cargos are able to more readily associate motors on adjacent protofilaments. I speculate that this would allow a cargo to switch protofilament tracks to circumvent an obstacle that would normally result in a longer pause duration. I also observed reversals of cargo motion on crowded microtubules. I attribute these reversals to cargos with multiple motors bound. If the system is under strain and a front motor detaches, cargo reversals would be observed as the Qdot cargo rocks backward and repositions itself over the remaining motors engaged with the microtubule.

These studies provide insights into how cargo motility is maintained on microtubules crowded with motors. In these circumstances, transport of cargos by multiple motors is essential. I show that cargos actually take advantage of these crowded conditions to help successfully navigate these same crowded tracks. The crowded conditions enable cargos to bind and exchange motors easily, allowing cargos to be transported further and navigate around obstacles by attaching to motors on neighboring tracks.

5.1.2 Motor Transport on Bundled Microtubules

I next studied how the architecture of microtubule tracks affects kinesin motility. I prepared three types of microtubule bundles: 1) tightly packed bundles with randomly oriented microtubules formed by depletion forces in the presence of PEG, 2) antiparallel bundles formed by MAP65, with a 25 nm interspacing between filaments, and 3) endogenous parallel microtubule bundles from neuronal-like processes of differentiated CAD cells. These different bundle types allowed for the understanding of how the spacing between microtubules and the orientation of microtubules within a bundle affect motility.

In cells, MAPs generate microtubule bundles with spacing between filaments within the bundle. I show that this spacing is essential for motor motility. On tightly packed microtubule bundles formed in the presence of PEG, I saw that kinesin motility was reduced, as motors exhibited shorter run lengths and slower velocities on PEG bundles compared to single microtubules in the presence of PEG. I did not observe a reduction in processivity or velocity in the case of MAP65 bundles. While I did observe a reduction in velocity on CAD cell bundles, I did not observe a reduction in processivity. This reduction in velocity is likely attributed to MAPs on these cellular bundles that I could not control for in my single microtubule assay, and not an effect of the bundle architecture. This data suggests that the spacing between microtubules is essential for organizing the microtubule bundle and preventing staggered, overlapping microtubules within the bundle from acting as obstacles for kinesin motors.

In the case of microtubule bundles that possess oppositely oriented microtubules (PEG and MAP65 bundles), I observed motors that switch direction during a run. I believe that these reversals in direction are due to motors switching to an adjacent, oppositely oriented microtubule track. This is supported by the fact that I did not observe these reversals in the case of CAD cell bundles, where all microtubules are oriented in the same direction. I showed that the ability of motors to switch to adjacent microtubule tracks within a bundle enhances the processivity of kinesin motors. For example, in the case of PEG bundles that reduce motor motility, I showed that motors that were able to switch microtubule tracks recovered processivity, and had run lengths similar to motors on single microtubules with PEG. However, motors that did not reverse exhibit reduced run lengths compared to motors on single microtubules with PEG. Thus, this ability to switch microtubule tracks may be a mechanism by which kinesin motors use to avoid obstacles along their path.

5.1.3 Kinesin Motor Domain Mutants

Lastly, I probed how specific mutations within the kinesin motor domain affect motor transport. I mutated amino acid 157 in the human kinesin heavy chain, changing this negatively charged glutamic acid to either a positively charged lysine (E157K) or a neutrally charged alanine residue (E157A). This residue is positioned close to the microtubule binding face of the motor domain, and has been demonstrated to disrupt transport in vivo (Brendza et al., 1999; Djagaeva et al., 2012). I aimed to understand the mechanism behind these observed transport defects.

With single molecule studies, I showed that these mutant motors behaved similar to each other in that both E157A and E157K mutants exhibited a reduction in run length and velocity. Interestingly, I found that in multiple motor gliding assays, these mutants behaved differently. I carried these assays out on three different surface densities of kinesin motors. In the case of wildtype motors, I observed that gliding velocity was increased as the surface density was decreased, indicating that there is negative interference between motors on dense surfaces. For E157A mutants, I observed a similar increase in velocity as the surface density of motors was decreased. As expected, for all surface densities, I observed a decrease in the velocity of gliding filaments compared to assays with wildtype motors. This decrease was proportional to the decrease in velocity observed in single molecule assays. I saw a similar decrease in gliding velocity with E157K motors compared to wildtype motors on high densities of motors. However, in the case of E157K motors, I did not observe an increase in the gliding velocity as the surface density of motors was decreased. The gliding velocities remained relatively constant across all surface densities of E157K motors. Thus, for low surface densities of E157K motors, I observed an even greater-fold reduction in the E157K gliding velocities compared to wildtype motors.

This behavior suggests that E157K motors could possess a defect that affects their ability to work cooperatively with multiple motors to transport a single filament. An alternative interpretation of this data can be made based on my observation that there were fewer motility events observed in single molecule assays with E157K motors compared to assays with identical concentrations of wildtype or E157A motors. This low number of motility events could be due to a high probability of E157K motors to bind microtubules and quickly release without stepping, which could be caused by a lack of coordination between two motor heads within a dimer. It is possible that such events would not be observed with the time resolution used in these studies. Motors with a high probability of binding but not stepping would act to create drag in a microtubule gliding assay, and could provide another explanation for the behavior of E157K motors in these multiple motor gliding assays. This work provides new insights into the mechanism by which these kinesin mutants could cause transport defects in vivo.

5.2 Future Directions

Using the system where I crowded microtubules with excess motors to probe the effect on single motor and cargo motility, I showed that cargos were able to form non-specific attachments with motors along the microtubule. I believe that at high crowding along the microtubule, cargos are able to readily associate motors on adjacent protofilaments, allowing them to navigate around obstacles. In the case of these experiments, obstacles encountered were slow moving motors, generated by traffic along the microtubule. Further studies using non-motile obstacles, such as a rigor kinesin or the MAP, tau, would be interesting to probe the mechanism by which self-assembled cargos are able to navigate around stationary obstacles on microtubules crowded with excess motors. Using a rigor kinesin, a mutant that binds microtubules tightly and does not release, would allow for the direct comparison of how self-assembled cargos are able to navigate around moving versus stationary obstacles. Using the MAP, tau, would enable the study of the extent to which these self-assembled cargos are able to navigate around obstacles that could exist in neurodegenerative disease states. Aggregates of tau along microtubules is a hallmark of neurodegenerative diseases, such as Alzheimer’s Disease (Ackmann et al., 2000). These aggregates can be generated in vitro by adding high concentrations of tau to assays. Unlike kinesin obstacles which bind to a single protofilament on the microtubule, these tau aggregates are likely to simultaneously block many adjacent protofilaments. Thus, these would pose as a very different obstacle than rigor kinesin mutants, and would require cargos to associate new motors on multiple adjacent protofilaments to allow it to navigate around such a large obstacle. Addition of these different types of non-motile obstacles to my assay would allow for a better understanding of how, and whether, self-assembled cargos are able to ensure proper transport along microtubules in the case of healthy cells versus diseased cells exhibiting signs of neurodegeneration.

Another interesting avenue to pursue would be to study how cargoes with multiple motors are transported along microtubule bundles. Here I have studied how single motors navigate these complex microtubule architectures. In cells however, transport is more complex, as cargos are often carried by multiple motors. The study of cargos transported by multiple kinesin motors or cargos transported by multiple species of motors would be interesting as these are representative of cargos transported in vivo. Specifically, it would be interesting to study how a cargo complexed to many motors of a single species is transported on bundles with antiparallel microtubules. Cargos that are 1 μm in diameter would span over many different microtubule tracks within a bundle. Assuming these cargos have motors distributed randomly on their surface, they would likely have motors simultaneously interacting with many different filaments within the bundle. On bundles with antiparallel microtubules, this would be interesting as there could be motors of the same species pulling in opposite directions on the cargo. This would resemble a tug-of-war, which is typically only thought of when two different motor species (i.e. Kinesin and Dynein) pull on the cargo in opposite directions. In dendrites, microtubule bundles are comprised of randomly oriented microtubules. Therefore, these bundles are likely to possess microtubules that are oriented antiparallel to one another. These studies could provide insights into how cargos are transported over long distances in dendrites.

In studies with E157K mutant motors, I have shown that there is a further reduction in microtubule gliding velocities compared to velocities observed in single molecule assays. This suggests that the defects in transport with these mutants is further exacerbated in multiple motor assays, and could explain the severe defects in transport observed in vivo. I have provided two hypotheses for the mechanism by which E157K mutant kinesin motors disrupt the transport of cargos in vivo. One mechanism is that these mutants are defective in their ability to cooperate with other motors to transport a single cargo. A second mechanism could be that these mutants are unable to properly coordinate between heads within a single dimer, resulting in many motors that bind and fall off before taking any steps.

In gliding assays, there are many motors that function to transport a single microtubule. This assay is messy in that the number of motors transporting microtubules is unknown as not all motors bound to the coverslip could be oriented in such a way to be capable of producing effective steps. Studies of cargos with just a few motors attached could provide further insight into whether and how these motors are defective in cooperative transport. New studies have shown that protein and DNA scaffolds can be used to link known numbers of motors to a single cargo (Derr et al., 2012; Diehl et al., 2006; Furuta et al., 2013). This tool could be used here to better understand how the number of motors bound to a cargo affects transport.

Studies of E157K mutants with higher temporal resolution could help probe whether there is a large probability that motors bind microtubules without taking any productive steps. In the studies presented here, mutants were tagged with GFP and a 500 ms exposure time was required to image motors. This time resolution would not allow for the visualization of events where motors bind and quickly unbind without taking any steps. Tagging these mutant motors with quantum dots would allow for imaging with much faster acquisition times, and would potentially allow for the visualization of such events if they are occurring.

The studies presented in this dissertation address how motors carry out transport on complex microtubule tracks, as well as how specific residues in the kinesin motor domain contribute to the efficient transport of cargos on these tracks. The suggested studies here would further build on the current understanding of how motors navigate the crowded, complex tracks that exist in the cell.

APPENDIX A

DISTRIBUTIONS OF SINGLE MOLECULE DATA

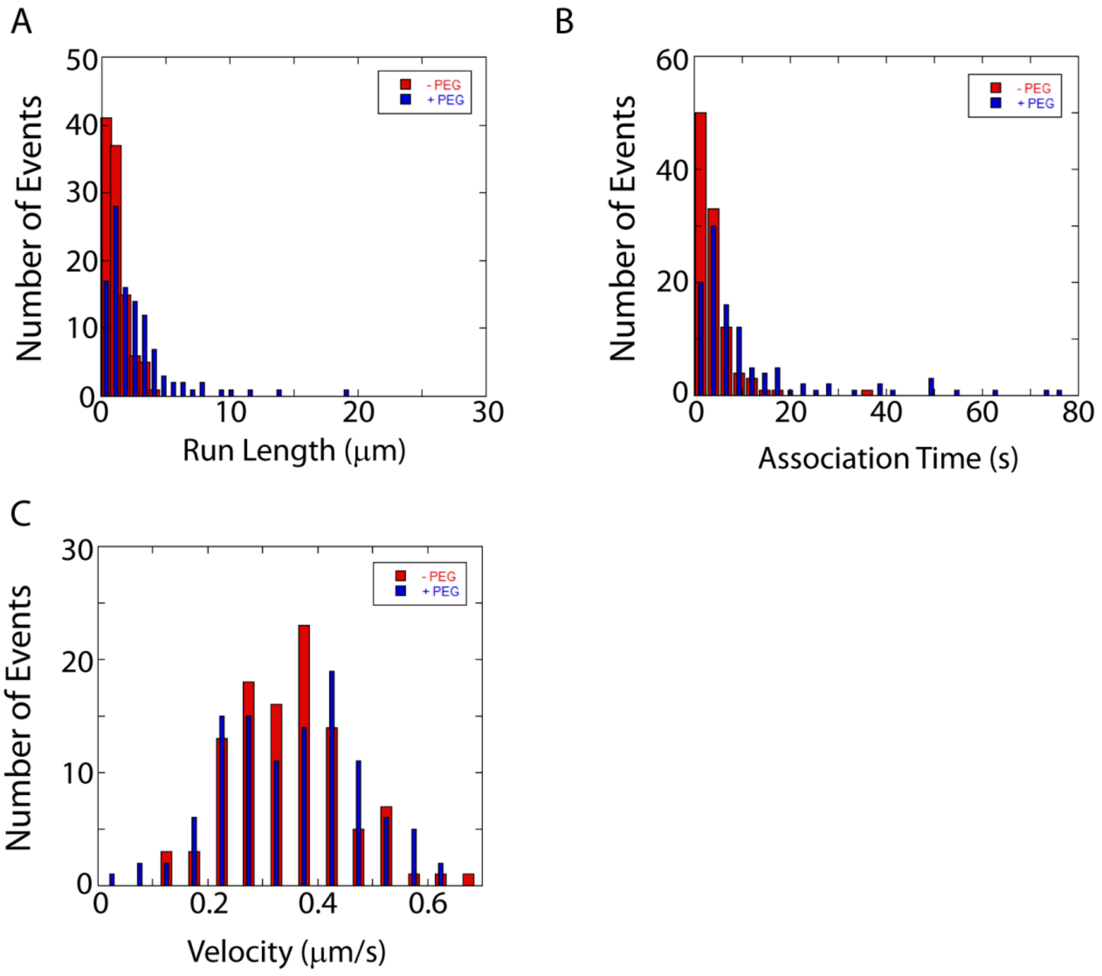

Figure A.1 Kinesin Motility on Single Microtubules in the Presence of PEG: Histograms

A. Distributions of run length measurements of motors on single microtubules in the absence (red bars) and presence of PEG (blue bars). **B.** Distributions of association time measurements of motors on single microtubules in the absence and presence of PEG. **C.** Distributions of moving velocity measurements of motors on microtubules in the absence and presence of PEG. **A-C.** For data taken in the absence of PEG, N = 105. For data taken in the presence of PEG, N = 109.

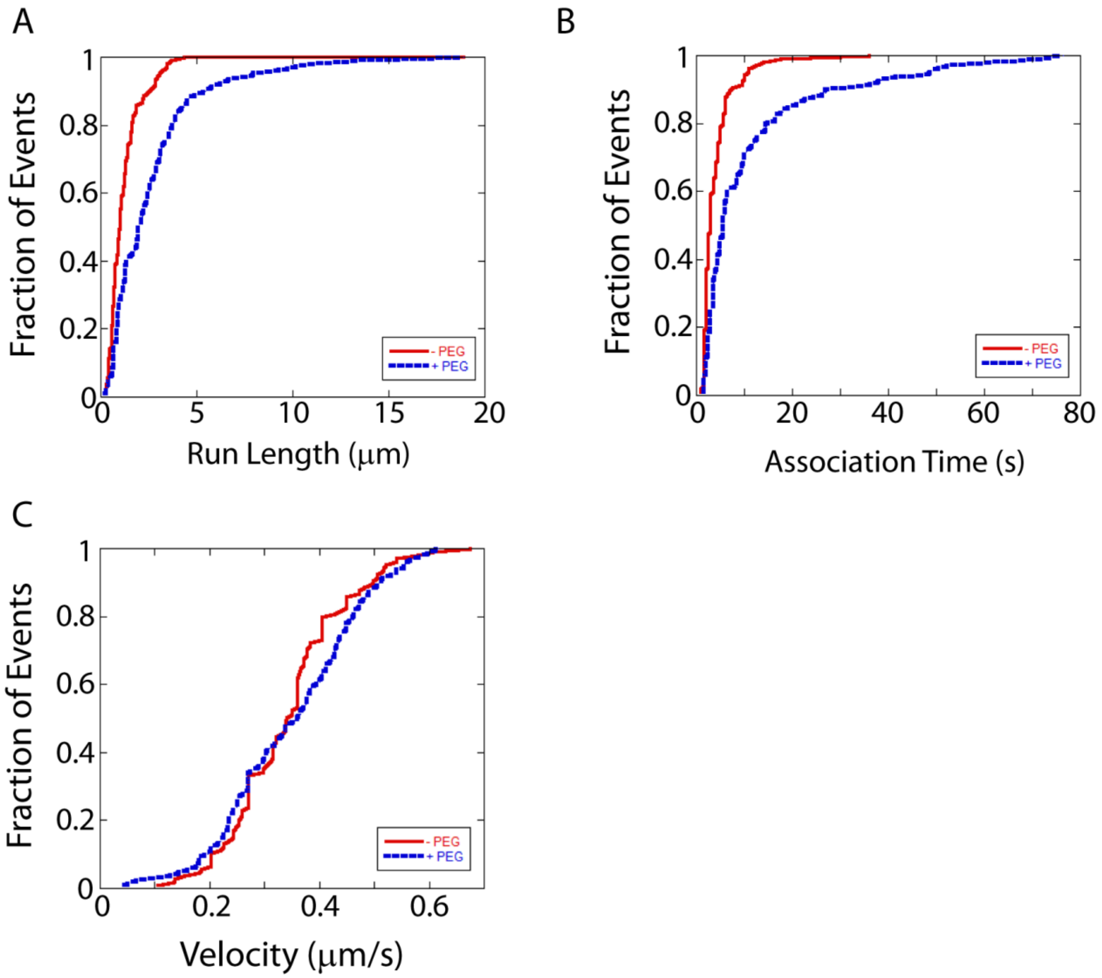

Figure A.2 Kinesin Motility on Single Microtubules in the Presence of PEG: Cumulative Probability Distributions

A. Cumulative probability distributions of run length measurements of motors on single microtubules in the absence (red) and presence of PEG (blue). **B.** Cumulative probability distributions of association time measurements of motors on single microtubules in the absence and presence of PEG. **C.** Cumulative probability distributions of moving velocity measurements of motors on microtubules in the absence and presence of PEG. **A-C.** For data taken in the absence of PEG, N = 105. For data taken in the presence of PEG, N = 109.

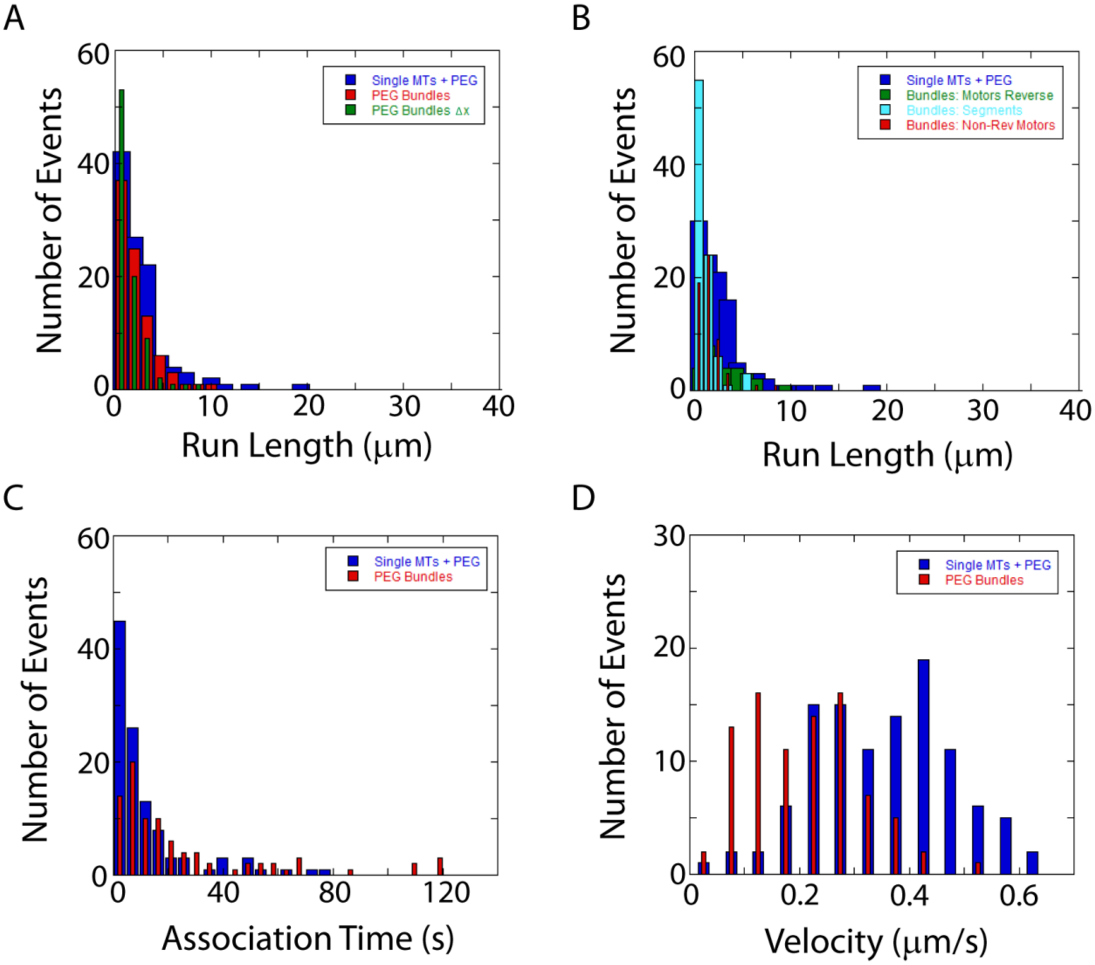

Figure A.3 Kinesin Motility on PEG Bundles: Histograms

A. Distributions of total run length measurements of motors on single MTs + PEG (blue bars) and PEG Bundles (red bars); and the final distance traveled (Δx) for motors on PEG bundles (green bars). **B.** Distributions of run length measurements of motors on single microtubules + PEG (blue bars), of motors that reverse direction on PEG bundles (green bars) and motors that do not reverse direction on PEG bundles (cyan bars). In addition, the average distance traveled before or after reversing direction on PEG bundles was measured (segments, red bars). **C.** Distributions of association time measurements of motors on single microtubules + PEG (blue bars) and on PEG bundles (red bars). **D.** Distributions of moving velocity measurements of motors on single microtubules with PEG (blue bars) and PEG bundles (red bars). **A-D.** For single microtubules with PEG, N = 109; for PEG bundles, N = 87; for motors that reverse on PEG bundles, N = 30; for motors that do not reverse on PEG bundles, N = 57.

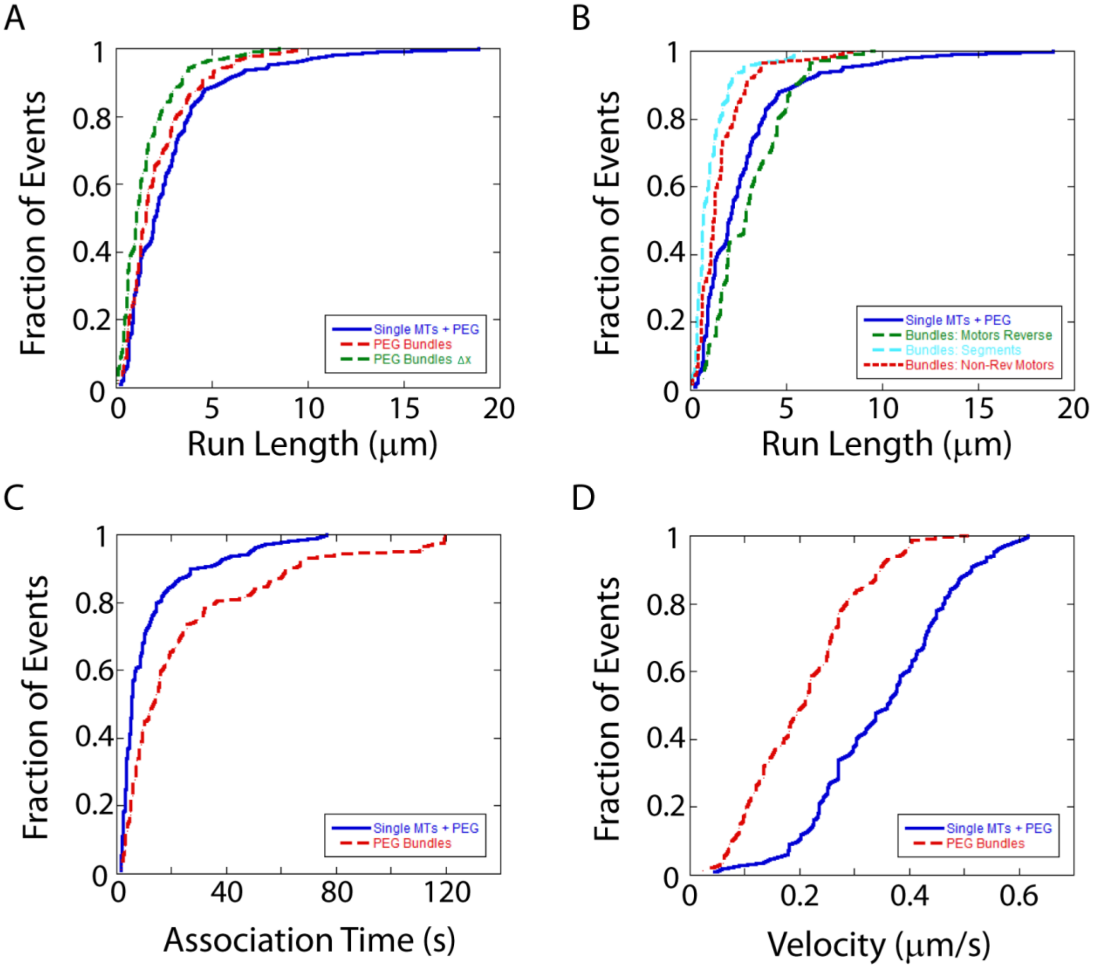

Figure A.4 Kinesin Motility on PEG Bundles: Cumulative Probability Distributions

A. Cumulative probability distributions of total run length measurements of motors on single MTs + PEG (blue) and PEG Bundles (red); and the final distance traveled (Δx) for motors on PEG bundles (green). **B.** Cumulative probability distributions of run length measurements of motors on single microtubules + PEG (blue), of motors that reverse direction on PEG bundles (green) and motors that do not reverse direction on PEG bundles (cyan). In addition, the average distance traveled before or after reversing direction on PEG bundles was measured (segments, red). **C.** Cumulative probability distributions of association time measurements of motors on single microtubules + PEG (blue) and on PEG bundles (red). **D.** Cumulative probability distributions of moving velocity measurements of motors on single microtubules with PEG (blue) and PEG bundles (red). **A-D.** For single microtubules with PEG, N = 109; for PEG bundles, N = 87; for motors that reverse on PEG bundles, N = 30; for motors that do not reverse on PEG bundles, N = 57.

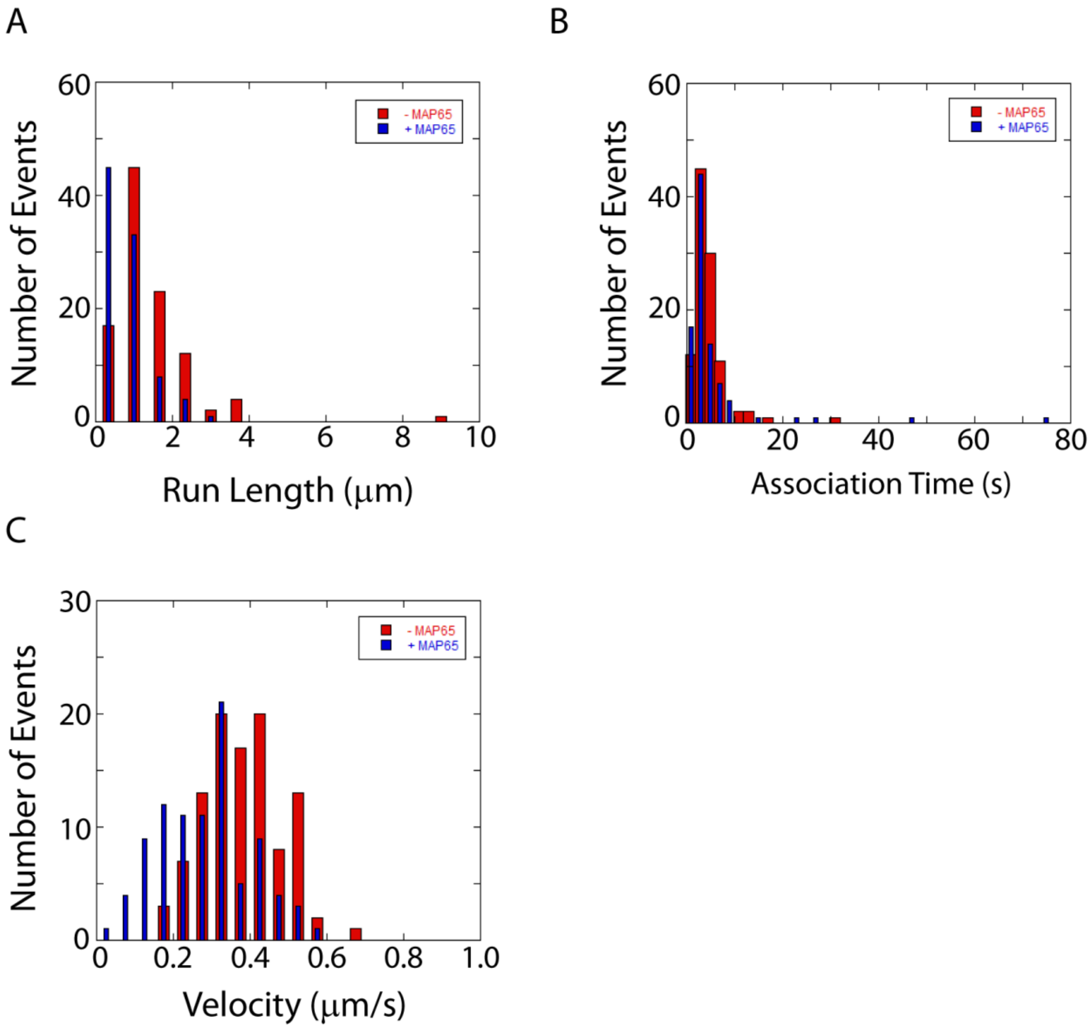

Figure A.5 Kinesin Motility on Single Microtubules in the Presence of MAP65: Histograms

A. Distributions of run length measurements of motors on microtubules in the absence (red bars) and presence (blue bars) of MAP65. **B.** Distributions of association time measurements of motors on microtubules in the absence and presence of MAP65. **C.** Distributions of moving velocity measurements of motors on microtubules in the absence and presence of MAP65. **A-C.** For data taken in the absence of MAP65, N = 104. For data taken in the presence of MAP65, N = 91.

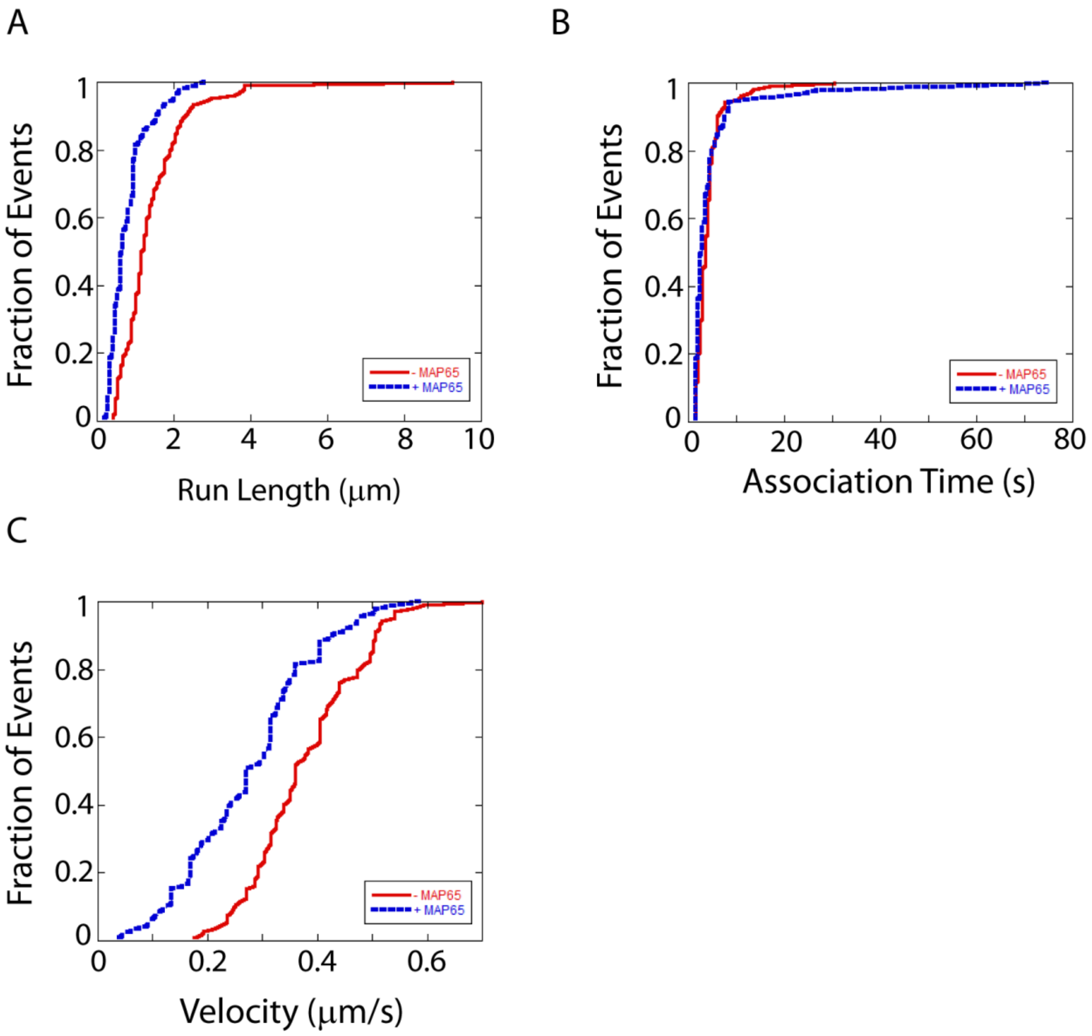

Figure A.6 Kinesin Motility on Single Microtubules in the Presence of MAP65: Cumulative Probability Distributions

A. Cumulative probability distributions of run length measurements of motors on microtubules in the absence (red) and presence (blue) of MAP65. **B.** Cumulative probability distributions of association time measurements of motors on microtubules in the absence and presence of MAP65. **C.** Cumulative probability distributions of moving velocity measurements of motors on microtubules in the absence and presence of MAP65. **A-C.** For data taken in the absence of MAP65, N = 104. For data taken in the presence of MAP65, N = 91.

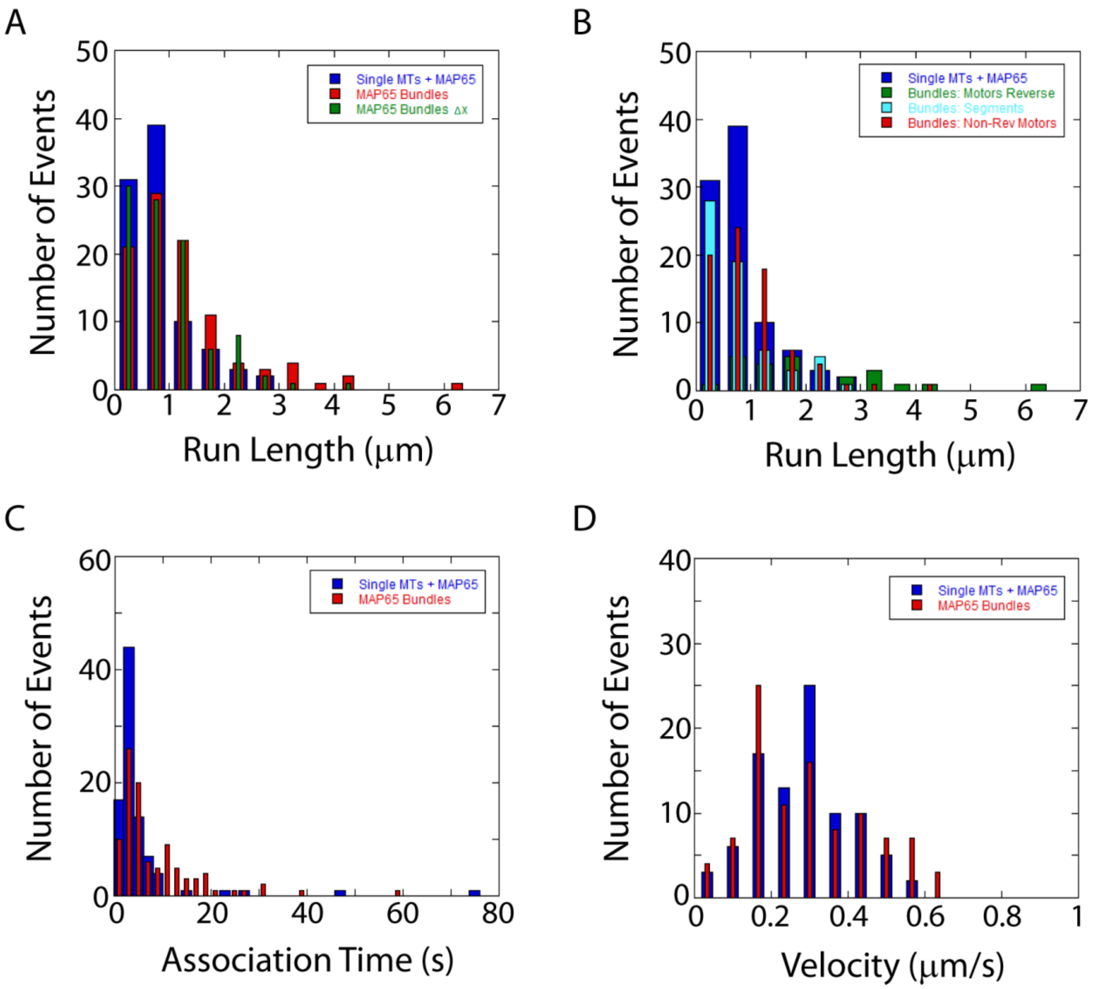

Figure A.7 Kinesin Motility on MAP65 Bundles: Histograms

A. Distributions of run length measurements of motors on single MTs + MAP65 (blue bars) and MAP65 bundles (red bars); and the final distance traveled (Δx) for motors on MAP65 bundles (green bars). **B.** Distributions of run length measurements of motors on single microtubules with MAP65 (blue bars), of motors that reverse direction on MAP65 bundles (green bars), motors that do not reverse direction on MAP65 bundles (red bars). In addition, the average distance traveled before or after reversing direction on MAP65 bundles was measured (segments, cyan bars). **C.** Distributions of association time measurements of motors on single microtubules with MAP65 (blue bars) and MAP65 bundles (red bars). **D.** Distributions of moving velocity measurements of motors on single microtubules with MAP65 (blue bars) and MAP65 bundles (red bars). **A-D.** For single microtubules with MAP65, N = 91; for MAP65 bundles, N = 98, for motors that reverse on MAP65 bundles, N = 23; for motors that do not reverse on MAP65 bundles, N = 75.

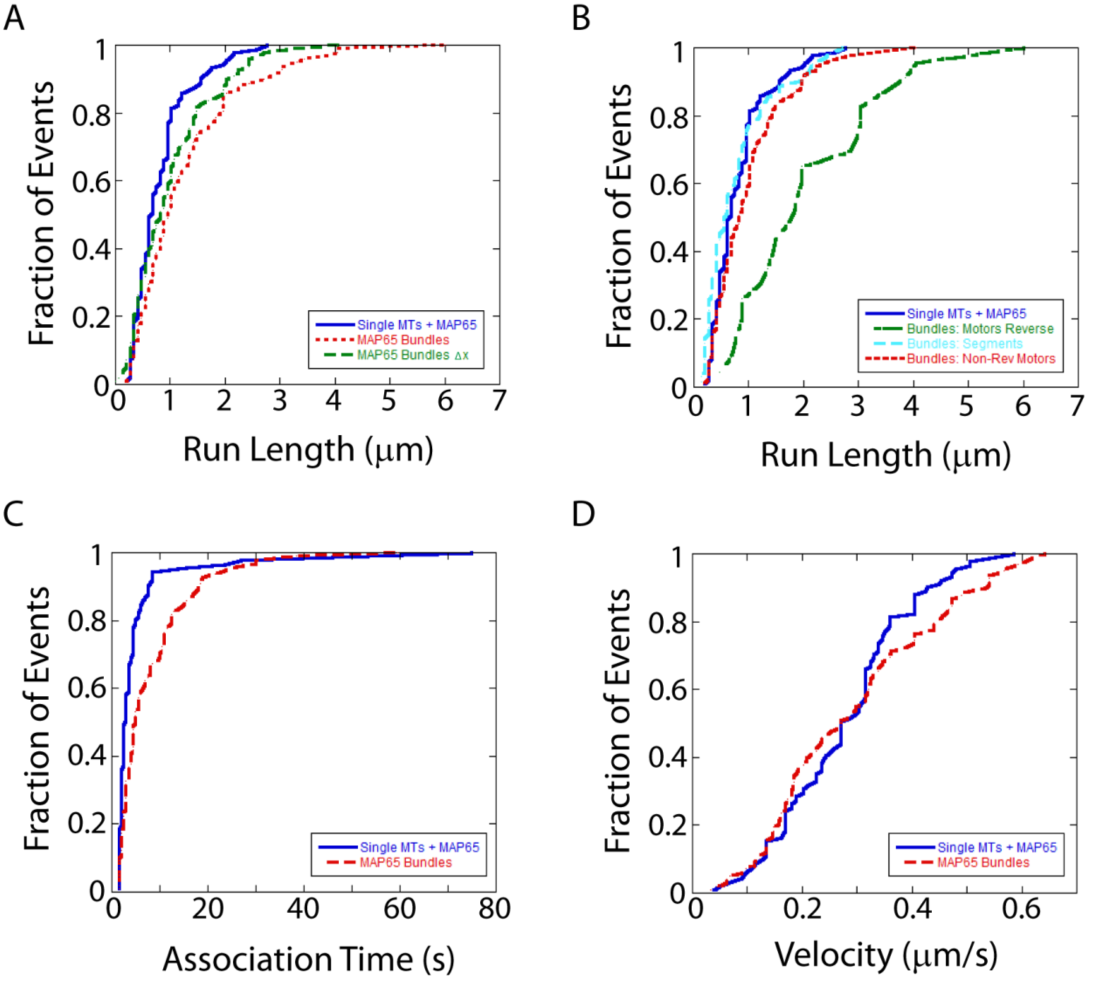

Figure A.8 Kinesin Motility on MAP65 Bundles: Cumulative Probability Distributions

A. Cumulative probability distributions of run length measurements of motors on single MTs + MAP65 (blue) and MAP65 bundles (red); and the final distance traveled (Δx) for motors on MAP65 bundles (green). **B.** Cumulative probability distributions of run length measurements of motors on single microtubules with MAP65 (blue), of motors that reverse direction on MAP65 bundles (green), motors that do not reverse direction on MAP65 bundles (red). In addition, the average distance traveled before or after reversing direction on MAP65 bundles was measured (segments, cyan). **C.** Cumulative probability distributions of association time measurements of motors on single microtubules with MAP65 (blue) and MAP65 bundles (red). **D.** Cumulative probability distributions of moving velocity measurements of motors on single microtubules with MAP65 (blue) and MAP65 bundles (red). **A-D.** For single microtubules with MAP65, N = 91; for MAP65 bundles, N = 98, for motors that reverse on MAP65 bundles, N = 23; for motors that do not reverse on MAP65 bundles, N = 75.

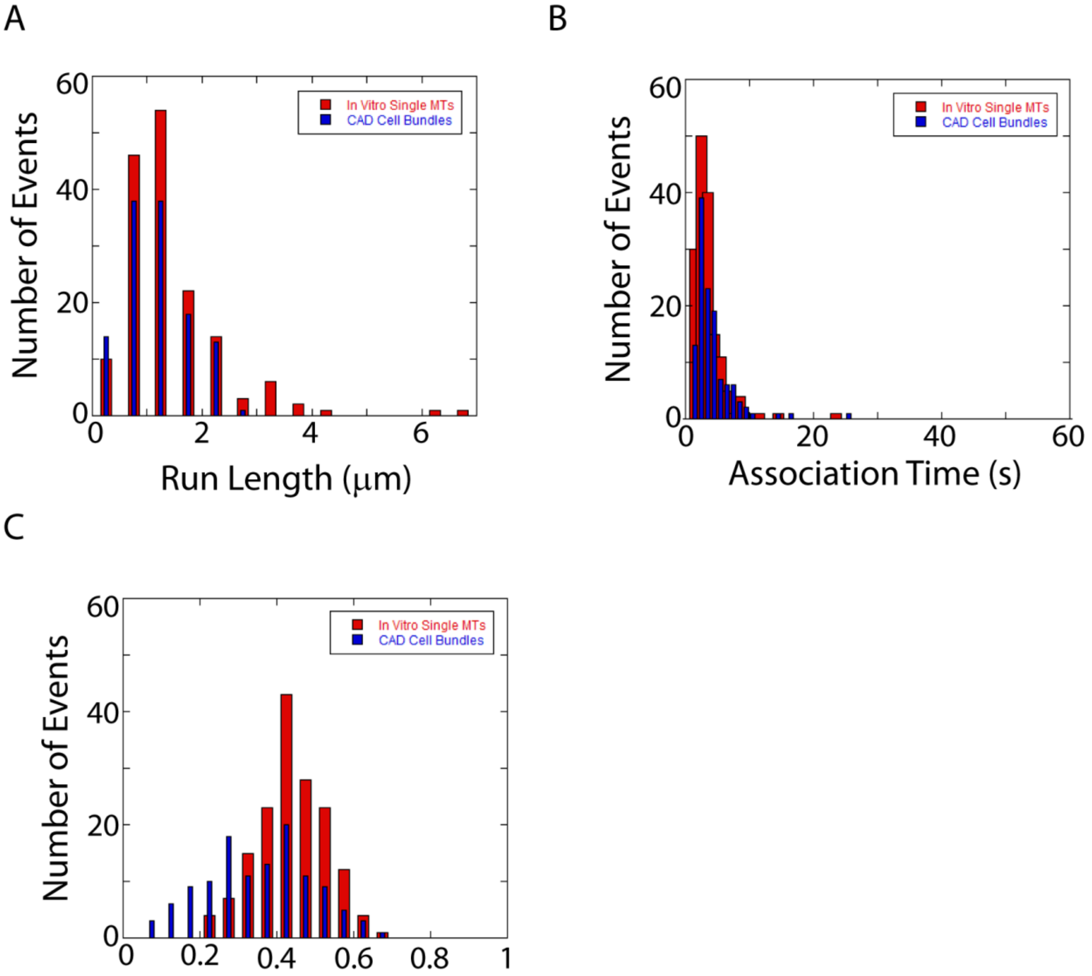

Figure A.9 Kinesin Motility on Cellular Bundles: Histograms

A. Distributions of run length measurements of motors on single microtubules polymerized in vitro (red bars) and on microtubule bundles derived from CAD cells (blue bars). **B.** Distributions of association time measurements of motors on single microtubules polymerized in vitro (red bars) and on microtubule bundles derived from CAD cells (blue bars). **C.** Distributions of moving velocity measurements of motors on single microtubules polymerized in vitro (red bars) and on microtubule bundles derived from CAD cells (blue bars). **A-C.** For data taken on single microtubules polymerized in vitro, N = 160. For data taken on microtubule bundles derived from CAD cells, N = 122.

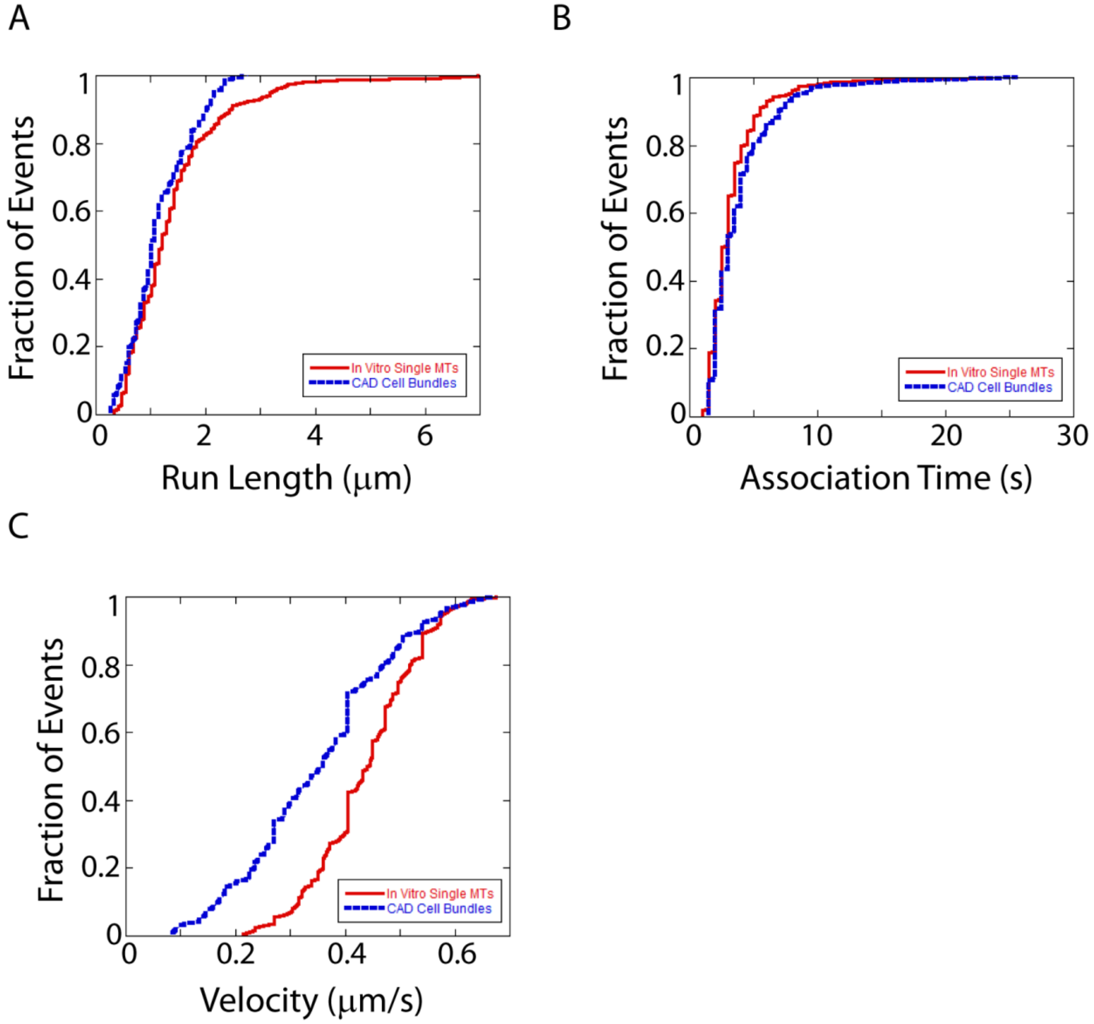

Figure A.10 Kinesin Motility on Cellular Bundles: Cumulative Probability Distributions

A. Cumulative probability distributions of run length measurements of motors on single microtubules polymerized in vitro (red) and on microtubule bundles derived from CAD cells (blue). **B.** Cumulative probability distributions of association time measurements of motors on single microtubules polymerized in vitro (red) and on microtubule bundles derived from CAD cells (blue). **C.** Cumulative probability distributions of moving velocity measurements of motors on single microtubules polymerized in vitro (red) and on microtubule bundles derived from CAD cells (blue). **A-C.** For data taken on single microtubules polymerized in vitro, N = 160. For data taken on microtubule bundles derived from CAD cells, N = 122.

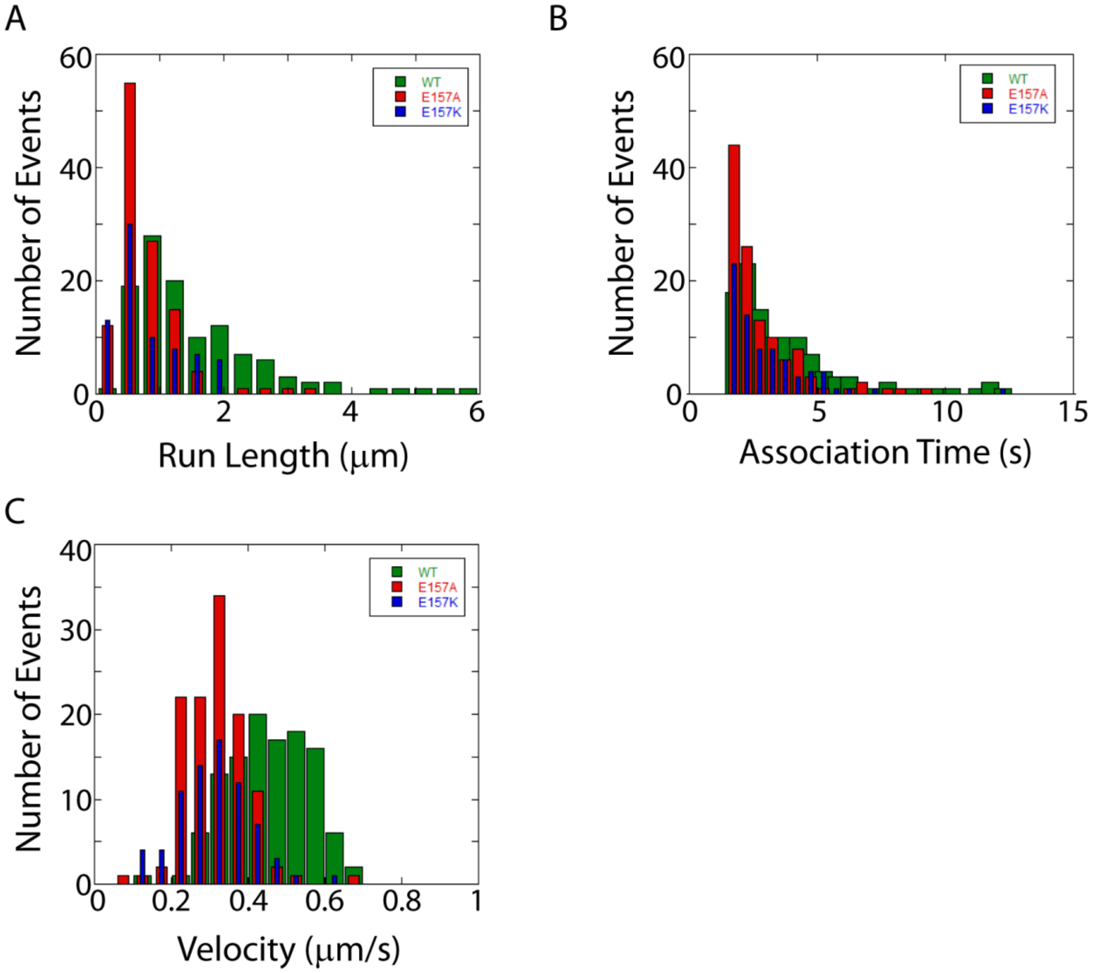

Figure A.11 Single Molecule Studies of Mutant Kinesin Motors: Histograms

A. Distributions of run length measurements for wildtype and E157 mutant kinesin motors. **B.** Distributions of association time measurements for wildtype and E157 mutant kinesin motors. **C.** Distributions of moving velocity measurements for wildtype and E157 mutant kinesin motors. For all plots, number of motors measured for WT, E157A, and E157K was 115, 117, and 74, respectively. Error bars represent standard error of the mean.

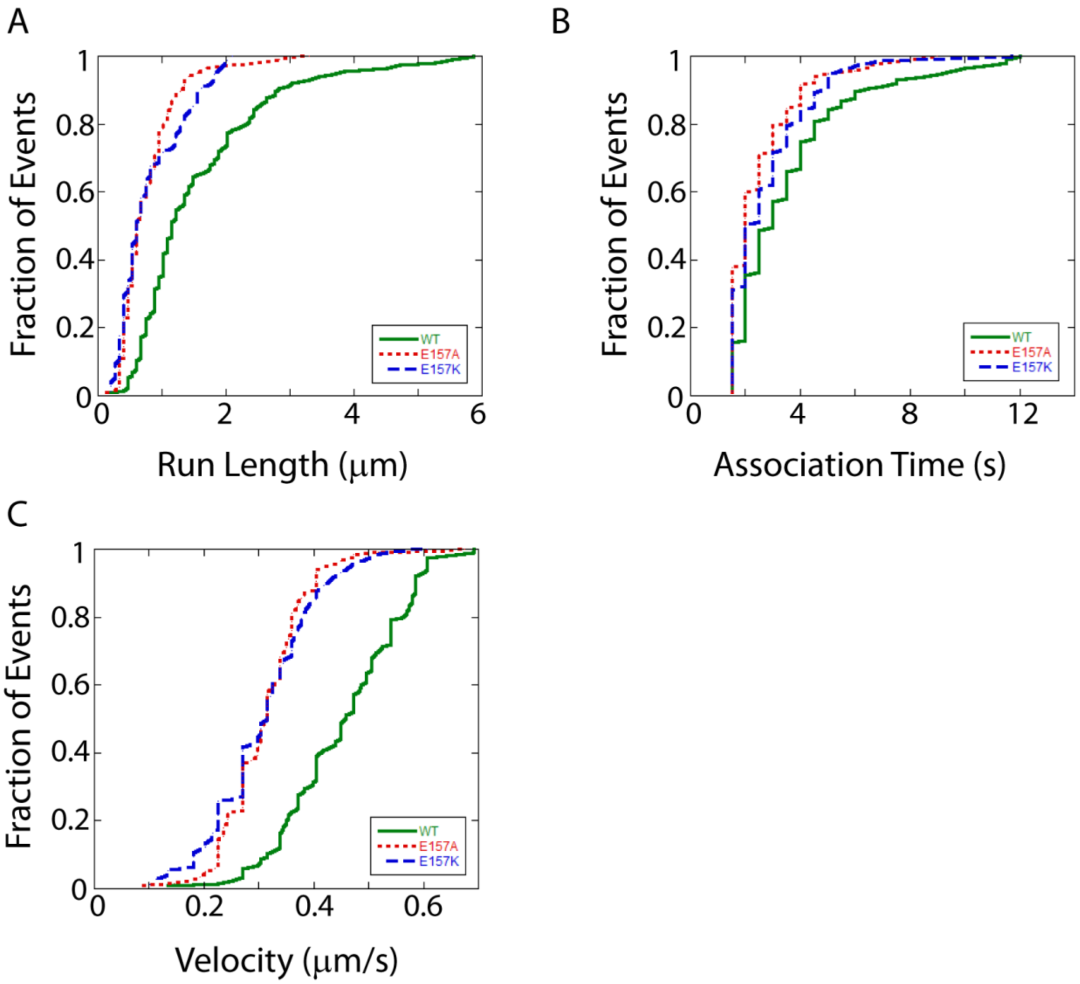

Figure A.12 Single Molecule Studies of Mutant Kinesin Motors: Cumulative Probability Distributions

A. Cumulative probability distributions of run length measurements for wildtype and E157 mutant kinesin motors. **B.** Cumulative probability distributions of association time measurements for wildtype and E157 mutant kinesin motors. **C.** Cumulative probability distributions of moving velocity measurements for wildtype and E157 mutant kinesin motors. For all plots, number of motors measured for WT, E157A, and E157K was 115, 117, and 74, respectively. Error bars represent standard error of the mean.

APPENDIX B
PROTOCOLS

B.1 Tubulin Purification from Pig Brains

Stock Solutions:	PM Buffer (200mL)	PMG Buffer (200mL)
200mM PIPES	100mL	76mL
200mM EGTA	2mL	2mL
100mM $MgSO_4$	2mL	2mL
13.7M Glycerol	-------	116mL

	Super PMG (200mL)
1M PIPES	16mL
1M $MgSO_4$	2mL
200mM EGTA	2mL
13.7M Glycerol	175.2mL

1. Clean pig brains (3) and put in pre-tared 1L beaker
    Remove meniscus, etc. (use kimwipe to help clean)
2. Weigh cleaned brains: _______g
3. Put brains in blender
    Add 0.5mL PM buffer per 1g of brain. Volume of PM: ______mL
4. Pulse blender to homogenize brains (~5 seconds/pulse to prevent mixture from heating up)
5. Pour homogenized brains into ultra centrifuge tubes
6. Balance tubes
7. centrifuge at 100,000 xg for 45 minutes at 2°C with 50.2 Ti rotor
8. Pour supernatant into 500mL graduated cylinder (use pasteur pipette to get all sup)
    Volume of sup: ________mL
9. Add same volume of PMG to the sup (1:1 PMG:sup ratio)
    *If sup volume is greater than 100mL, add ½ volume of sup as super PMG
10. Add GTP to final concentration of 1mM
    ______mL of 100mM GTP stock
11. Cover graduated cylinder with parafilm and mix by inverting
12. Put sup into new ultra centrifuge tubes and balance
13. Polymerize MTs for 45 minutes at 37°C in water bath
14. Set ultra centrifuge to 37°C, place T865 rotor in 37°C incubator to warm up
15. Centrifuge at 100,000 xg in T865 rotor for 45 minutes at 37°C

These are the 1X Pellets (can drop freeze and store at -80°C or continue)

2X Pellets

1. Add PM to pellets using 1/5 volume of original homogenate (1X pellets, step 3)
    Volume of PM Buffer added: ______mL
2. Using a thin, pointed spatula, scrape pellet off side of cfuge tube and into PM buffer
    Lightly shake tube to make sure pellet is loose
    Quickly dump PM buffer + pellet into 15mL dounce in ice slurry
    Repeat for each pellet
3. Homogenize pellets in ice cold dounce until no large chunks seen (will be cloudy)
    Homogenize on ice every 2-3 minutes, for a total of 30 minutes (avoid excessive bubbling)
4. Put homogenized tubulin into ultra (T865) centrifuge tubes
5. Centrifuge 100,000 xg for 30 minutes at 2°C
6. Pour sup into graduated cylinder and approximate volume
    Volume of supernatant: ________mL
7. Add PMG buffer 1:1 with supernatant
    Add ______mL PMG
8. Add GTP to final concentration of 1mM
    Add ______μL 100mM GTP stock
9. Parafilm cylinder and mix by inverting
10. Put supernatant into new ultra T865 centrifuge tubes and incubate 45 minutes at 37°C in water bath
11. Centrifuge at 37°C for 45 minutes at 100,000 xg
12. Remove most of sup, leaving a small amount to cover pellets
13. Drop freeze pellets in liquid nitrogen and store at -80°C

High Salt Purification

1. Quickly thaw 2X pellets in 37°C water bath
2. Remove excess supernatant that froze with pellet
3. Take 2X pellets (2) and homogenize with dounce in 5mL PM buffer for 30 minutes on ice (Homogenize on ice every 2-3 minutes, for a total of 30 minutes, avoid excessive bubbling)
4. Spin at 100,000 xg at 4°C (T865 rotor) for 30 minutes
5. Save sup and add: 0.5 M PIPES
    10% DMSO
    1 mM GTP
    2 mM EGTA
    1 mM $MgSO_4$
6. Incubate at 37°C for 10 minutes
7. Spin 20 minutes at 20,000 xg at 37°C (T865 rotor)
8. Using dounce, homogenize pellet in 4mL PEM-100 on ice for 30 minutes
9. Spin 30 minutes at 100,000 xg at 4°C (T865 rotor)
10. Save supernatant as high salt purified tubulin
11. Bring tubulin to 5 mg/mL using PEM-100
12. Aliquot and drop freeze in liquid nitrogen, store in -80°C

B.2 Fluorescent Labeling of Tubulin

Adapted from Mitchison Lab Protocol

BUFFERS:

5X BRB-80
400 mM PIPES
5 mM $MgCl_2$
5 mM EGTA
pH 6.8 with KOH

High pH Cushion
0.1 M NaHEPES, pH 8.6
1 mM $MgCl_2$
1 mM EGTA
60% (v/v) glycerol

Labeling Buffer
0.1 M NaHEPES, pH 8.6
1 mM $MgCl_2$
1 mM EGTA
40% (v/v) glycerol

Quench
2X BRB-80
100 mM K-Glutamate
40% (v/v) gycerol

Low pH Cushion
60% (v/v) glycerol
in 1X BRB-80

PEM-100
100 mM Na-PIPES
1 mM $MgSO_4$
1 mM EGTA
pH 6.8

1. Thaw high-salt purified tubulin: _______mg in ________mL
2. Add MgCl2 to 4 mM: __________μL of 1M stock
3. Add GTP to 1 mM: ____________μL of 100 mM stock
4. Incubate on ice 5 minutes
5. warm to 37°C
6. Add DMSO to 10% final concentration: _________μL
   *add in 2 steps, mix gently but thoroughly
7. Incubate at 37°C for 45 minutes
8. Warm 15mL high pH cushion in a 25 mL centrifuge tube to 37°C
9. Layer MTs onto cushion (with cut 1mL pipette tip)
10. Spin for 35 minutes in T865 rotor at 53,000 rpm (285,500 xg) at 37°C
11. Dissolve 1mg of dye into 50μL DMSO
    (ie DyLight 650 NHS Ester, Prod #62265, Thermo Scientific)
12. Warm 3 mL Labeling Buffer to 37°C
13. After spin, remove the supernatant above the cushion
14. Rinse supernatant-cushion interface 2 times (1mL each) with warm Labeling Buffer
15. Remove cushion
16. Resuspend pellet in 600μL warm Labeling Buffer using cutoff large pipette tip
    *keep tubulin warm during resuspension
    *continue resuspending until no chunks of tubulin are visible
17. Add the dye to the tubulin (should be 10-20 fold molar excess of dye to tubulin)
    *can estimate tubulin concentration by assuming 70% recovery of starting tubulin
18. Incubate at 37°C for 45 minutes
    *gently vortex mixture every 2-3 minutes during labeling reaction

19. Warm 1mL Quench to 37°C
    Warm 5mL Low pH cushion in 10mL centrifuge tube to 37°C
20. Add equal volume of Quench to labeling reaction and mix well

21. Incubate 5 minutes at 37°C
22. Layer labeling reaction onto low pH cushion
23. Centrifuge 35 minutes at 50,000 rpm (225,600 xg) in 50Ti rotor at 37°C
24. Warm 3 mL 1x BRB-80 to 37°C
25. Remove the supernatant from above the cushion
26. Rinse the supernatant-cushion interface 2 times with 1 mL warm 1x BRB-80
27. Remove cushion
28. Rinse pellet with 1 mL warm 1x BRB-80
29. Resuspend pellet in 800μL of ice cold PEM-100 using cutoff large pipette tip
30. Transfer resuspended chunks of the pellet to a small ice cold dounce (1-2mL volume) in an ice cold water bath
31. Resuspend pellet by gentle douncing until suspension is uniform
    *continue douncing intermittently for total time of 30 minutes
32. Spin depolymerized tubulin for 20 minutes at 71,000 rpm (227,000 xg) in small ultra at 4°C
33. Transfer supernatant to a new tube and estimate volume: __________μL
34. Add: BRB-80 to 1x: __________μL of 5x stock
    $MgCl_2$ to 4 mM: _________μL of 1M stock
    GTP to 1 mM: _________μL of 100 mM stock
35. Incubate on ice for 5 minutes
36. Warm to 37°C for 2 minutes
37. Add ½ volume of glycerol (33% v/v final) and mix well
38. Incubate 45 minutes at 37°C
39. Warm 5 mL Low pH cushion in 10 mL cfuge tube to 37°C
40. Layer MTs onto cushion
41. Spin 35,000 rpm (110,600 xg) in 50Ti rotor at 37°C for 35 minutes
42. Warm 4 mL 1x BRB-80 to 37°C
43. After spin, remove supernatant above the cushion
44. Rinse the supernatant-cushion interface 2 times with 1 mL 1x BRB-80
45. Remove the cushion
46. Rinse pellet 2 times with 1 mL 1x BRB-80 to remove residual glycerol
47. Resuspend pellet in 300μL ice cold PEM-100 using cut large pipette tip
    *pellet should resuspend easily
48. Transfer to dounce and homogenize in ice water slurry for 20-30 minutes
49. Transfer to small ultra cfuge tubes
50. Spin for 15 minutes at 144,400 xg in small ultra at 4°C
51. Recover sup and bring to 5 mg/mL final concentration
52. Aliquot and drop freeze in LN_2

Calculate Protein Concentration:

$$\text{Protein Concentration (M)} = \frac{[A_{280} - (A_{max} \times CF)]}{\varepsilon_{protein}} \times \text{ dilution factor}$$

$\varepsilon_{tubulin\ @\ 280nm} = 115{,}000\ M^{-1}\ cm^{-1}$
$CF = A_{280}$ of fluorophore / A_{max} of fluorophore

Calculate Degree of Labeling:

$$\text{Moles dye per mole protein} = \frac{A_{max} \text{ of labeled protein} \times \text{dilution factor}}{\varepsilon_{fluor} \times \text{protein concentration (M)}}$$

B.3 Microtubule Polymerization

1. Thaw aliquot of labeled and aliquot of unlabeled tubulin and put on ice
   *bring tubulin to final concentration of 5 mg/mL using PEM-100 (if not already at 5 mg/mL)
2. Mix tubulin at desired ratio of labeled:unlabeled (typically use 25% labeled tubulin)
3. Centrifuge 10 minutes at 4^{o}C in small ultra centrifuge at 90,000 rpm (366,000 xg) to remove tubulin aggregates
4. Add supernatant to a new 1.5mL tube
5. Add GTP to 1 mM final concentration
6. Incubate 20 minutes at 37^{o}C
7. Add Taxol to 50 μM
8. Incubate 20 minutes at 37^{o}C
9. Spin 10 minutes at room temperature in tabletop centrifuge at 16,000 xg
10. Discard supernatant
11. Resuspend pellet in PEM-100 + 40 μM Taxol (use cut pipette tip to minimize shearing of microtubules)

<u>1:100 Microtubule Dilution for Use in Assays</u>

98 μL PEM-100
1 μL 2 mM Taxol
1 μL 5mg/mL polymerized microtubules

B.4 Kinesin-1 Purification

Day One:

1. Transform kinesin DNA into Rosetta cells
2. Make 400 mL TPM media in 1L flask:
    - 8g Tryptone
    - 6g Yeast Extract
    - 1.6g NaCl
    - 0.8g Na_2HPO_4
    - 0.4g KH_2PO_4
    - **Add dH_2O to bring final volume to 395.6 mL and autoclave**
    - *4 mL 20% Glucose
    - *400 μL 100 mg/ml Ampicillin *add to media after autoclaved (same day growing cells)

3. Make buffers if needed (sterile filter and store in 4°C)

Lysis Buffer:	Wash Buffer:	Elution Buffer:
50 mM $NaPO_4$, pH 8.0	50 mM $NaPO_4$, pH 6.0	50 mM $NaPO_4$, pH 7.2
250 mM NaCl	250 mM NaCl	500 mM Imidazole
	1 mM $MgCl_2$	250 mM NaCl
		1 mM $MgCl_2$

Day Two:

1. First thing in the morning, make 5 mL starter culture:
    - 5 mL TPM media
    - 50 μL 20% Glucose
    - 5 μL 100mg/ml Ampicillin
    - 15 colonies from transformation plate
2. Incubate starter culture on 37°C shaker until culture is cloudy (approximately 2 hours)
3. Once starter culture is cloudy, add to 400 mL TPM media (*add glucose and ampicillin to TPM media)
4. Grow cells to OD 1-2 in TPM media (usually grow to about 1.7)
5. Let culture cool to room temperature
6. Induce with IPTG (final concentration of 0.2 mM)
7. Shake at room temp overnight

Day Three:

5. Spin down cells for 10 minutes at 4°C, 5,000 rpm
6. Pour off supernatant, freeze pellet in -80°C for 1 hour
    - *pellet can also be left at -80°C for purification on a different day
7. Put pellet on ice and resuspend in 30mL cold Lysis Buffer (keep on ice during resuspension)

To Lysis buffer, add: 30 μl 2mg/mL Aprotonin
30 μl 2mg/mL Leupeptin
30 μl 2mg/mL Pepstatin
30 μl Tween-20
150 μl 100mM ATP

8. Add 62mg Lysozyme
9. Rock at 4°C for 20 minutes

10. Add 15ul DnaseI (Sigma)
11. Sonicate 1 minute on ice (setting 3)
12. Centrifuge 30 minutes, 4°C, 40,000xg (T865 rotor)

Bead Equilibration:

**put beads on rocker for ~30 minutes to get beads fully into solution before using*

1. Add 500ul Ni beads to 2mL tube, add 1.5mL Lysis Buffer, invert tube 10 times, spin 2 min at 500xg, remove sup without disturbing bead bed
2. Repeat for a total of 4 times

13. Pour supernatant into 50mL conical tube (*20 μL gel sample*)
14. Add 620 μl 1M Imidazole to supernatant
15. Add some supernatant to beads, and bring back and forth to get beads into supernatant conical
16. Incubate at 4°C on rocker for 1.5 hours

Wash and Elution Buffers:

Wash Buffer:	**Elution Buffer:**	**PEM-100:**
25 mL Wash Buffer	2.5 mL Elution Buffer	12 mL PEM-100
25 μL 100mM ATP	2.5 μL 100mM ATP	12 μL 100 mM ATP

17. Flow Lysate sup+beads through column (*gel sample of FT*)
    **Lysate FT may be put in -80°C freezer and used for another purification*
18. Flow 25mL Wash Buffer (with ATP added) over column (*gel sample of FT*)
19. Flow 150 μL Elution Buffer+ATP over column and collect first fraction (*gel sample*)
20. Flow 500 μL Elution Buffer+ATP over column for fractions 2-5 (*gel samples*)
    **kinesin will usually be in fraction 2*

21. dot blot to verify fraction containing kinesin:
    -with pencil, draw 5 circles on a piece of filter paper, label circles Elutions 1-5
    -add 1 μL of each fraction to respective circles
    -stain with coomassie for 30 seconds
    -destain

Buffer Exchange:

1. Remove top and bottom cap of NAP-5 column
2. Allow buffer to completely drain by gravity flow
3. Add 10 mL PEM-100+ATP and allow to completely enter gel bed
4. Add 500 μL of elution with protein (determined by dot blot)
5. Put new 1.5 mL tube under column
6. Add 1 mL PEM-100+ATP and collect eluate (*20 μL gel sample*)

Add 200 μL 60% sucrose (10% final concentration) to buffer exchanged kinesin
Aliquot
Drop freeze in liquid nitrogen and store in -80°C

B.5 Coverslip Cleaning and Silanization

*Notes: *For both cleaning and silanization, use a glass box and metal coverslip racks.*
**Before coverslip cleaning, use alconox soap to thoroughly clean glass box and racks*
**In between EVERY step (even ddH$_2$O water rinses), rinse box 3xs with tap water followed by 3xs with ddH$_2$O*
**Make sure that anything that comes in contact with silane is completely dry*

Coverslip Cleaning:

1. Immerse coverslips in 100% acetone for 1 hour
2. Immerse coverslips in 100% ethanol for 10 minutes
3. Rinse 2 times in ddH$_2$O, 5 minutes each
4. Immerse coverslips in 0.1M KOH for 15 minutes (prepare just before use)
   3.05g KOH into 500ml ddH$_2$O
5. Rinse 3 times in ddH$_2$O, 5 minutes each
6. Air dry coverslips overnight (cover racks with foil to prevent dust from landing on coverslips)
7. Rinse glass box with ddH$_2$O and let dry overnight (cover)

Silanization of Coverslips:

1. Once cleaned coverslips and glass box have dried completely, immerse in 2% DDS for 5 minutes (dimethyldichlorosilane solution, 2% w/v-GE Healthcare, PlusOne, Repel-Silane ES, cat # 17-1332-01)
2. Use funnel to pour silane solution back in bottle for reuse
3. Immerse coverslips in 100% ethanol for 5 minutes
4. Immerse coverslips in fresh 100% ethanol for 5 minutes
5. Rinse coverslips 3 times in ddH$_2$O
6. Air dry coverslips

B.6 GFP-Kinesin Single Molecule Assay

5% Pluronic F127
50 mg Pluronic F127
1 mL PEM-100
*incubate overnight at 37^{o}C to get into solution
*before each use, spin 1 minute @ 14,000xg, to remove aggregates
after spin, transfer sup to new tube (keep this), leaving ~100 μL at bottom of tube

Deoxy
1.2 mg Glucose Oxidase (Sigma G-2133, stored in -20^{o}C dessicator)
28.1 μL Catalase (Sigma C-3155, stored in 4^{o}C)
91.9 μL ddH$_2$O
Store at 4^{o}C, remake after 1 week

2% Anti-Tubulin
0.4 μL 50% anti-tubulin antibody (Millipore, MAB1864)
9.6 μL PEM-100

0.5% Pluronic F127
22.5 μL PEM-100
2.5 μL 5% Pluronic F127

1:100 Microtubules
98 μL PEM-100
1 μL 2 mM Taxol
1 μL 5mg/mL microtubules

PEM-Taxol Wash
98 μL PEM-100
1 μL 2 mM Taxol
1 μL 1M DTT

1:100 GFP Kinesin
98 μL PEM-100
1 μL 1M DTT
1 μL GFP-kinesin

1. Clean slide with 70% ethanol and assemble chamber using silanized coverslip (do not clean silanized coverslip with ethanol) and doublestick tape, creating a chamber that holds ~10μL
2. Add 10 μL 2% anti-tubulin antibody, incubate 5 minutes
3. Add 10 μL 5% Pluronic F127, incubate 5 minutes
4. Add 10 μL 1:100 Microtubules, incubate 10 minutes
5. Add 10 μL PEM-Taxol Wash
6. Add 10 μL Motility Mix
   X μL PEM-100
   2 μL 0.5% Pluronic F127
   0.5 μL 1 mM Taxol
   0.5 μL 10 mg/mL BSA in PEM-100
   1 μL 1M DTT
   X μL 1:100 GFP-kinesin (typically use 1-2 μL)
   1 μL 20 mM Mg-ATP
   1 μL 300 mg/mL Glucose
   1 μL Deoxy
   ----
   20 μL final volume

B.7 Qdot Cargos

<u>430 nM Halo Kinesin</u>
X μL PEM-100
1 μL 1M DTT
X μL Halo Kinesin (430 nM final concentration)
----
20 μL final volume

<u>1:10:10 Kinesin:Ligand:Qdot Incubation</u>
**Before using Qdots, spin in tabletop centrifuge for 3 minutes at 5,000xg at 4°C*

1. Mix:
    - 2.1 μL 430 nM Halo Kinesin
    - 9 μL 1μM PEG-biotin ligand
2. Incubate at room temperature 10 minutes
3. Add 9 μL 1 μM Qdots (take from top after they have been spun down)
4. Mix and incubate at room temperature 10 minutes
5. Incubate on ice 4-6 hours
    - **kinesin is now at 45 nM*
    - **Qdots are now at 450 nM*

B.8 Qdot Cargo Assays

2% anti-tubulin antibody
0.4 mL anti-tubulin antibody
9.6 mL PEM-100

1:100 Microtubules
98 μL PEM-100
1 μL 2 mM Taxol
1 μL 5 mg/mL MTs

PEM-Taxol
98 μL PEM-100
1 μL 2 mM Taxol
1 μL 1M DTT

Qdot-Kinesin
X μL PEM-100
1 μL 1M DTT
X μL Qdot-Kinesin*
----
10 μL final volume

*use 45 nM kinesin as starting concentration. For final kinesin densities on MT greater than or equal to 10 nM, use final concentration of 10 nM Qdot-Kinesin. For 1 or 5 nM final densities, use final concentrations of 1 or 5 nM Qdot-kinesin here)

1. Clean slide with 70% ethanol and assemble chamber with silanized coverslip and doublestick tape
2. Add 10 μL 2% anti-tubulin, incubate 5 minutes
3. Add 10 μL 5% Pluronic F127, incubate 5 minutes
4. Add 10 μL 1:100 Microtubules, incubate 10 minutes
5. Add 10 μL PEM-Taxol Wash
6. Add 10 μL Qdot-Kinesin, incubate 10 minutes
7. Add 10 μL Motility Mix
   X μL PEM-100
   2 μL 0.5% Pluronic F127
   0.5 μL 1 mM Taxol
   0.5 μL 10 mg/mL BSA
   1 μL 1M DTT
   X μL Qdot-Kinesin (same final concentration as step 6)
   X μL Unlabeled Halo Kinesin*
   1 μL 10 mM ATP
   1 μL 300 mg/mL Glucose
   1 μL Deoxy
   ----
   20 μL final volume

*final concentration should be final kinesin density desired on MTs minus what was added as Qdot-Kinesin in motility mix

B.9 Kinesin Motility on PEG Bundles

1:10 MTs
8.8 μL PEM-100
0.2 μL 2 mM Taxol
1 μL 5 mg/mL Microtubules

5% PEG Bundles
19.5 μL PEM-100
0.5 μL 2 mM Taxol
25 μL 10% PEG, mw 40,000
5 μL 1:10 Microtubules
Incubate at 37^{o}C, 10 minutes

0.5% Pluronic F127
22.5 μL PEM-100
2.5 μL 5% F127

2% Anti-Tubulin Antibody
0.4 μL YL1/2 tubulin abody
9.6 μL PEM-100

PEM-Taxol+5% PEG
22 μL PEM-100
0.25 μL 2 mM Taxol
0.25 μL 1M DTT
2.5 μL 50% PEG, mw 40,000

1:500 GFP-Kinesin
247 μL PEM-100
2.5 μL 1M DTT
0.5 μL GFP-kinesin
make up right before addition to motility mix

1. Clean glass slide with 70% ethanol and assemble chamber with silanized coverslip and doublestick tape
2. Add 10 μL 2% anti-tubulin antibody, incubate 5 minutes
3. Add 10 μL 5% Pluronic F127, incubate 5 minutes
4. Add 10 μL 5% PEG microtubule bundles, incubate 10 minutes
5. Add 10 μL PEM-Taxol+5% PEG
6. Add 10 μL Motility Mix

X μL PEM-100
2 μL 0.5% Pluronic F127
0.5 μL 1 mM Taxol
0.5 μL 10 mg/mL BSA in PEM-100
1 μL 1M DTT
2 μL 50% PEG, mw 40,000
X μL 1:500 GFP-kinesin (typically use approximately 0.5 μL)
1 μL 10 mM ATP
1 μL 300 mg/mL Glucose
1 μL Deoxy

----

20 μL final volume

B.10 Kinesin Motility on MAP65 Bundles

1:10 MTs
8.8 µL PEM-100
0.2 µL 2 mM Taxol
1 µL 5 mg/mL Microtubules

2% MAP65 Bundles
X µL PEM-100
0.45 µL 2 mM Taxol
X µL MAP65 (112 nM final concentration)
4.5 µL 1:10 Microtubules
----
45 µL final volume
Incubate at 37^{o}C, 10 minutes

2% Anti-Tubulin Antibody
0.4 µL YL1/2 tubulin antibody
9.6 µL PEM-100

PEM-Taxol+2% MAP65
X µL PEM-100
0.45 µL 2 mM Taxol
0.45 µL 1M DTT
X µL MAP65 (112 nM final concentration)

0.5% Pluronic F127
22.5 µL PEM-100
2.5 µL 5% F127

1:100 GFP-Kinesin
98 µL PEM-100
1 µL 1M DTT
1 µL GFP-kinesin

1. Clean glass slide with 70% ethanol and assemble chamber with silanized coverslip and doublestick tape
2. Add 10 µL 2% anti-tubulin antibody, incubate 5 minutes
3. Add 10 µL 5% Pluronic F127, incubate 5 minutes
4. Add 10 µL 2% MAP65 microtubule bundles, incubate 10 minutes
5. Add 10 µL PEM-Taxol+2% MAP65
6. Add 10 µL Motility Mix
    X µL PEM-100
    2 µL 0.5% Pluronic F127
    0.5 µL 1 mM Taxol
    0.5 µL 10 mg/mL BSA in PEM-100
    1 µL 1M DTT
    X µL MAP65 (112 nM final concentration)
    X µL 1:100 GFP-kinesin (typically use approximately 0.5 µL)
    1 µL 10 mM ATP
    1 µL 300 mg/mL Glucose
    1 µL Deoxy
    ----
    20 µL final volume

B.11 Cad Cell Culture

DMEM/F12 Media (Gibco, 12400-024)

1. Add entire packet of powder to 1 L flask (rinse packet with ddH_2O to get all powder into beaker)
2. Add 1.2g of $NaHCO_3$
3. Bring volume to ~890 mL with ddH_2O
4. Add 10mL 100x antibiotic/antimycotic
5. pH to 7.3 with NaOH or HCl
6. Bring final volume to 900mL with ddH_2O
7. Add 100mL serum (or dH_2O for (-) serum media)
7. Filter sterilize in hood

Splitting Cad Cells

1. Add 4.5 mL DMEM/F12 media + 10% serum to $25cm^2$ T-flask (Becton-Dickinson, 35-3082)
2. Put T-flask with media in incubator for 5-10 minutes
3. Using 1 mL pipette, pipette cells up and down against surface to get all cells in solution
4. Add 0.5 mL cells to new flask
5. Split cells every 3-4 days (ie Monday and Friday)

Plating Cad Cells for Differentiation

1. Plate 20,000-40,000 cells per glass bottom dish (In Vitro Scientific, 35mm Dish with 20mm Bottom Well, D35-20-1.5-N) in DMEM/F12 media + 10% serum
2. Allow cells to adhere to surface
3. Rinse cells 2 times in DMEM/F12 (-) serum media
4. Add 2 mL DMEM/F12 (-) serum media
5. Allow cells to grow processes for 2-3 days

B.12 Cad Cell Membrane Extraction

Adapted from: Sivaramakrishnan and Spudich. 2009. Coupled myosin VI motors facilitate unidirectional movement on an F-actin network. JCB. 187: 53-60.

<u>Extraction Buffer</u>
50 mM Imidazole, pH 6.8
50 mM KCl
0.5 mM $MgCl_2$
0.1 mM EDTA
1 mM EGTA
50 μM Taxol
1% Triton X-100
4% PEG, mw 40,000

1. Wash cells gently with 85% PBS, 2 times
2. Add 150 μL Extraction Buffer to well in plate with differentiated cells, let sit 4 minutes
3. Add 150 μL 85% PBS + 50 μM Taxol solution to well, let sit 45 minutes
4. Rinse cells with PEM-100 + 50 μM Taxol + 1 mg/mL BSA solution, let sit 5 minutes
5. Add 150 μL motility mix with final concentration of 1 mg/mL BSA

B.13 Kinesin-1 Gliding Assay

Chamber Wash
22.5 µL PEM-100
25 µL 10 mg/mL BSA
(In PEM-100)
1.5 µL 2mM Taxol
1 µL 1M DTT

1:100 Microtubules
98 µL PEM-100
1 µL 2 mM Taxol
1 µL 5 mg/mL MTs

Activation Mix
45.5 µL PEM-100
0.5 µL 2 mM Taxol
1 µL 1M DTT
1 µL 100 mM Mg-ATP
1 µL 300 mg/mL Glucose
1 µL deoxy

1. Clean coverslip and slide with 70% ethanol and assemble chamber with double stick tape
2. Add 10 µL purified kinesin to chamber, incubate 5 minutes
3. Add 10 µL Chamber Wash to chamber
4. Add 10 µL 1:100 Microtubule dilution to chamber, incubate 2 minutes
5. Add 10 µL Activation Mix to chamber
6. Image microtubules

BIBLIOGRAPHY

Ackmann, M., H. Wiech, and E. Mandelkow. 2000. Nonsaturable binding indicates clustering of tau on the microtubule surface in a paired helical filament-like conformation. *The Journal of biological chemistry*. 275:30335-30343.

Alexander, J.E., D.F. Hunt, M.K. Lee, J. Shabanowitz, H. Michel, S.C. Berlin, T.L. MacDonald, R.J. Sundberg, L.I. Rebhun, and A. Frankfurter. 1991. Characterization of posttranslational modifications in neuron-specific class III beta-tubulin by mass spectrometry. *Proceedings of the National Academy of Sciences of the United States of America*. 88:4685-4689.

Ali, M.Y., H. Lu, C.S. Bookwalter, D.M. Warshaw, and K.M. Trybus. 2008. Myosin V and Kinesin act as tethers to enhance each others' processivity. *Proceedings of the National Academy of Sciences of the United States of America*. 105:4691-4696.

Arai, T., and Y. Kaziro. 1977. Role of GTP in the assembly of microtubules. *Journal of biochemistry*. 82:1063-1071.

Arce, C.A., J.A. Rodriguez, H.S. Barra, and R. Caputo. 1975. Incorporation of L-tyrosine, L-phenylalanine and L-3,4-dihydroxyphenylalanine as single units into rat brain tubulin. *European journal of biochemistry / FEBS*. 59:145-149.

Asai, D.J., and M.P. Koonce. 2001. The dynein heavy chain: structure, mechanics and evolution. *Trends in cell biology*. 11:196-202.

Baas, P.W., J.S. Deitch, M.M. Black, and G.A. Banker. 1988. Polarity orientation of microtubules in hippocampal neurons: uniformity in the axon and nonuniformity in the dendrite. *Proceedings of the National Academy of Sciences of the United States of America*. 85:8335-8339.

Beeg, J., S. Klumpp, R. Dimova, R.S. Gracia, E. Unger, and R. Lipowsky. 2008. Transport of beads by several kinesin motors. *Biophysical journal*. 94:532-541.

Bieling, P., S. Kandels-Lewis, I.A. Telley, J. van Dijk, C. Janke, and T. Surrey. 2008. CLIP-170 tracks growing microtubule ends by dynamically recognizing composite EB1/tubulin-binding sites. *The Journal of cell biology*. 183:1223-1233.

Bisig, C.G., M.E. Chesta, G.G. Zampar, S.A. Purro, V.S. Santander, and C.A. Arce. 2009. Lack of stabilized microtubules as a result of the absence of major maps in CAD cells does not preclude neurite formation. *The FEBS journal*. 276:7110-7123.

Block, S.M., L.S. Goldstein, and B.J. Schnapp. 1990. Bead movement by single kinesin molecules studied with optical tweezers. *Nature*. 348:348-352.

Bohm, K.J., R. Stracke, and E. Unger. 2000. Speeding up kinesin-driven microtubule gliding in vitro by variation of cofactor composition and physicochemical parameters. *Cell biology international*. 24:335-341.

Brendza, K.M., D.J. Rose, S.P. Gilbert, and W.M. Saxton. 1999. Lethal kinesin mutations reveal amino acids important for ATPase activation and structural coupling. *The Journal of biological chemistry*. 274:31506-31514.

Brown, A. 2003. Axonal transport of membranous and nonmembranous cargoes: a unified perspective. *The Journal of cell biology*. 160:817-821.

Chan, J., C.G. Jensen, L.C. Jensen, M. Bush, and C.W. Lloyd. 1999. The 65-kDa carrot microtubule-associated protein forms regularly arranged filamentous cross-bridges between microtubules. *Proceedings of the National Academy of Sciences of the United States of America*. 96:14931-14936.

Chen, J., Y. Kanai, N.J. Cowan, and N. Hirokawa. 1992. Projection domains of MAP2 and tau determine spacings between microtubules in dendrites and axons. *Nature*. 360:674-677.

Chevalier-Larsen, E., and E.L. Holzbaur. 2006. Axonal transport and neurodegenerative disease. *Biochimica et biophysica acta*. 1762:1094-1108.

Conway, L., and J.L. Ross. 2013. A model system to study transport of self-assembled cargos. *Commun Integr Biol*. 6:e25387-25381-e25387-25383.

Conway, L., D. Wood, E. Tuzel, and J.L. Ross. 2012. Motor transport of self-assembled cargos in crowded environments. *Proceedings of the National Academy of Sciences of the United States of America*. 109:20814-20819.

Coy, D.L., W.O. Hancock, M. Wagenbach, and J. Howard. 1999. Kinesin's tail domain is an inhibitory regulator of the motor domain. *Nature cell biology*. 1:288-292.

Dauer, W., and S. Przedborski. 2003. Parkinson's disease: mechanisms and models. *Neuron*. 39:889-909.

Derr, N.D., B.S. Goodman, R. Jungmann, A.E. Leschziner, W.M. Shih, and S.L. Reck-Peterson. 2012. Tug-of-war in motor protein ensembles revealed with a programmable DNA origami scaffold. *Science*. 338:662-665.

Diehl, M.R., K. Zhang, H.J. Lee, and D.A. Tirrell. 2006. Engineering cooperativity in biomotor-protein assemblies. *Science*. 311:1468-1471.

Dietrich, K.A., C.V. Sindelar, P.D. Brewer, K.H. Downing, C.R. Cremo, and S.E. Rice. 2008. The kinesin-1 motor protein is regulated by a direct interaction of its head and tail. *Proceedings of the National Academy of Sciences of the United States of America*. 105:8938-8943.

Dixit, R., J.L. Ross, Y.E. Goldman, and E.L. Holzbaur. 2008. Differential regulation of dynein and kinesin motor proteins by tau. *Science*. 319:1086-1089.

Djagaeva, I., D.J. Rose, A. Lim, C.E. Venter, K.M. Brendza, P. Moua, and W.M. Saxton. 2012. Three routes to suppression of the neurodegenerative phenotypes caused by kinesin heavy chain mutations. *Genetics*. 192:173-183.

Dunn, S., E.E. Morrison, T.B. Liverpool, C. Molina-Paris, R.A. Cross, M.C. Alonso, and M. Peckham. 2008. Differential trafficking of Kif5c on tyrosinated and detyrosinated microtubules in live cells. *Journal of cell science*. 121:1085-1095.

Edde, B., J. Rossier, J.P. Le Caer, E. Desbruyeres, F. Gros, and P. Denoulet. 1990. Posttranslational glutamylation of alpha-tubulin. *Science*. 247:83-85.

Fan, J., A.D. Griffiths, A. Lockhart, R.A. Cross, and L.A. Amos. 1996. Microtubule minus ends can be labelled with a phage display antibody specific to alpha-tubulin. *Journal of molecular biology*. 259:325-330.

Furuta, K., A. Furuta, Y.Y. Toyoshima, M. Amino, K. Oiwa, and H. Kojima. 2013. Measuring collective transport by defined numbers of processive and nonprocessive kinesin motors. *Proceedings of the National Academy of Sciences of the United States of America*. 110:501-506.

Gaillard, J., E. Neumann, D. Van Damme, V. Stoppin-Mellet, C. Ebel, E. Barbier, D. Geelen, and M. Vantard. 2008. Two microtubule-associated proteins of Arabidopsis MAP65s promote antiparallel microtubule bundling. *Molecular biology of the cell*. 19:4534-4544.

Gao, Y., and M.L. Kilfoil. 2009. Accurate detection and complete tracking of large populations of features in three dimensions. *Optics express*. 17:4685-4704.

Gigant, B., W. Wang, B. Dreier, Q. Jiang, L. Pecqueur, A. Pluckthun, C. Wang, and M. Knossow. 2013. Structure of a kinesin-tubulin complex and implications for kinesin motility. *Nature structural & molecular biology*.

Gilbert, S.P., M.L. Moyer, and K.A. Johnson. 1998. Alternating site mechanism of the kinesin ATPase. *Biochemistry*. 37:792-799.

Goldstein, L.S. 2001. Kinesin molecular motors: transport pathways, receptors, and human disease. *Proceedings of the National Academy of Sciences of the United States of America*. 98:6999-7003.

Gross, S.P. 2004. Hither and yon: a review of bi-directional microtubule-based transport. *Physical biology*. 1:R1-11.

Gross, S.P., M. Vershinin, and G.T. Shubeita. 2007. Cargo transport: two motors are sometimes better than one. *Current biology : CB*. 17:R478-486.

Gutierrez-Medina, B., A.N. Fehr, and S.M. Block. 2009. Direct measurements of kinesin torsional properties reveal flexible domains and occasional stalk reversals during stepping. *Proceedings of the National Academy of Sciences of the United States of America*. 106:17007-17012.

Hackney, D.D., and M.F. Stock. 2008. Kinesin tail domains and Mg2+ directly inhibit release of ADP from head domains in the absence of microtubules. *Biochemistry*. 47:7770-7778.

Hallak, M.E., J.A. Rodriguez, H.S. Barra, and R. Caputto. 1977. Release of tyrosine from tyrosinated tubulin. Some common factors that affect this process and the assembly of tubulin. *FEBS letters*. 73:147-150.

Hancock, W.O., and J. Howard. 1998. Processivity of the motor protein kinesin requires two heads. *The Journal of cell biology*. 140:1395-1405.

Hariharan, V., and W.O. Hancock. 2009. Insights into the Mechanical Properties of the Kinesin Neck Linker Domain from Sequence Analysis and Molecular Dynamics Simulations. *Cellular and molecular bioengineering*. 2:177-189.

Heidemann, S.R., J.M. Landers, and M.A. Hamborg. 1981. Polarity orientation of axonal microtubules. *The Journal of cell biology*. 91:661-665.

Hendricks, A.G., E. Perlson, J.L. Ross, H.W. Schroeder, 3rd, M. Tokito, and E.L. Holzbaur. 2010. Motor coordination via a tug-of-war mechanism drives bidirectional vesicle transport. *Current biology : CB*. 20:697-702.

Herold, C., C. Leduc, R. Stock, S. Diez, and P. Schwille. 2012. Long-range transport of giant vesicles along microtubule networks. *Chemphyschem : a European journal of chemical physics and physical chemistry*. 13:1001-1006.

Hirokawa, N. 1994. Microtubule organization and dynamics dependent on microtubule-associated proteins. *Current opinion in cell biology*. 6:74-81.

Hirokawa, N. 1998. Kinesin and dynein superfamily proteins and the mechanism of organelle transport. *Science*. 279:519-526.

Hirose, K., J. Fan, and L.A. Amos. 1995. Re-examination of the polarity of microtubules and sheets decorated with kinesin motor domain. *Journal of molecular biology*. 251:329-333.

Hirose, K., J. Lowe, M. Alonso, R.A. Cross, and L.A. Amos. 1999. 3D electron microscopy of the interaction of kinesin with tubulin. *Cell structure and function*. 24:277-284.

Holleran, E.A., L.A. Ligon, M. Tokito, M.C. Stankewich, J.S. Morrow, and E.L. Holzbaur. 2001. beta III spectrin binds to the Arp1 subunit of dynactin. *The Journal of biological chemistry*. 276:36598-36605.

Holzbaur, E.L. 2004. Motor neurons rely on motor proteins. *Trends in cell biology*. 14:233-240.

Hunt, A.J., and J. Howard. 1993. Kinesin swivels to permit microtubule movement in any direction. *Proceedings of the National Academy of Sciences of the United States of America*. 90:11653-11657.

Hyman, A., D. Drechsel, D. Kellogg, S. Salser, K. Sawin, P. Steffen, L. Wordeman, and T. Mitchison. 1991. Preparation of modified tubulins. *Methods in enzymology*. 196:478-485.

Ikegami, K., R.L. Heier, M. Taruishi, H. Takagi, M. Mukai, S. Shimma, S. Taira, K. Hatanaka, N. Morone, I. Yao, P.K. Campbell, S. Yuasa, C. Janke, G.R. Macgregor, and M. Setou. 2007. Loss of alpha-tubulin polyglutamylation in ROSA22 mice is associated with abnormal targeting of KIF1A and modulated synaptic function. *Proceedings of the National Academy of Sciences of the United States of America*. 104:3213-3218.

Janke, C., and J.C. Bulinski. 2011. Post-translational regulation of the microtubule cytoskeleton: mechanisms and functions. *Nature reviews. Molecular cell biology*. 12:773-786.

Kamal, A., G.B. Stokin, Z. Yang, C.H. Xia, and L.S. Goldstein. 2000. Axonal transport of amyloid precursor protein is mediated by direct binding to the kinesin light chain subunit of kinesin-I. *Neuron*. 28:449-459.

King, S.J., and T.A. Schroer. 2000. Dynactin increases the processivity of the cytoplasmic dynein motor. *Nature cell biology*. 2:20-24.

Klumpp, L.M., K.M. Brendza, J.E. Gatial, 3rd, A. Hoenger, W.M. Saxton, and S.P. Gilbert. 2004. Microtubule-kinesin interface mutants reveal a site critical for communication. *Biochemistry*. 43:2792-2803.

Klumpp, L.M., K.M. Brendza, J.M. Rosenberg, A. Hoenger, and S.P. Gilbert. 2003. Motor domain mutation traps kinesin as a microtubule rigor complex. *Biochemistry*. 42:2595-2606.

Klumpp, S., and R. Lipowsky. 2005. Cooperative cargo transport by several molecular motors. *Proceedings of the National Academy of Sciences of the United States of America*. 102:17284-17289.

Konishi, Y., and M. Setou. 2009. Tubulin tyrosination navigates the kinesin-1 motor domain to axons. *Nature neuroscience*. 12:559-567.

Korn, C.B., S. Klumpp, R. Lipowsky, and U.S. Schwarz. 2009. Stochastic simulations of cargo transport by processive molecular motors. *The Journal of chemical physics*. 131:245107.

Kubo, T., H.A. Yanagisawa, T. Yagi, M. Hirono, and R. Kamiya. 2010. Tubulin polyglutamylation regulates axonemal motility by modulating activities of inner-arm dyneins. *Current biology : CB*. 20:441-445.

Kunwar, A., M. Vershinin, J. Xu, and S.P. Gross. 2008. Stepping, strain gating, and an unexpected force-velocity curve for multiple-motor-based transport. *Current biology : CB*. 18:1173-1183.

L'Hernault, S.W., and J.L. Rosenbaum. 1985. Chlamydomonas alpha-tubulin is posttranslationally modified by acetylation on the epsilon-amino group of a lysine. *Biochemistry*. 24:473-478.

Lasek, R.J., Brady, ST. 1984. Adenylyl imidodiphosphate (AMP-PNP), a non-hydrolyzable analogue of ATP produces a stable inter-mediate in the motility cycle of fast axonal transport. *Biol Bull*. 167:503.

Leduc, C., K. Padberg-Gehle, V. Varga, D. Helbing, S. Diez, and J. Howard. 2012. Molecular crowding creates traffic jams of kinesin motors on microtubules. *Proceedings of the National Academy of Sciences of the United States of America*. 109:6100-6105.

Leduc, C., F. Ruhnow, J. Howard, and S. Diez. 2007. Detection of fractional steps in cargo movement by the collective operation of kinesin-1 motors. *Proceedings of the National Academy of Sciences of the United States of America*. 104:10847-10852.

Li, H., T. Mao, Z. Zhang, and M. Yuan. 2007a. The AtMAP65-1 cross-bridge between microtubules is formed by one dimer. *Plant & cell physiology*. 48:866-874.

Li, H., M. Yuan, and T. Mao. 2007b. AtMAP65-1 binds to tubulin dimers to promote tubulin assembly. *Journal of biochemistry and molecular biology*. 40:218-225.

Li, W., J.T. Xia, and Y. Feng. 2006. Microtubule stability and MAP1B upregulation control neuritogenesis in CAD cells. *Acta pharmacologica Sinica*. 27:1119-1126.

Liao, G., and G.G. Gundersen. 1998. Kinesin is a candidate for cross-bridging microtubules and intermediate filaments. Selective binding of kinesin to detyrosinated tubulin and vimentin. *The Journal of biological chemistry*. 273:9797-9803.

Lodish, H., A. Berk, S.L. Zipursky, P. Matsudaira, D. Baltimore, and J. Darnell. 2000. Molecular Cell Biology. Freeman, W.H., New York.

Loiodice, I., J. Staub, T.G. Setty, N.P. Nguyen, A. Paoletti, and P.T. Tran. 2005. Ase1p organizes antiparallel microtubule arrays during interphase and mitosis in fission yeast. *Molecular biology of the cell*. 16:1756-1768.

Lorenz, T., and M. Willard. 1978. Subcellular fractionation of intra-axonally transport polypeptides in the rabbit visual system. *Proceedings of the National Academy of Sciences of the United States of America*. 75:505-509.

Mallik, R., B.C. Carter, S.A. Lex, S.J. King, and S.P. Gross. 2004. Cytoplasmic dynein functions as a gear in response to load. *Nature*. 427:649-652.

Marks, D.L., J.M. Larkin, and M.A. McNiven. 1994. Association of kinesin with the Golgi apparatus in rat hepatocytes. *Journal of cell science*. 107 (Pt 9):2417-2426.

Matsuyama, A., T. Shimazu, Y. Sumida, A. Saito, Y. Yoshimatsu, D. Seigneurin-Berny, H. Osada, Y. Komatsu, N. Nishino, S. Khochbin, S. Horinouchi, and M. Yoshida. 2002. In vivo destabilization of dynamic microtubules by HDAC6-mediated deacetylation. *The EMBO journal*. 21:6820-6831.

Meijering, E., O. Dzyubachyk, and I. Smal. 2012. Methods for cell and particle tracking. *Methods in enzymology*. 504:183-200.

Merlitz H, W.C., Sommer JU. 2012. Inclusion Free Energy of Nanoparticles in Polymer Brushes. *Macromolecules*. 45:8494–8501.

Muller, M.J., S. Klumpp, and R. Lipowsky. 2010. Bidirectional transport by molecular motors: enhanced processivity and response to external forces. *Biophysical journal*. 98:2610-2618.

Needleman, D.J., M.A. Ojeda-Lopez, U. Raviv, K. Ewert, H.P. Miller, L. Wilson, and C.R. Safinya. 2005. Radial compression of microtubules and the mechanism of action of taxol and associated proteins. *Biophysical journal*. 89:3410-3423.

Neuwald, A.F., L. Aravind, J.L. Spouge, and E.V. Koonin. 1999. AAA+: A class of chaperone-like ATPases associated with the assembly, operation, and disassembly of protein complexes. *Genome research*. 9:27-43.

Nogales, E., M. Whittaker, R.A. Milligan, and K.H. Downing. 1999. High-resolution model of the microtubule. *Cell*. 96:79-88.

Nogales, E., S.G. Wolf, and K.H. Downing. 1998. Structure of the alpha beta tubulin dimer by electron crystallography. *Nature*. 391:199-203.

Palmer, R.E., D.S. Sullivan, T. Huffaker, and D. Koshland. 1992. Role of astral microtubules and actin in spindle orientation and migration in the budding yeast, Saccharomyces cerevisiae. *The Journal of cell biology*. 119:583-593.

Peloquin, J., Y. Komarova, and G. Borisy. 2005. Conjugation of fluorophores to tubulin. *Nature methods*. 2:299-303.

Peris, L., M. Thery, J. Faure, Y. Saoudi, L. Lafanechere, J.K. Chilton, P. Gordon-Weeks, N. Galjart, M. Bornens, L. Wordeman, J. Wehland, A. Andrieux, and D. Job. 2006. Tubulin tyrosination is a major factor affecting the recruitment of CAP-Gly proteins at microtubule plus ends. *The Journal of cell biology*. 174:839-849.

Peris, L., M. Wagenbach, L. Lafanechere, J. Brocard, A.T. Moore, F. Kozielski, D. Job, L. Wordeman, and A. Andrieux. 2009. Motor-dependent microtubule disassembly driven by tubulin tyrosination. *The Journal of cell biology*. 185:1159-1166.

Perlson, E., S. Maday, M.M. Fu, A.J. Moughamian, and E.L. Holzbaur. 2010. Retrograde axonal transport: pathways to cell death? *Trends in neurosciences*. 33:335-344.

Pierce, D.W., and R.D. Vale. 1998. Assaying processive movement of kinesin by fluorescence microscopy. *Methods in enzymology*. 298:154-171.

Qi, Y., J.K. Wang, M. McMillian, and D.M. Chikaraishi. 1997. Characterization of a CNS cell line, CAD, in which morphological differentiation is initiated by serum deprivation. *The Journal of neuroscience : the official journal of the Society for Neuroscience*. 17:1217-1225.

Ray, S., E. Meyhofer, R.A. Milligan, and J. Howard. 1993. Kinesin follows the microtubule's protofilament axis. *The Journal of cell biology*. 121:1083-1093.

Reck-Peterson, S.L., and R.D. Vale. 2004. Molecular dissection of the roles of nucleotide binding and hydrolysis in dynein's AAA domains in Saccharomyces cerevisiae. *Proceedings of the National Academy of Sciences of the United States of America*. 101:14305.

Reck-Peterson, S.L., A. Yildiz, A.P. Carter, A. Gennerich, N. Zhang, and R.D. Vale. 2006. Single-molecule analysis of dynein processivity and stepping behavior. *Cell*. 126:335-348.

Redeker, V., N. Levilliers, J.M. Schmitter, J.P. Le Caer, J. Rossier, A. Adoutte, and M.H. Bre. 1994. Polyglycylation of tubulin: a posttranslational modification in axonemal microtubules. *Science*. 266:1688-1691.

Rice, S., A.W. Lin, D. Safer, C.L. Hart, N. Naber, B.O. Carragher, S.M. Cain, E. Pechatnikova, E.M. Wilson-Kubalek, M. Whittaker, E. Pate, R. Cooke, E.W. Taylor, R.A. Milligan, and R.D. Vale. 1999. A structural change in the kinesin motor protein that drives motility. *Nature*. 402:778-784.

Rogers, A.R., J.W. Driver, P.E. Constantinou, D. Kenneth Jamison, and M.R. Diehl. 2009. Negative interference dominates collective transport of kinesin motors in the absence of load. *Physical chemistry chemical physics : PCCP*. 11:4882-4889.

Romberg, L., D.W. Pierce, and R.D. Vale. 1998. Role of the kinesin neck region in processive microtubule-based motility. *The Journal of cell biology*. 140:1407-1416.

Ross, J.L., H. Shuman, E.L. Holzbaur, and Y.E. Goldman. 2008. Kinesin and dynein-dynactin at intersecting microtubules: motor density affects dynein function. *Biophysical journal*. 94:3115-3125.

Ross, J.L., K. Wallace, H. Shuman, Y.E. Goldman, and E.L. Holzbaur. 2006. Processive bidirectional motion of dynein-dynactin complexes in vitro. *Nature cell biology*. 8:562-570.

Rudiger, M., U. Plessman, K.D. Kloppel, J. Wehland, and K. Weber. 1992. Class II tubulin, the major brain beta tubulin isotype is polyglutamylated on glutamic acid residue 435. *FEBS letters*. 308:101-105.

Rutter, G.A., and E.V. Hill. 2006. Insulin vesicle release: walk, kiss, pause ... then run. *Physiology*. 21:189-196.

Sackett, D.L. 1995. Structure and function in the tubulin dimer and the role of the acidic carboxyl terminus. *Sub-cellular biochemistry*. 24:255-302.

Schaap, I.A., C. Carrasco, P.J. de Pablo, and C.F. Schmidt. 2011. Kinesin walks the line: single motors observed by atomic force microscopy. *Biophysical journal*. 100:2450-2456.

Schnapp, B.J., R.D. Vale, M.P. Sheetz, and T.S. Reese. 1985. Single microtubules from squid axoplasm support bidirectional movement of organelles. *Cell*. 40:455-462.

Schuster, M., S. Kilaru, G. Fink, J. Collemare, Y. Roger, and G. Steinberg. 2011. Kinesin-3 and dynein cooperate in long-range retrograde endosome motility along a nonuniform microtubule array. *Molecular biology of the cell*. 22:3645-3657.

Scott, D.A., U. Das, Y. Tang, and S. Roy. 2011. Mechanistic logic underlying the axonal transport of cytosolic proteins. *Neuron*. 70:441-454.

Settembre, C., A. Fraldi, D.L. Medina, and A. Ballabio. 2013. Signals from the lysosome: a control centre for cellular clearance and energy metabolism. *Nature reviews. Molecular cell biology*. 14:283-296.

Sharma, N., J. Bryant, D. Wloga, R. Donaldson, R.C. Davis, M. Jerka-Dziadosz, and J. Gaertig. 2007. Katanin regulates dynamics of microtubules and biogenesis of motile cilia. *The Journal of cell biology*. 178:1065-1079.

Shastry, S., and W.O. Hancock. 2010. Neck linker length determines the degree of processivity in kinesin-1 and kinesin-2 motors. *Current biology : CB*. 20:939-943.

Sivaramakrishnan, S., and J.A. Spudich. 2009. Coupled myosin VI motors facilitate unidirectional movement on an F-actin network. *The Journal of cell biology*. 187:53-60.

Song, Y.H., and E. Mandelkow. 1993. Recombinant kinesin motor domain binds to beta-tubulin and decorates microtubules with a B surface lattice. *Proceedings of the National Academy of Sciences of the United States of America*. 90:1671-1675.

Soppina, V., A.K. Rai, A.J. Ramaiya, P. Barak, and R. Mallik. 2009. Tug-of-war between dissimilar teams of microtubule motors regulates transport and fission of endosomes. *Proceedings of the National Academy of Sciences of the United States of America*. 106:19381-19386.

Subramanian, R., E.M. Wilson-Kubalek, C.P. Arthur, M.J. Bick, E.A. Campbell, S.A. Darst, R.A. Milligan, and T.M. Kapoor. 2010. Insights into antiparallel microtubule crosslinking by PRC1, a conserved nonmotor microtubule binding protein. *Cell*. 142:433-443.

Suryavanshi, S., B. Edde, L.A. Fox, S. Guerrero, R. Hard, T. Hennessey, A. Kabi, D. Malison, D. Pennock, W.S. Sale, D. Wloga, and J. Gaertig. 2010. Tubulin glutamylation regulates ciliary motility by altering inner dynein arm activity. *Current biology : CB*. 20:435-440.

Svoboda, K., and S.M. Block. 1994. Force and velocity measured for single kinesin molecules. *Cell*. 77:773-784.

Svoboda, K., C.F. Schmidt, B.J. Schnapp, and S.M. Block. 1993. Direct observation of kinesin stepping by optical trapping interferometry. *Nature*. 365:721-727.

Telley, I.A., P. Bieling, and T. Surrey. 2009. Obstacles on the microtubule reduce the processivity of Kinesin-1 in a minimal in vitro system and in cell extract. *Biophysical journal*. 96:3341-3353.

Tulin, A., S. McClerklin, Y. Huang, and R. Dixit. 2012. Single-molecule analysis of the microtubule cross-linking protein MAP65-1 reveals a molecular mechanism for contact-angle-dependent microtubule bundling. *Biophysical journal*. 102:802-809.

Tytell, M., M.M. Black, J.A. Garner, and R.J. Lasek. 1981. Axonal transport: each major rate component reflects the movement of distinct macromolecular complexes. *Science*. 214:179-181.

Uchimura, S., Y. Oguchi, M. Katsuki, T. Usui, H. Osada, J. Nikawa, S. Ishiwata, and E. Muto. 2006. Identification of a strong binding site for kinesin on the microtubule using mutant analysis of tubulin. *The EMBO journal*. 25:5932-5941.

Vale, R.D. 2003. The molecular motor toolbox for intracellular transport. *Cell*. 112:467-480.

Vale, R.D., and R.J. Fletterick. 1997. The design plan of kinesin motors. *Annual review of cell and developmental biology*. 13:745-777.

Vale, R.D., T. Funatsu, D.W. Pierce, L. Romberg, Y. Harada, and T. Yanagida. 1996. Direct observation of single kinesin molecules moving along microtubules. *Nature*. 380:451-453.

Vale, R.D., T.S. Reese, and M.P. Sheetz. 1985a. Identification of a novel force-generating protein, kinesin, involved in microtubule-based motility. *Cell*. 42:39-50.

Vale, R.D., B.J. Schnapp, T. Mitchison, E. Steuer, T.S. Reese, and M.P. Sheetz. 1985b. Different axoplasmic proteins generate movement in opposite directions along microtubules in vitro. *Cell*. 43:623-632.

Verhey, K.J., D.L. Lizotte, T. Abramson, L. Barenboim, B.J. Schnapp, and T.A. Rapoport. 1998. Light chain-dependent regulation of Kinesin's interaction with microtubules. *The Journal of cell biology*. 143:1053-1066.

Verhey, K.J., D. Meyer, R. Deehan, J. Blenis, B.J. Schnapp, T.A. Rapoport, and B. Margolis. 2001. Cargo of kinesin identified as JIP scaffolding proteins and associated signaling molecules. *The Journal of cell biology*. 152:959-970.

Vershinin, M., B.C. Carter, D.S. Razafsky, S.J. King, and S.P. Gross. 2007. Multiple-motor based transport and its regulation by Tau. *Proceedings of the National Academy of Sciences of the United States of America*. 104:87-92.

Wang, L., C.L. Ho, D. Sun, R.K. Liem, and A. Brown. 2000. Rapid movement of axonal neurofilaments interrupted by prolonged pauses. *Nature cell biology*. 2:137-141.

Weisbrich, A., S. Honnappa, R. Jaussi, O. Okhrimenko, D. Frey, I. Jelesarov, A. Akhmanova, and M.O. Steinmetz. 2007. Structure-function relationship of CAP-Gly domains. *Nature structural & molecular biology*. 14:959-967.

Welte, M.A. 2004. Bidirectional transport along microtubules. *Current biology : CB*. 14:R525-537.

Woehlke, G., A.K. Ruby, C.L. Hart, B. Ly, N. Hom-Booher, and R.D. Vale. 1997. Microtubule interaction site of the kinesin motor. *Cell*. 90:207-216.

Yang, J.T., R.A. Laymon, and L.S. Goldstein. 1989. A three-domain structure of kinesin heavy chain revealed by DNA sequence and microtubule binding analyses. *Cell*. 56:879-889.

Yildiz, A., M. Tomishige, A. Gennerich, and R.D. Vale. 2008. Intramolecular strain coordinates kinesin stepping behavior along microtubules. *Cell*. 134:1030-1041.

Yildiz, A., M. Tomishige, R.D. Vale, and P.R. Selvin. 2004. Kinesin walks hand-over-hand. *Science*. 303:676-678.

Zhu, H., H.Y. Lee, Y. Tong, B.S. Hong, K.P. Kim, Y. Shen, K.J. Lim, F. Mackenzie, W. Tempel, and H.W. Park. 2012. Crystal structures of the tetratricopeptide repeat domains of kinesin light chains: insight into cargo recognition mechanisms. *PloS one*. 7:e33943.